ELECTROSTATIC CONTROL OF MICROFLUIDIC SYSTEMS FOR ENHANCEMENT OF NANOPARTICLE SEPARATIONS AND FET NANOBIOSENSORS

BY

VIKHRAM VILASUR SWAMINATHAN

DISSERTATION

Submitted in partial fulfillment of the requirements
for the degree of Doctor of Philosophy in Mechanical Engineering
in the Graduate College of the
University of Illinois at Urbana-Champaign, 2015

Urbana, Illinois

Doctoral Committee:

Professor M. Taher A. Saif, Chair
Professor Rashid Bashir, Director of Research
Professor Placid M. Ferreira
Associate Professor Sascha Hilgenfeldt
Dr. Andrew Fischer, Abbott Laboratories

Abstract

An abundance of ions in saline media or physiological buffers causes extensive shielding of charged surfaces and potentials. As a result, electrostatic forces cannot penetrate beyond the electrochemical double layer (EDL); conversely, charged molecules outside the EDL cannot transduce a sensor surface and are rendered effectively invisible. In this thesis, we discuss a separation problem and a sensing problem that are both constrained by this fundamental limitation. Our goal has been to explore novel electrical pathways for circumventing the loss of electrostatic effects: towards improving the dielectrophoretic separation of sub-micron colloids, or the mitigation of EDL shielding for improved label-free electrical detection of analyte molecules using field-effect biosensors.

Dielectrophoresis is a favored method for numerous microfluidic applications for the capture of biological species, as well as, separation of organic and inorganic contaminants from water. However, given that ionic mobility (by far) exceeds those of the suspended matter, the ions redistribute rapidly to overwhelm any electrophoretic effects within the system. Any attempt at capturing sub-micron particles by electrostatic means is drastically limited due to the dual effect of weak electric fields in the media, as well as poor volumetric scaling of separation forces with respect to particle size. In order to improve the capture of colloids, we have designed a scheme based on multiple interdigitated electrode (IDE) arrays under mixed AC/DC bias. Through AC electroosmotic micromixing that breaks the EDL shielding, as well as a transverse DC component, the separation field penetrates across a microchannel to capture particles from the bulk. We analytically determine favorable biasing conditions for field enhancement through circuit analysis and demonstrate the enhanced electric field through computational simulations. Under these conditions, we experimentally demonstrate improved capture of 0.75 μm diameter colloids over conventional AC-DEP methods. Depending on the salinity of the suspension, the method can be used to design species collection zones in microfluidic systems.

Biosensors based on the field-effect transistor (FET) are capable of detecting molecular binding or hy-

bridization events through direct coupling of analyte charge with conduction through the FET. This label-free approach can be used to realize ultraportable and point-of-care (POC) diagnostic devices. However, the charge of biomolecules is inevitably screened by surrounding ions, thus reducing the overall sensitivity in any practical solution. To address this fundamental problem, we have examined the possibility of modifying the salt background around a sensor. With the help of on-chip polarizable electrodes, we demonstrate a method for localized electronic desalting of a FET biosensor. By locally removing the excess ions that shield the device from analytes, the Debye length around the senor can be sufficiently increased to encompass the molecular layers. Hence, the apparent charge of the target molecules can be maximized and the sensitivity of the device increased.

We have visited the 100-year-old Gouy-Chapman theory that is the most widely used to model EDLs, and incorporated theoretical advancements from Modified Poisson-Boltzmann models, to accurately predict the regimes in which desalting of highly saline solutions can be effective. Furthermore, we have designed a biasing scheme in which the on-chip microelectrodes can gate bias the FETs during the desalting process itself, thereby circumventing the back diffusion of ions to allow simultaneous sensing experiments. In order to overcome the adverse scaling of surface capacitance against ionic concentration, and desalting limitations arising out of non-zero ion-sizes and ion crowding in EDLs, it is necessary to reduce the scale of the biosensor to that of a microdroplet as well as incorporate surface-area enhancements on the desalting electrodes. Although challenging to implement such a construct, sub-nanoliter droplets around FET(s) can serve as isolated chambers for parallel reactions. We have achieved favorable desalting capacity in the $\sim$10mM salinity regime, without loss of molecular stability for which salt is known to play a crucial role. Additionally, we have also leveraged the scalability of semiconductor electronics to incorporate large scale arrays of FETs to overcome device-to-device variations and also enable parallel detection experiments. Finally, we have adapted and characterized well-known functionalization chemistries for optimal capture of analyte monolayers on the devices. We believe that our study uniquely addresses the fundamental phenomenological limitation associated with excess salt as a key determinant of sensitivity. Our approach can pave the way for multiplexed label-free electronic detection in physiological solutions with improved sensitivity.

In memory of Professor Mark A. Shannon.

And, to the indefatigable spirit of my parents and Yamini. C'est la vie!

Acknowledgments

From the outset, I am extremely grateful to Prof. Rashid Bashir for advising me in bringing my doctoral research to a complete and cohesive story. He took me in at a time when I needed guidance after the loss of my then doctoral advisor, Prof. Mark A. Shannon. I met Prof. Bashir first during a guest lecture he delivered for the ME598 (Advanced MEMS/NEMS) class for which I was the TA. At the time, I sought his mentoring for my project on dielectrophoresis and he readily agreed, saying, "OK, lets talk." Since then, Prof. Bashir absorbed me into his group seamlessly and offered unconditional support, along with the periodic push/nudge to ensure that I maintained my focus on key goals. Without these, my PhD would have just not been possible! The bio-nano-FET project has added a dimension on microsensors to my research profile that I had always hoped for.

I would also like to express my gratitude to Prof. Taher Saif, Prof. Placid Ferreira, Prof. Sascha Hilgenfeldt and Dr. Andrew Fischer (Abbott Laboratories) for agreeing to serve on my PhD committee. Every member of my committee has, notwithstanding their busy schedules, taken keen interest in my projects and provided valuable feedback and extremely constructive suggestions right up to my defense exam from which I stand to benefit much in my future pursuit. Prof. Ferreira has been instrumental in ensuring that all Shannon group students are continually supported by the MechSE department towards graduating from our programs. I met Prof. Taher Saif first at the IEEE MEMS Conference in Italy. From an excursion to the ruins of Pompeii, to his exceptional course on the Mechanics of MEMS, to serving as my committee Chair and, many research discussions, I have enjoyed a very nice friendship and wise counsel from Prof. Saif. I owe many thanks to all of my committee members for the role they have played in my PhD.

Prof. Mark A. Shannon offered me my first big opportunity to work on MEMS, a topic very close to my heart. I recall that joining Mark's group wasn't easy, for it took not one but two attempts to get his attention. I recall him agreeing to be my advisor and supervise my research with his classic one-liner: "You must be bold enough to make mistakes". I think I took him literally. So, in many ways, my research has taken its time and encountered a few challenges in the process of maturing. I consider the opportunity to co-author with him a review article on transport through nanocapillary membranes as a crucial learning

experience, which I have continued to use towards my ongoing research. Mark Shannon, above all, has taught me to be equally compassionate and appreciative of colleagues and competitors, and continues be an inspiration.

During the course of this work, I have learned several things from Mark, and rediscovered that again from Prof. Bashir—on the art of conducting research, communication, advising and teaching and, most importantly, ethics. I had noted Mark's emphasis for research communication at the time of presenting my MS research, I would be remiss if I do not recount how both my advisors have placed the utmost importance on the quality of research presentation.

My research has depended on many resources. I would also like to acknowledge the Defense Advanced Research Project Agency, the National Science Foundation, the National Institutes of Health, Abbott Laboratories, TSMC, the WaterCAMPWS and NanoCEMMS Centers, MNTL, MRL and the MechSE Departments for financial and facilities support in my projects. Our collaborators from Purdue University, Piyush Dak and Prof. Ashraf Alam have supported us with key analytical and computational aspects of my research problem.

Dr. Glennys Mensing, has provided much support and coordinated my research, besides guiding me through my TA positions. Glennys has played a stellar role in looking out for Shannon group members and ensuring that all of us are on track to our degrees. I have directly benefited from her help (as well as that of Mike Hansen and Miki Takagi's) in the MNTL and MNMS cleanrooms. At other times, especially when things were tough, Glennys has given advice and much encouragement to boost my morale.

Dr. Bruce Flachsbart gave me my first real lessons in MEMS and some of the best about cleanroom research. I especially enjoyed working with him, his teaching style and putting together the course on Advanced MEMS/NEMS.

Members of Prof. Bashir's research group, LIBNA, have been extremely welcoming and supportive. Dr. Bobby Reddy Jr., Dr. Brian Dorvel, Dr. Eric Salm, and Carlos Duarte have helped me so much with understanding FETs and biosensors and patiently enabled me to transition onto the bio-nano-FET project. The likes of Anurup, Caroline, Elise, Gelson, Greg, Jiwook, Laolu, Ritu, Sangjo, Shouvik, Tanmay, and Umer, with whom I have enjoyed many research discussions and who have given me valuable feedback during meetings. Shahzad, Yunice, Anu and Mariam were junior and undergraduate students involved with our project. Especially, Shahzad and Yunice have helped me with experiments and microfabrication.

In addition to my thesis research, I also had the opportunity to collaborate with several peers. Dr. Likun Zhu (IUPUI) was my close mentor early in my graduate program. I am extremely indebted to him for guiding me through my infancy in MEMS and, later, collaborating with me on a nanofabrication project. Dr. Huan Hu

was also part of this collaboration, and it has been a pleasure to work with him while I have benefited from several useful discussions too. Dr. Byunghoon Bae (NASA/JPL) and Dr. Junghoon Yeom (Michigan State Uni.) have always offered help and many useful tips and suggestions. And all members of the Shannon group- Ali, Andrea, Cody, Damena, Kisung, Mbikayi, Shama, Ton and Yaofeng who made life in the MEB basement good.

During my graduate program, I also had several teaching opportunities. I am extremely grateful to the MechSE department for providing TA support in times of need. I have learnt a lot about teaching and course development during many useful discussions that I had with Prof. Pratap Vanka, Dr. Glennys Mensing, Dr. Richard Keane, Prof. Dmitrios Kyritsis, Prof. Randy Ewoldt, Prof. Sungwoo Nam, Prof. Blake Johnson and Prof. Sewoong Oh and Prof. Mike Philpott. The Mavis Fellowship and the Center for Innovation in Teaching and Learning have enabled me develop a strong teaching philosophy, discover my love for teaching, and also improve my faculties through the Graduate Teacher Certificate Program.

I am also very grateful to Kathy Smith, Jennifer Hayden, Emily Lange and Laurie Macadam, who have helped me on so many occasions on behalf of the MechSE department, especially with my added travel and visa issues.

Academics aside, I found some of the most wonderful friends at Champaign-Urbana. I enjoyed volunteering for Asha for Education as well, along with the likes of Aravind, Vidisha, Harini, Gowri, Pradeep, Praveen, Vinay, Milu, Kaushik, Vivek, Urmitapa, Raghu, Avanija, Navaneethan, Swetha, Vinod, Chandu, Preeti and Padmaja. I have shared some great times over tea, games, picnics, camping and fairly heated debates with them.. and also discovered the joy of running!

Last, but not the least—family. My parents, Uma and Swaminathan and little brother, Rohith have been the greatest source of strength and support throughout my pursuits. I have always found their advice and philosophy to fall back on whenever I needed help to maintain focus. And my wife, Yamini, who has cheerfully been my emotional and moral support throughout while patiently waiting for 9 years! Not once has she doubted my intent and has never been short of encouragement when I needed it the most.

Although this thesis has taken time shaping up, I dedicate it to Mark Shannon for his inspiration, and my parents and Yamini, for their unwavering support and fighting spirit.

Table of Contents

List of Tables

List of Figures

List of Abbreviations

AC	Alternating Current.
ACED	Alternating Current Electrodialysis.
ACEO	Alternating Current Electroosmosis.
AFM	Atomic Force Microscopy.
AMP	Antibody Mimic Protein.
APDMES	(3-aminopropyl)-dimethyl-ethoxysilane.
BHF	Buffered Hydrofluoric Acid.
CA	Contact Angle.
CDL	Composite Double Layer.
C.E.	Counter Electrode.
CMOS	Complementary Metal-Oxide-Semiconductor.
CNT	Carbon Nanotubes.
CV	Cyclic Voltammetry.
DC	Direct Current.
DEP	Dielectrophoresis.
DI water	Deionized Water.
DNA	Deoxyribonucleic Acid.
DRIE	Deep Reactive Ion Etching.
dsDNA	Double-stranded DNA.
EDL	Electrochemical Double Layer.
EG-FET	Extended Gate Field-effect Transistor.
EIS	Electrochemical Impedance Spectroscopy.
FET	Field-effect Transistor.
GC	Gouy-Chapman.
GPDMES	(3-glycidoxypropyl)-dimethyl-ethoxysilane.

HSA	High Surface Area.
ICP-DRIE	Inductively Coupled Plasma-Deep Reactive Ion Etching.
IDE	Interdigitated Electrode.
IHP	Inner Helmholtz Plane.
IPA	Isopropyl alcohol/propan-2-ol.
ISFET	Ion-sensitive Field-effect Transistor.
LAMP	Loop Mediated Isothermal Amplification.
LOD	Limit Of Detection.
LPCVD	Low Pressure Chemical Vapor Deposition.
MACEtch	Metal Assisted Chemical Etching.
MEMS	Micro-Electro-Mechanical Systems.
miRNA	micro-RNA.
MOSFET	Metal-Oxide-Semiconductor Field-effect Transistor.
MPB	Modified Poisson-Boltzmann.
NMOS	N-type Metal-oxide-semiconductor.
OCV	Open-circuit Voltage.
OHP	Outer Helmholtz Plane.
PBS	Phosphate Buffered Saline.
PCR	Polymerase Chain Reaction.
PDMS	Polydimethylsiloxane.
PECVD	Plasma Enhanced Chemical Vapor Deposition.
PI	Polyimide.
POC	Point-of-care.
PMOS	P-type Metal-oxide-semiconductor.
PPy	Polypyrrole.
PSA	Prostate Specific Antigen.
PTFE	Polytetrafluoroethylene.
QRE	Quasi Reference Electrode.
REFET	Reference Field-effect Transistor.
RIE	Reactive Ion Etching.
RMS	Root Mean Squared.
RNA	Ribonucleic Acid.
RO	Reverse Osmosis.

SAM	Self-assembled Monolayer.
SEM	Scanning Electron Microscopy.
SiNP	Silicon Nanopillar.
SSC	Saline Sodium Citrate.
ssDNA	Single-stranded DNA.
W.E.	Working Electrode.

List of Symbols

λ_D	Debye length.
ε	Permittivity.
ε_0	Dielectric constant.
k_B	Boltzmann's constant.
T	Temperature.
N_A	Avogadro number.
e	Fundamental charge.
n_0	Bulk ionic concentration.
ΔP	Pressure drop.
Π	Osmotic pressure drop.
m	Mass.
$\vec{A}$	Acceleration.
$\vec{F}_E$	Separation force.
$\vec{F}_{drag}$	Drag force.
$\vec{E}$	Electric field intensity.
q	Charge.
$\vec{Q}$	Quadrupole.
t	Time.
r	Particle radius.
ε_m	Dielectric constant of medium.
ω	AC frequency.
$K(\omega)$	Clausius-Mossotti factor.
φ	Spatial phase component of electric field.
ε^*	Complex permittivity.
σ	Conductivity.

$\vec{F}_{DEP}$	Dielectrophoretic force.
V_{PP}	Applied AC bias magnitude.
V_{Debye}	Voltage drop in EDL.
z	Distance from electrode (chapter 3).
Ω	Dimensionless parameter.
η	Dynamic viscosity.
$\vec{D}$	Displacement electric field.
G_0	Conductance.
ΔG	Change in conductance.
d	Nanowire diameter.
μ	Mobility.
L_{NW}	Nanowire length.
N_D	Number density of charge carriers.
Γ_l	Salt-dependent sensitivity.
R	Nanowire radius (chapter 4).
l	Length of analyte from nanowire surface.
$\Delta V_{Desalting}$	Desalting bias.
n_0	Initial ionic concentration.
n_i	Final ionic concentration.
ψ	Local potential.
ψ_0	Potential drop across EDL.
z	Ion charge number (chapter 5).
σ_e	Surface charge density in EDL.
ν	Ion packing fraction.
a	Ion size.
$n(\vec{r})$	Local anion concentration.
$p(\vec{r})$	Local cation concentration.
V_Ω	Volume of droplet domain.
l_c	Compact layer thickness.
A_e	Electrode surface area.
λ_i	Apparent Debye length.
f	Desalting fraction (chapter 5).
V_c	Critical voltage.

V_e	Desalting bias.
V_b	Voltage across diffuse Boltzmann layer.
$V_{\Omega,max}$	Maximum volume desalted.
Q_e	Surface charge adsorbed.
V/SA	Droplet volume to electrode surface area ratio.
$V_{Desalting1}, V_{Desalting2}$	Desalting voltages.
V_g	Gate bias.
τ	Timescale of ion diffusion.
L	Characteristic length.
D	Diffusivity.
I_D, I_{DS}	Transistor source-drain current.
Z	Impedance.
f	frequency (chapter 6).
R	Resistance (chapter 6).
C	Capacitance.
I_g	Gate leakage current.
θ^*	Apparent contact angle.
f	Area fraction (chapter 8).
θ_y	Young's contact angle.
M_1, M_2	Micro re-entrant structures.
H_1, H_2	Micro re-entrant+hierarchical structures.
H_3	Micropillar+hierarchical structure.

Chapter 1

Introduction

1.1 Shielding at electro-electrolyte interfaces

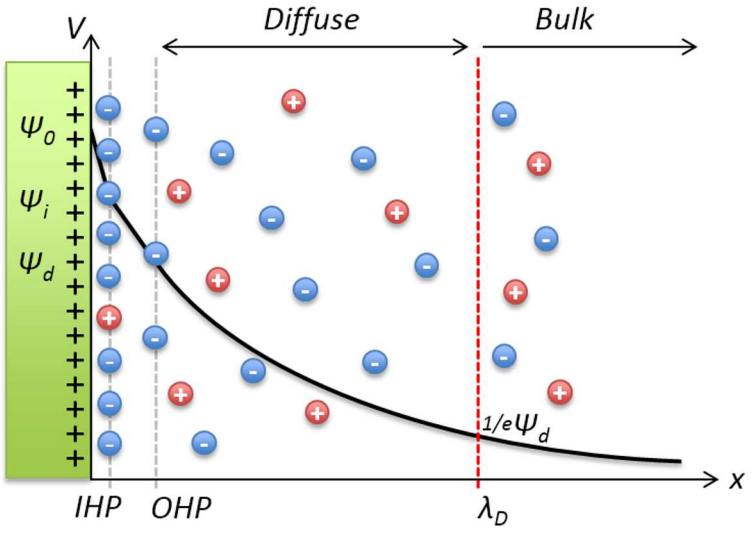

Figure 1.1: A schematic of the electrochemical double layer at an electrode-electrolyte interface.

A charged surface in solution, or an equivalent voltage applied at an electrode, attracts counter-ions from the electrolyte. This causes a redistribution of charges at the electrode-electrolyte interface through the formation of the electrochemical double layer (EDL) [1]. It is a well-known effect that the background excess of ions in electrolytes interferes with electrochemical phenomena due to heavy shielding of electrode-electrolyte interfaces as well as charged molecules by the EDL. Figure 1.1 shows a schematic of the EDL composition at an electrode-electrolyte interface. When a surface potential, ψ_0, is applied, a compact monolayer of counter-ions (also known as the Stern layer) condenses at the surface within the inner Helmholtz plane (IHP). Outside the compact layer, beyond the outer Helmholtz plane (OHP), a diffuse region is formed comprising a concentrated mixture of enriched counter-ions and depleted co-ions. The electric field in the

diffuse EDL region of fairly dilute solutions decays exponentially and the ionic concentration also decreases as we move away from the electrode to merge with the bulk. The overall salt concentration in the EDL is much greater than the bulk concentration, with an increased number of counter-ions and decreased number of co-ions. The phenomenological lengthscale associated with the EDL, over which electric field decays exponentially to $1/e$ of its intensity at the surface, is also known as the Debye length, λ_D given by [2, 3]

$$\lambda_D = \sqrt{\frac{\varepsilon_0 \varepsilon_r k_B T}{2 N_A e^2 n_0}} \tag{1.1}$$

for a 1:1 electrolyte, where ε_0 is the electric permittivity of free space, ε_r the dielectric constant of the electrolyte, k_B is the Boltzmann constant, T the temperature, N_A the Avogadro number, e the fundamental electronic charge and n_0 the ionic concentration of the electrolyte. Physiological fluids, such as blood, plasma and serum, have high salt content of up to 150mM, isotonic with biological buffers such as phosphate buffered saline (PBS) and saline sodium citrate (SSC). Sourcewater obtained from freshwater and ocean sources for human consumption has a wide salinity range of 1-550mM. At these high concentrations, λ_D<1 nm; thus, *a*) electrostatic separation fields cannot penetrate the EDL to perturb the bulk solution in microfluidic systems, and, *b*) surface charges present on target analytes (which are typically ∼10 nm in size or larger) will likely be completely shielded from the surface of a biosensor as they reside outside the Debye length.

Therefore, the EDL establishes fundamental limitations in electrolytes. Electrostatic separation fields can only be sustained if enough work is performed to overcome the electrostatic shielding, a challenging problem considering that the number of ions in solution that contribute to this effect outnumber the species being separated by several orders of magnitude! Similarly, in order to enable direct, label-free transduction of a field-effect biosensor, it is crucial that we artificially extend the Debye length through desalting or modify the relative proximity of bound analytes so that their surface charges are included. Separation and sensing schemes will benefit from techniques that can overcome EDL shielding or workarounds to sustain electric fields in solution.

1.2 Summary of studies undertaken

In this research, we have mainly addressed a separation problem and a sensing problem. The separation problem deals with the capture of sub-micron colloidal particles from aqueous media by enhancing the dielectrophoresis forces using a new multielectrode architecture and mixed AC/DC biasing scheme. The sensing problem is based on the label free detection of micro-RNA markers using field-effect biosensors. We have implemented a method of localized electronic desalting to overcome screening limitations at high

salt conditions and outline a scheme of integrating this with a transistor-in-droplet platform. Further, we have examined the multiplexing capability and statistical improvements of detection experiments with arrays of transistors. In addition, we also report the results of a nanofabrication study to develop re-entrant and hierarchical micro/nanostructures in silicon substrates for superhydrophobicity with extremely low hysteresis.

1.3 Thesis outline

This thesis has been divided into in three parts. The first part (chapters 2 & 3) deals with the separation problem. Chapter 2 motivates the need for colloidal separation and reviews the literature on dielectrophoresis, the most widely used method for microfluidic particle separations. This chapter also identifies the scaling issues and outlines a modified approach for improved dielectrophoresis with the use of multiple interdigitated electrode arrays and a mixed biasing scheme. Chapter 3 contains a theoretical analysis of AC electroosmotic flow to identify regimes of field enhancement, finite element simulation of an improved separation scheme, and its experimental demonstration with sub-micron colloids where we clearly show improved separation over conventional dielectrophoresis.

The second part of the thesis (chapters 4-7) deals with the problem of label-free sensing with field-effect nanobiosensors. Chapter 4 introduces the sensing problem with an overview of label-free molecular detection using field-effect devices. This is followed by an analysis of how screening effects impede these devices, and the extent of desalting needed to overcome this problem. At the same time, the role of salt ions on biomolecular stability is also examined to establish certain feasibility requirements to achieve improvements with desalting. Chapter 5 introduces the concept of localized electrostatic desalting and contains a detailed discussion of nanofluidic theories to accurately predict the desalting capacity before outlining certain practical requirements for on-chip electrodes. Chapter 6 contains the experimental realization and characterization of desalting, along with a novel pathway for biasing the FET in microroplet platforms. A CMOS-compatible method to fabricate electrodes, increase their surface and enhance their performance through electrochemical treatments is outlined and their eventual desalting capacity is quantified. Chapter 7 deals with the sensing experiments for detection of miRNAs. A large array of transistors is introduced to facilitate statistical improvements and multiplexing. Molecular functionalization protocols are revisited to analyze the capture and orientation of molecules on the array geometry and the role of probe concentrations studied.

The third and final part of this thesis (chapter 8) is a discussion of a nanofabrication problem. A method of combining hierarchical nanofeatures over re-entrant microstructures is presented, in order achieve

superhydrophobic structures with extremely low contact angle hysteresis. A one-mask, highly scalable approach towards fabricating 3-D out-of-plane nanostructures in silicon is discussed.

Chapter 9, in conclusion, highlights the significant developments and outcomes of this study and projects the future work needed to expand the capability of label-free detection using the field-effect nanobiosensor.

Chapter 2

Dielectrophoretic separation of particles

2.1 Motivation behind the separation problem

The first part of this thesis is based on a sub-micron particle separation problem. The study was conceived as part of the MANTRA project in the Shannon group, whose goal was the development of an improved desalination system comprising various stages that separated out contaminants based on size and physical properties. Figure 2.1 shows a schematic layout of the MANTRA desalination system. The current study on separation of colloidal foulants was envisaged as the final particulate separation module, called ACED colloidal particle separator, before reverse osmosis (RO) desalination. The overall objective was to remove suspended colloidal scale particles before the RO stage in order to achieve net energy efficiency over conventional RO that requires frequent backwashing of membrane foulants. In this chapter, we discuss and formulate the colloid separation problem and touch upon key aspects of AC electrostatics approaches[1].

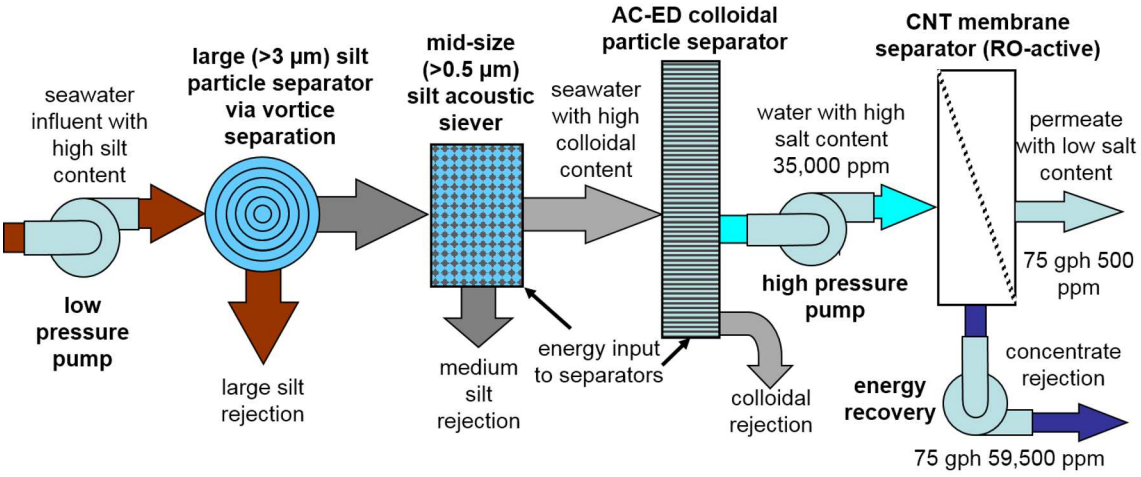

Figure 2.1: Schematic of the MANTRA desalination system

[1]Some results discussed in this chapter are published in [4]. Reproduced with permission from Springer Science+Business Media.

2.1.1 Opportunities for improved separation of suspended matter

The energy consumption during desalination and water purification processes can be analyzed through the equivalent pressure drop at various stages of the plant. Equation 2.1 captures the stage-wise pressure drop in an RO system due to native (1) as well as local salinity (2), amount of rejectate (3), membrane fouling (4), concentration polarization (5), membrane flux (6) and module configuration (7). Desalination systems are designed to operate in the range of 42 atm (625 psi) to a high of 71 atm (1050 psi), and at 55 atm (800 psi) in typical cases. Of all the pressure drops described, ΔP_{Foul}, is often the most significant and also has indirect implications for terms (5) and (6). Hence, key to optimizing the cost and energy-density of the desalinator is to minimize the losses associated with fouling.

$$\Delta P = \overset{(1)}{\Pi_{Osmotic|\infty}} + \overset{(2)}{\Pi_{Osmotic|X}} + \overset{(3)}{\Delta P_{Reject}} + \overset{(4)}{\Delta P_{Foul}} + \overset{(5)}{\Delta P_{Polar}} + \overset{(6)}{\Delta P_{Membrane}} + \overset{(7)}{\Delta P_{Module}} \tag{2.1}$$

2.1.2 The occurrence and role of colloids

Irreversible fouling is caused primarily by small molecules (O(100's kDa) and $<1\ \mu m$ in size) such as inorganic silica colloids, proteins, lipids, humic substances and other natural organic matter. Various studies have characterized the size and occurence of colloids, including geographical, seasonal and depth variations in the water sources [5, 6, 7]. While 99% of all suspended matter is contained in silt and microparticles ($\geq 1\ \mu m$) that can be sedimented, the 1% composed of colloids is most numerous with a typical ocurrence of 100 ppm (approximately 1 billion particles per mL) [7]. Most of these colloidal species are sufficiently small and light enough to be unaffected by gravimetric separation methods. At the same time they are also charged [8, 9], with a relatively high charge to mass ratio compared to micron and larger sized particles, due to which they have a tendency of adhering strongly to the surfaces and pores of membranes [10].

The schematic in figure 2.2(b) shows a mechanism of membrane fouling. Sub-micron particles can block the surfaces of pores and also get lodged in the walls permanently, thereby causing steep decrease in flux over time (figure 2.2(a)). The pressure drop due to fouling can be one order of magnitude in minutes, warranting frequent cleaning through a backwash process. This decreases the throughput and increases the energy cost per product water. Moreover, the irreversible nature of fouling does not permit full flux recovery, consequently degrading the filtration and RO membrane lifetimes as well. Therefore, desalination and purification systems would benefit from a technique that can eliminate colloids prior to the membrane-based steps in the system. Considering the charge and polarizability of suspended matter, an alternating current electrodialysis (ACED) scheme was motivated based on separation methods such as dielectrophoresis.

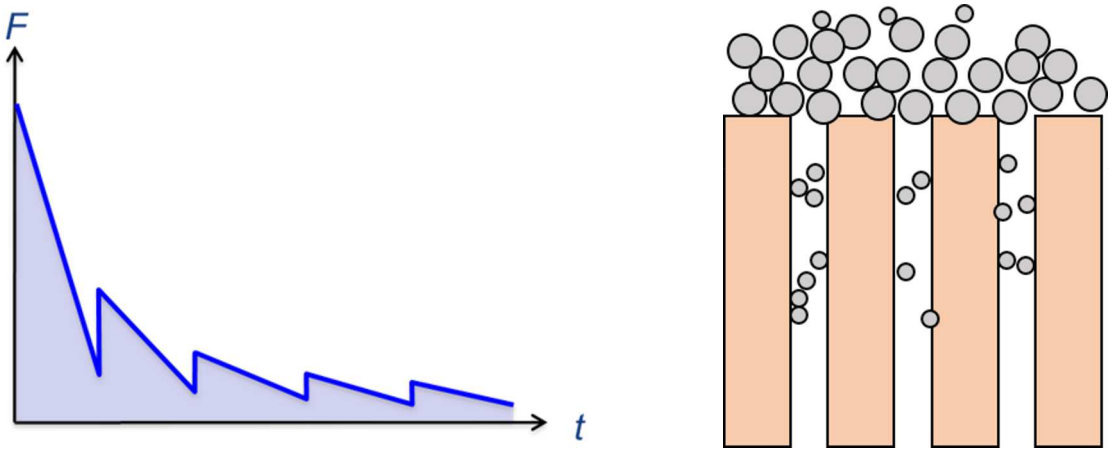

(a) Typical flux performance degration due to fouling of a superflux reverse osmosis membrane

(b) Colloids cause fouling of membranes by pore-blocking

Figure 2.2: Fouling issues in membrane-based filtration and desalination systems.

2.2 Dielectrophoresis

Dielectrophoresis (DEP) works on the basis of separation of polarizable neutral particles under a spatially non-uniform electric field [11]. Over the years, DEP has gained considerable interest [12] and is demonstrated widely for microfluidic capture, segregation and even patterning of particles and biological species such as rare cells, bacteria, viruses and other biomolecules. The generic equation for the separation force, $\vec{F}_E$, acting on a particle under the influence of an electric field is given by [13]

$$m\vec{A} = \vec{F}_E - \vec{F}_{drag} \tag{2.2a}$$

$$\vec{F}_E = q\vec{E} + (\vec{m}\nabla)\,\vec{E} + \frac{1}{6}\left(\vec{Q} : \vec{E}\right) + .. \tag{2.2b}$$

The first term describes electrophoretic effects arising from coulombic interaction between the net charge of the particle, q and the electrical field, $\vec{E}$. This vanishes in the absence of a net charge on the particle (typically the case due to shielding of surfaces) or in an alternating field whose time average is zero. Therefore the separation force is primarily contributed to by dielectric polarization, with the time-averaged DEP forces acting on a particle given by [11, 13, 14]:

$$\left\langle \vec{F}_E\,(t) \right\rangle = 2\pi\varepsilon_m r^3 \left\{ Re\left(K\left(\omega\right)\right)\nabla E^2_{RMS} + Im\left(K\left(\omega\right)\right)\left(E^2_x\nabla\varphi_x + E^2_y\nabla\varphi_y + E^2_z\nabla\varphi_z\right)\right\} \tag{2.3}$$

where, ε_m is the permittivity of the medium, r is the particle radius, $\vec{E}(\omega)$ is the electric field, φ_i $(i = x, y, z)$ are its spatial phase components, ω is the angular frequency, and $K(\omega)$ is the Clausius-Mossotti factor. The two components described on the right-hand side of equation 2.3 describe the DEP (real) and travelling wave (imaginary) or twDEP effects on the particles respectively. While DEP depends on the gradient of the electric field and can be modulated by geometric manipulation of the field lines, twDEP accounts for contributions from the spatial phase components and prominently features in periodic multielectrode systems with 4 or more phases. Derived from the complex permittivities ε_p^* and ε_m^* of the particle and medium, respectively, $K(\omega)$ determines the nature of DEP forces:

$$K(\omega) = \frac{\varepsilon_p^* - \varepsilon_m^*}{\varepsilon_p^* + 2\varepsilon_m^*} \tag{2.4}$$

where, $\varepsilon^* = \varepsilon + \dfrac{\sigma}{j\omega}$ is a function of the electric permittivity ε and conductivity σ of the material, and $j = \sqrt{-1}$. $K(\omega)$ behaves as a scaling coefficient in the calculation of $\left\langle \vec{F}_{DEP} \right\rangle$ and is bounded as follows: $-0.5 \leq Re\left(K(\omega)\right) \leq 1$ for DEP and $-1 \leq Im\left(K(\omega)\right) \leq 0$ for twDEP, in the case of homogeneous spherical particles. Figure 2.3 shows plots of the real and imaginary components of $K(\omega)$ for polystyrene beads (ε_r = 2.6) in aqueous solutions (ε_r = 80) across the frequency spectrum for various background ionic strengths. Note in figure 2.3(a) that while there exists a sharp crossover point between positive (pDEP) and negative (nDEP) forces in low salt media, $K(\omega) < 0$ through the frequency spectrum in more saline solutions and hence the beads will always experience nDEP. Further, with $-1 \leq Im\left(K(\omega)\right) \leq 0$ as seen in figure 2.3(b), the twDEP force can oppose the DEP force in low salt media if the device is AC-biased at below the crossover frequency for the particles.

2.2.1 Demonstrations of DEP separations

Among some recent demonstrations of DEP, Park et al. [15] developed a reusable printed circuit board-based electrode array for DEP manipulation of beads and cells. Cemazar et al. [16] demonstrated a reusable DEP fractionation chamber to separate mammalian cells based on their viability. Similarly, Zhu et al. [17] demonstrated a DEP system with castellated electrodes to separate bacterial cells based on viability. Bajaj et al. [18] segregated stem cells and polystyrene beads based on differences in polarizability, followed by stereolithographic patterning in hydrogels. Cen et al. [19] incorporated the combined effects of DEP, twDEP as well as electrorotation for the separation of malignant cells. Huang et al. [20], designed a hybrid DEP/immunocapture system using a Hele-Shaw flow cell to facilitate guided capture and enrichment of circulating tumor cells. Park et al. [21] demonstrated the use of nanofabricated probes to capture vaccinia

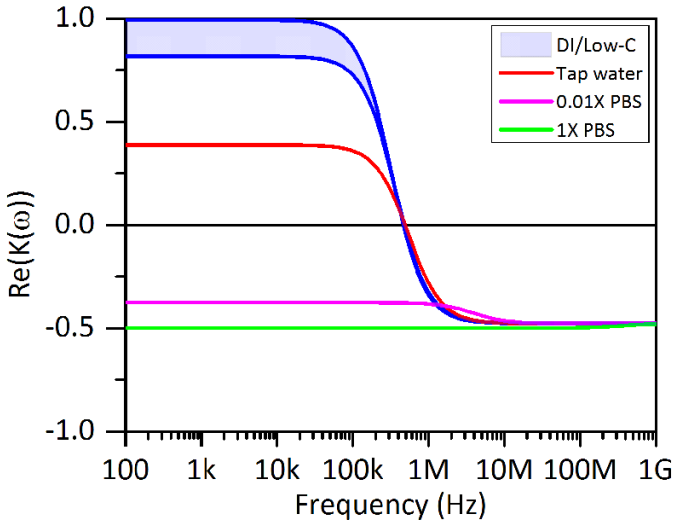

(a) Real (DEP) component of $K(\omega)$

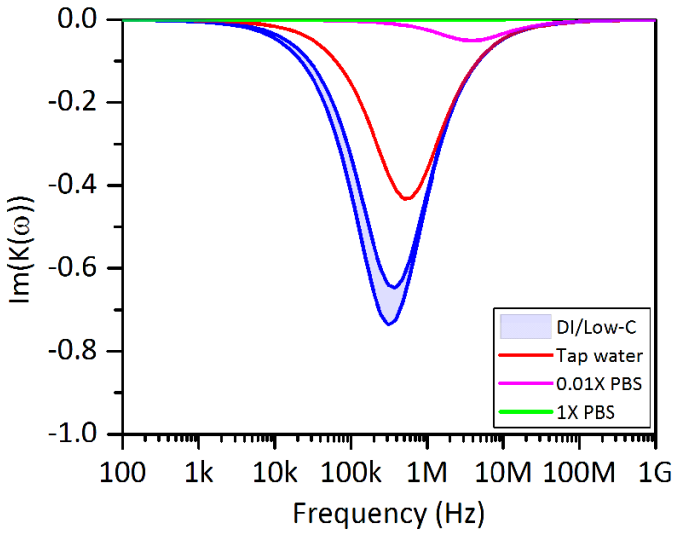

(b) Imaginary (twDEP) component of $K(\omega)$

Figure 2.3: The Clausius-Mossotti factor for a spherical polystyrene particle in various media.[2]

virus particles and characterize their dielectric properties. Interdigitated electrode arrays have also been used to implement combined DEP capture and impedance sensing of microparticles and bacteria [22, 23].

[2]Reproduced from [4], with permission from Springer Science+Business Media

2.2.2 Efforts to overcome scaling aspects of dielectrophoresis

DEP efficiency scales poorly due to the volumetric dependence on the particle size and, further, it is also inversely dependent on the spatial dimensions of the system [24, 25]. Various approaches have been adopted for enhancing the DEP effects such as with the use interdigitated electrode arrays and traveling wave schemes [26, 27, 28, 29, 30] and multiple frequency DEP [31]. Gadish and Voldman incorporated a herringbone chaotic advection mixer in order to increase the probablistic capture of spores over planar interdigitated electrodes [32]. Pethig [12] has also discussed the integration of novel electrode shapes and topologies. These include crossed electrode arrays [33], piecewise-curved electrodes [34] and castellated electrodes [35, 17] that have been implemented for spatial enhancement of DEP forces.

While most demonstrations of DEP and spatial enhancements have been very successful at the 1-10 μm particle sizes, sub-micron separations are particularly difficult. Castellanos et al. [36] have shown through scaling calculations for a 25 μm characteristic length that DEP forces at 5-15 V applied AC biases are weak compared to thermal fluctuations when we transition to the sub-micron sizes. The electrostatic fields and gradients can be enhanced locally by reducing the charcateristic lengthscale, i.e., the width and spacing of electrodes. However, the electric field typically decays rapidly towards the bulk away from the electrodes, and hence the DEP effects are weaker in these regions. Separation schemes for colloidal-scale particles require ways to sustain stronger forces in bulk.

2.3 Enhancement of DEP separations for colloids through improved electrostatics

A schematic of the colloid separation method is depicted in figure 2.4. The device consists of two pairs of interdigitated microelectrodes patterned on either side of a microfluidic channel. Using a mixed AC/DC biasing scheme, it is possible to establish enhanced separation fields that cause particles in the flow to collect over the electrodes. Either pair of interdigitated electrode is supplied with a longitudinal high-frequency AC bias. At the same time, a transverse bias is applied across the channel by providing a DC offset for one pair of electrodes relative to the second pair. The power sources that drive both these electrode pairs are connected in-phase to control the uniformity of the transverse signal. At high frequency, the AC bias perturbs the vicinity of the electrodes rapidly to prevent EDL shielding effects. The magnitudes of the AC and DC components are adjusted in such a way as to ensure maximum separation forces over the electrodes that also penetrate out into the bulk regions of the channel.

Figure 2.5 shows a micrograph of a device with two pairs of electrodes embedded underneath a 100 nm

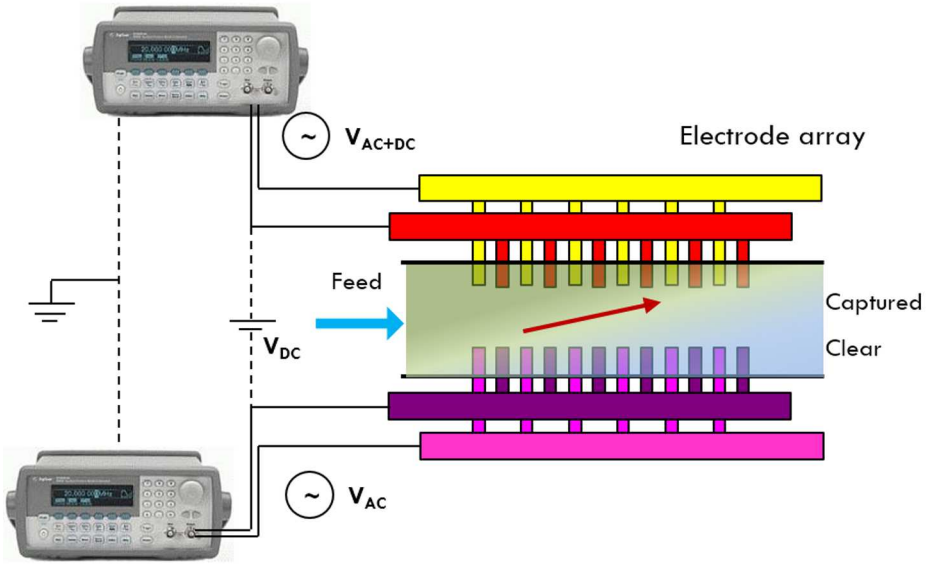

Figure 2.4: Schematic of improved nanoparticle separation using an AC/DC combined separation method.[3]

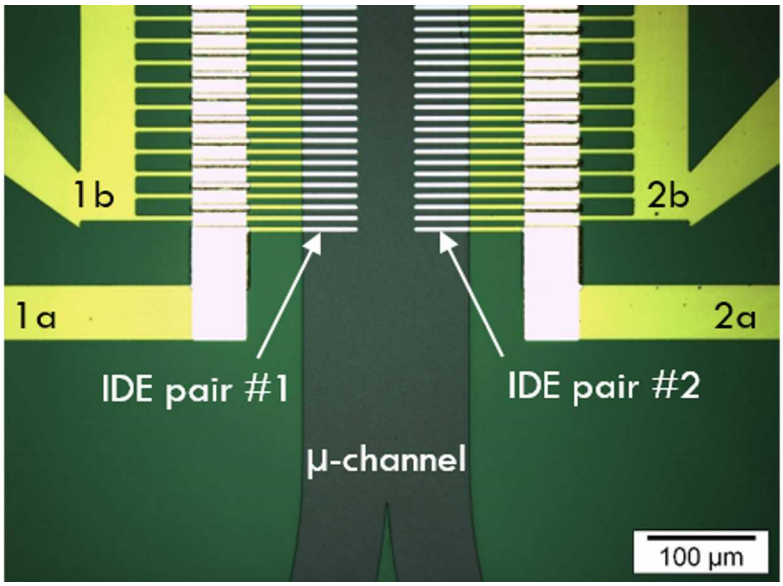

Figure 2.5: Micrograph of colloid separation chip showing two pairs of embedded interdigitated high-aspect ratio microelectrodes (5 μm wide) prior to microfluidic sealing.[4]

thick Si_3N_4 dielectric in a microchannel, prior to the final bonding of a PDMS microfluidic layer. The electrodes in each pair are 5 μm wide and 5 μm apart. Across the channel, electrode lengths are 50 μm and the gap between both pairs is 50 μm.

In this work, we have developed a method of enhancing the DEP forces over conventional 2-electrode

[3,4]Reproduced from [4], with permission from Springer Science+Business Media

AC-DEP through a mixed AC/DC excitation scheme. Our method uses two pairs of interdigitated electrode arrays in a longitudinal AC bias and a transverse DC bias. This novel combination collectively enables separation of sub-micron colloids from the bulk that normally do not respond well towards DEP separations. The method draws its advantages from the AC electroosmosis induced micromixing effects that break the shielding effects to enable further penetration of the separation forces in the bulk region of the microchannel. In chapter 3, we get a deeper understanding of the phenomena that enable our approach through analytical and computational models and experimentally demonstrate a device that takes advantage of these features.

Chapter 3

Enhanced colloidal separation from aqueous media

DC electrostatic strategies are typically ineffective for separation in aqueous suspensions. Counter-ions that migrate towards the electrodes to form the electrochemical double layer (EDL) cause rapid shielding of their surface potential ([1],[3]) so that it becomes practically impossible to sustain steady-state electric fields. When AC electrostatics is incorporated, however, the RC-constant of the EDL determines the effectiveness of the ion shielding. Depending on the magnitude and frequency of the AC-bias, ion shielding may or may not compete against electrostatic phenomena. At low frequencies, similar to the case of DC biasing, the ions migrate rapidly to charge the EDL capacitor. Since the time constant of the surface capacitance is short, it can charge completely during each cycle. All of the applied voltage decays within the EDL and hence the electrodes are apparently shielded from the bulk. Although these frequencies may be favorable for DEP separations from the standpoint of $K(\omega)$ values, the inability to sustain electrostatic separation fields can drastically hamper particle separation in this regime. When the biasing frequency approaches the RC-characteristic of the electrodes, this causes perturbation of the ions that would normally be trapped in the EDL. These ions are forced to circulate locally around the electrodes due to the phenomenon of electroosmotic pumping [37, 38, 39, 40, 29]. At the right conditions, this effect can be used to completely depolarize the microfluidic system while a separation field is at work. In this chapter, we discuss the formulation of a novel biasing scheme in microchannel systems to enhance the DEP separation fields.[1].

3.1 AC electrostatic field induced flow over electrodes

Figure 3.1 shows a schematic of AC electroosmotic (ACEO) flow around microelectrodes. During the first half of the AC cycle, the electrode voltage attracts counter-ions that are drawn from the bulk towards the edge. As they approach closer to the electrode, the electric field causes their path to curve tangentially towards the center of the electrode surface. During the second half of the cycle, when the polarity reverses, these ions from the proximity (which now assume the role of co-ions) are repelled away. Due to their existing

[1]Results discussed in this chapter are published in [4]. Reproduced with permission from Springer Science+Business Media.

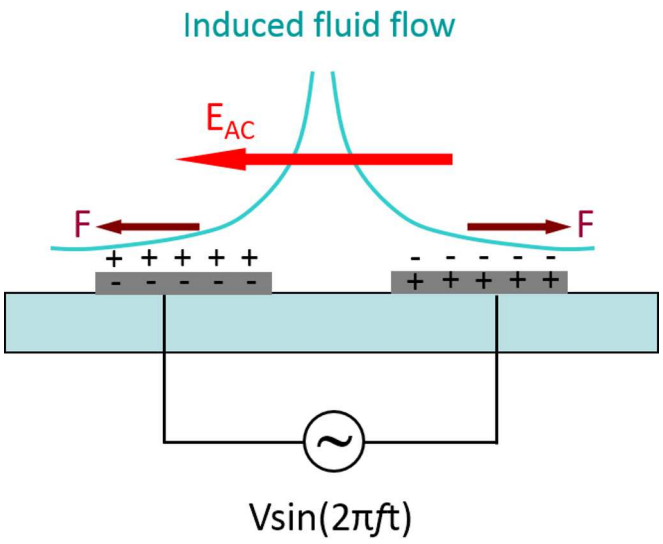

Figure 3.1: Schematic of electroosmotic flow cirulation around a pair of microelectrodes in AC bias.[2]

momentum from the first half-cycle, they are forced out tangentially towards the far edge. Eventually their path curves out away from the edge towards the bulk. The ACEO perturbation causes perfect circulation if the applied signal matches with the RC-constant of the microelectrodes. As a result of this local circulation of ions, an induced ACEO flow occurs and results in micromixing around the electrodes that prevents the formation of EDL. This can effectively short-circuit the surface capacitance to decrease the potential drop across the EDL. The effect is further accentuated at even higher frequencies when the perturbation is much faster than the response time of the circuit. Electric fields now penetrate out into the bulk electrolyte and the colloidal particles can experience the forces to be separated out. The design variables that can be used to tune the RC-constant of microelectrodes in a microfluidic system are:

a) the electrode geometry (width/spacing) and placement that affect the capacitance, and

b) the solution conductivity and permittivity that control the resistance and $K(\omega)$

3.2 Theoretical calculations of separation fields

3.2.1 Analytical modeling of ACEO effects

Ramos et al., have provided an elegant analytical model based on the above geometric and material parameters for determining the electroosmotic depolarization by micromixing around interdigitated electrodes

[2]Reproduced from [4], with permission from Springer Science+Business Media

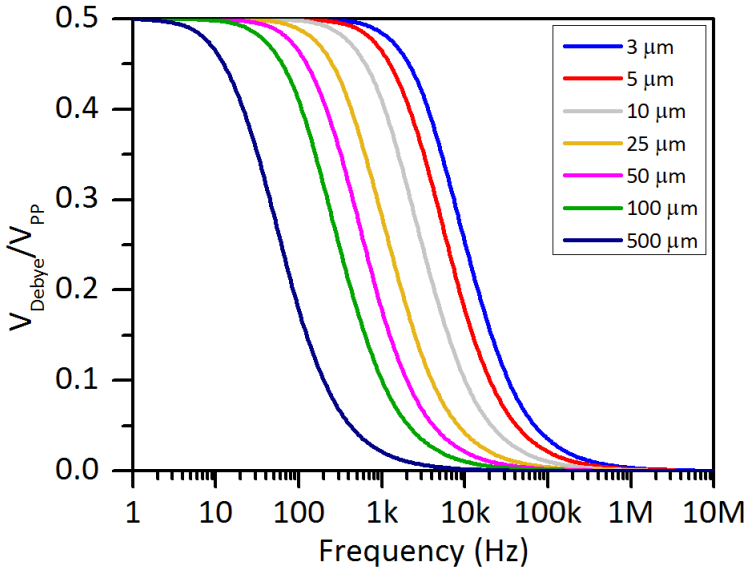

(a) Normalized voltage drop in the capacitive EDL compared to the resistive bulk v/s frequency for various electrode dimensions

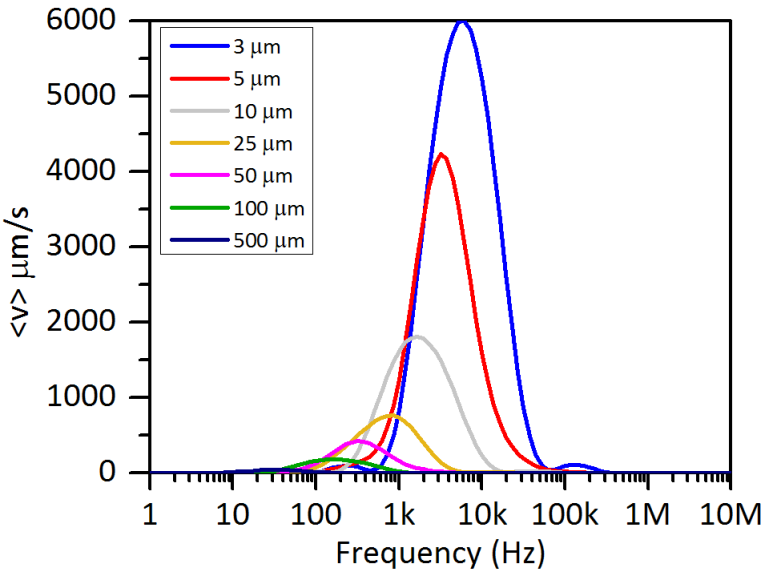

(b) Time-averaged ACEO velocity in the EDL v/s frequency for various electrode dimensions. <v> is maximized at $\Omega = 1$ and <v> $\longrightarrow$ 0 as V_{Debye} approaches 0

Figure 3.2: Calculations of AC electroosmotic flow parameters while breaking the EDL barrier.[3]

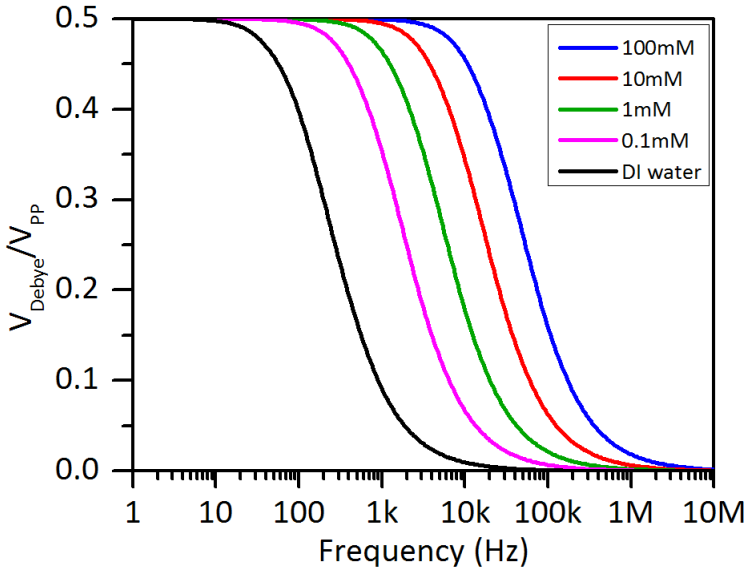

(c) Normalized voltage drop in EDL vs. frequency for 5 μm electrodes across various salt concentrations

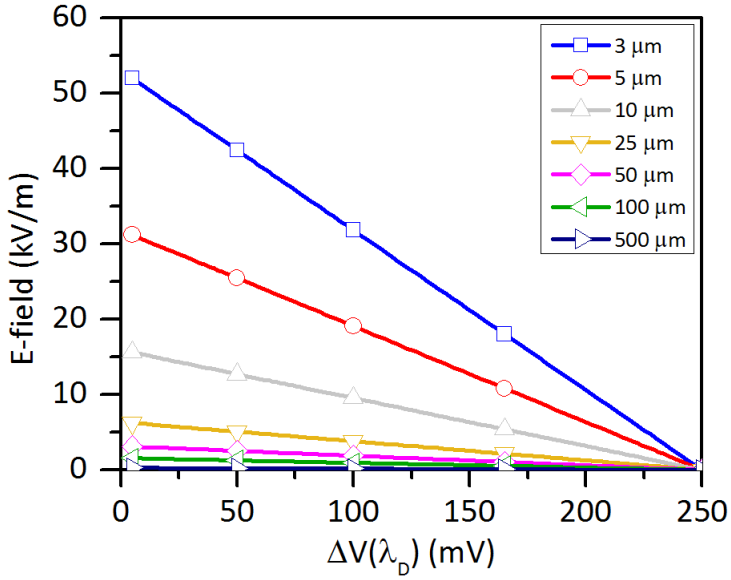

(d) Electric field magnitude at 1 V bias across the electroosmotic flow region v/s voltage drop in the EDL for various electrode dimensions

Figure 3.2: (contd...) Calculations of AC electroosmotic flow parameters while breaking the EDL barrier.[3]

[37],[40]. The local electric field lines around the microelectrodes follow well-defined semi-circular paths and can be modeled as a parallel circuit of infinitesimal current tubes flowing through two linearized EDL capacitors in series with a solution resistance. For sufficiently dilute media, a linear approximation is acceptable

[3]Reproduced from [4], with permission from Springer Science+Business Media

for the EDL capacitance to simplify and derive a closed-form solution. The voltage drop, V_{Debye}, in the EDL as a function of the peak-to-peak bias, V_{PP}, and the electrode width/spacing, z, is given by

$$V_{Debye} = \frac{V_{PP}}{2}\frac{1}{(1+j\Omega)} \tag{3.1}$$

where, $\Omega = \omega\frac{\pi\varepsilon_m}{2\sigma_m}\frac{z}{\lambda_D}$. The time-averaged electroosmotic velocity, $\langle v\rangle$ at the electrodes is given by

$$\langle v\rangle = \frac{\varepsilon_m V_{PP}^2 \Omega^2}{8\eta z\left(1+j\Omega^2\right)^2} \tag{3.2}$$

where, η is the dynamic viscosity of the medium.

The plots in figure 3.2 show the effects of AC electric field induced electroosmotic flow in overcoming EDL shielding of microelectrodes. The relative potential drop due to ionic shielding, V_{Debye}/V_{PP}, (figure 3.2(a)) has been determined by the circuit analysis model in equation 3.1. While at the lower frequencies most of the potential drop occurs within the EDL, the induced ACEO flow effect becomes apparent at intermediate and higher frequencies ($\geq$1 kHz). This can also be seen in figure 3.2(b) where the mean electroosmotic velocity (by solving equation 3.2) at the electrodes increases at these frequencies to its maximum value and then finally drops to zero again because the AC cycling is too fast for the ions to follow. When $f_{AC} \geq {}^1/_{RC}$, the EDL capacitance is completely disrupted by the micromixing and hence $V_{Debye} \longrightarrow 0$. Under this condition, all of the applied voltage extends out to the bulk solution, where the colloids may be perturbed. Figure 3.2(c) shows plots of V_{Debye}/V_{PP} for various ionic strength media. The threshold frequency for electroosmotic field enhancement increases with the salt concentration due to the decreased RC-constant as the Debye length decreases. We discuss this in further detail in section 3.4.3, accompanied by experimental results. The curves in figures 3.2(a) and 3.2(b) shift towards higher frequencies as the electrode dimensions decrease in size. However, the corresponding electric field strength is much higher because it inversely scales with the length. This is apparent in figure 3.2(d), which plots the electric field at 1 V_{PP} applied bias v/s voltage drop in the EDL across various electrode dimensions. The increase in electric field intensity as we scale down in size of the microelectrode geometry is advantageous for increasing the force of separation acting on the particles near the microelectrodes.

3.2.2 Numerical solutions

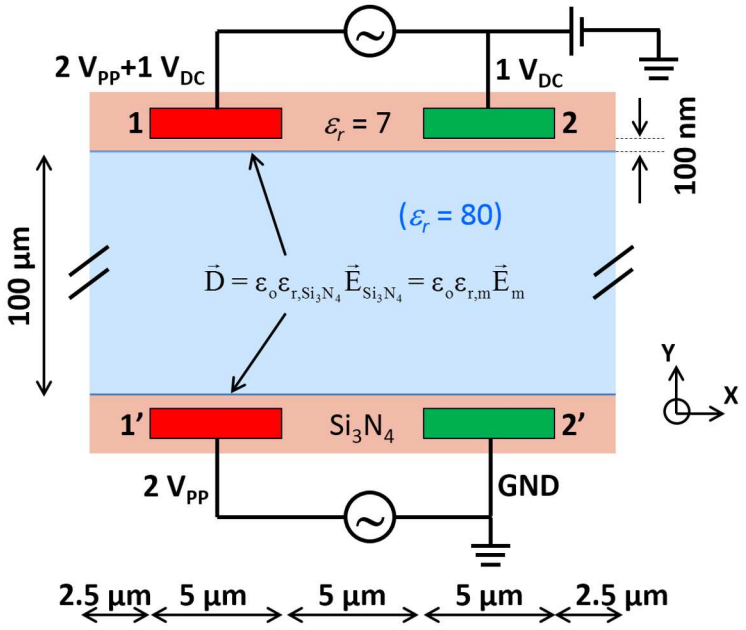

Figure 3.3: Schematic of the problem setup and 2-D finite element solution domain implemented for a 2-pair microelectrode system.[4]

The analytical model for ACEO depolarization of microelectrodes provides an elegant framework for enhancement of electric fields in microfluidic systems. In order to calculate the effect for two pairs of electrodes and mixed AC-DC biasing scheme, we resort to numerical simulations. Figure 3.3 shows a schematic of the computational domain in which finite element simulations were performed using Comsol Multiphysics 4.4®. The domain consisted of two pairs of coplanar electrodes, each 5 μm wide with 5 μm spacing, set 100 μm apart. The lengthwise high-aspect ratio of these electrodes ($\geq$20:1), and large center-to-center distance (100 μm) between the pairs when compared to the electrode width allows us to simplify the computational cost and complexity by reducing the system to a 2-D model domain. A 0.1 μm thin Si_3N_4 dielectric ($\varepsilon_r = 7$) was incorporated as a passivation layer over the electrodes, which were set to their respective biasing potentials to establish the mixed 2 V_{PP} AC + 1 V_{DC} transverse bias. A key requirement for this biasing approach is that $V_{PP} \geq V_{DC}$, failing which the DC potential will overwhelm the time varying component through EDL shielding of the electrodes. The microchannel region was filled with aqueous dielectric ($\varepsilon_r = 80$). Physical continuity at the interface between the dielectrics was enforced by maintaining compatibility between the displacement electric fields ($\overrightarrow{D} = \varepsilon_r \varepsilon_0 \overrightarrow{E}$) on either side, while a periodic boundary condition was applied on

[4]Reproduced from [4], with permission from Springer Science+Business Media

the transverse walls of the domain to ensure continuity of electric flux. Considering optimal high-frequency depolarization, the EDL capacitive effects were ignored, as were other effects such as electrothermal heating and flow induced charge separations.

Figure 3.4(a) shows the root-mean-squared (RMS) potential distribution in the channel. Due to high-frequency depolarization, it is possible to sustain a transverse gradient that aids in colloid separation. Partial asymmetry also arises in the solution due to this transverse bias across the channel, as indicated by the stretching iso-potential lines of the contours that do not align in perfect symmetry around the electrodes and at the longitudinal axis of the microchannel. This is also quantitatively demonstrated in figures 3.4(c) and 3.4(d). Figure 3.4(b) shows a comparison of the transverse electric field, E_y, across the channel, with and without the transverse bias. When a conventional AC-only bias is applied, the electric field completely decays within ca. 10 μm from the electrodes at either side of the channel and hence particles in the bulk will be mostly unperturbed. However, under the mixed biasing scheme, it is possible to sustain as high as 100 V/cm in the transverse potential gradient. Figures 3.4(c) and 3.4(d) show the respective transverse (E_y) and longitudinal (E_x) components of the electric field along various sections of the channel. In figure 3.4(c), the effect of the transverse DC bias on E_y can be seen from the fact that the longitudinal neutral plane of symmetry for the profile plots is shifted away from zero to a magnitude of -100 V/cm. Similarly, the effect of the additional DC bias on E_x is that the symmetry of figure 3.4(d) about $x = 0$ is broken. This is more pronounced at the vicinity of the electrodes. Within this proximity of the electrodes (1-5 μm), high field intensity (500-1500 V/cm) leads to the ACEO depolarization and also provides large trapping forces near the electrodes. As expected, the transverse electric field is maximum directly above the center of the electrodes, but the longitudinal component is maximized at the electrode edges. While the field decays to less than 10% of the peak value at 10 μm, we are still able to sustain $\sim$100 V/cm in E_y as E_x is practically zero in the bulk region. Furthermore, using the mixed scheme, we can establish a non-zero electric field profile across the channel and at least 10-fold larger gradients that are necessary in the proximity of the electrodes to overcome EDL shielding.

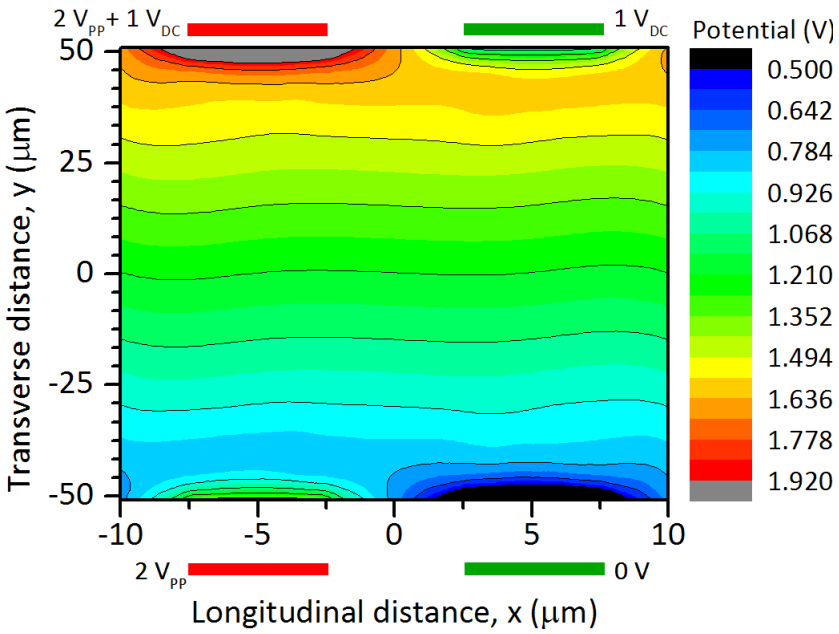

(a) Potential distribution in the channel when a 2 V_{PP} AC excitation is used along with transverse 1 V_{DC} bias

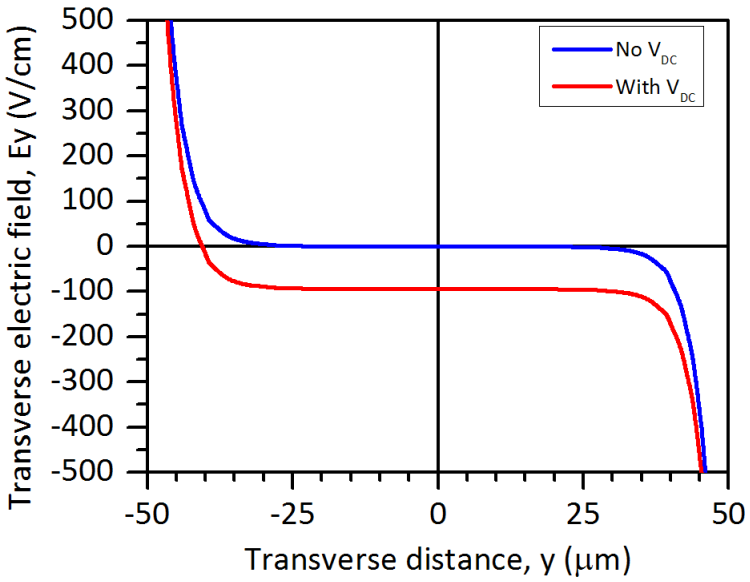

(b) Transverse electric field, E_y, across the channel on a section through the electrodes, with and without the transverse bias

Figure 3.4: Computational solution (RMS) of the potential and electric field distributions using our biasing scheme. The relative location of electrodes in 3.4(a), 3.4(c) and 3.4(d) is also shown schematically.[5]

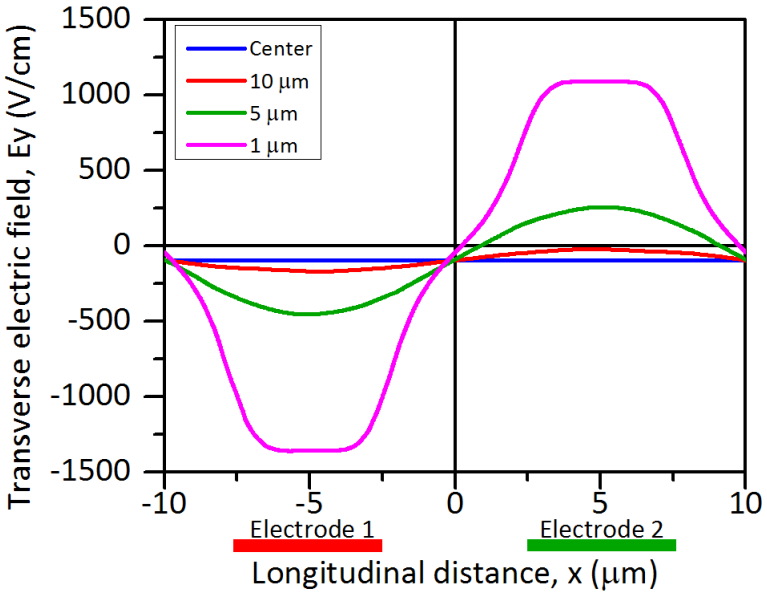

(c) Transverse electric field along various cross-sections parallel to the channel

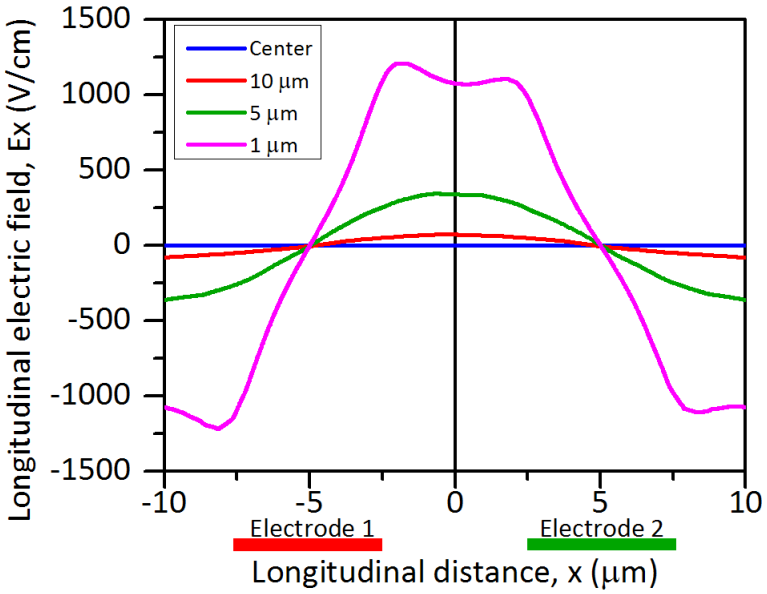

(d) Longitudinal electric field along various cross-sections parallel to the channel

Figure 3.4: (contd. . .) Computational solution (RMS) of the potential and electric field distributions using our biasing scheme. The relative location of electrodes in 3.4(a), 3.4(c) and 3.4(d) is also shown schematically.[5]

[5]Reproduced from [4], with permission from Springer Science+Business Media

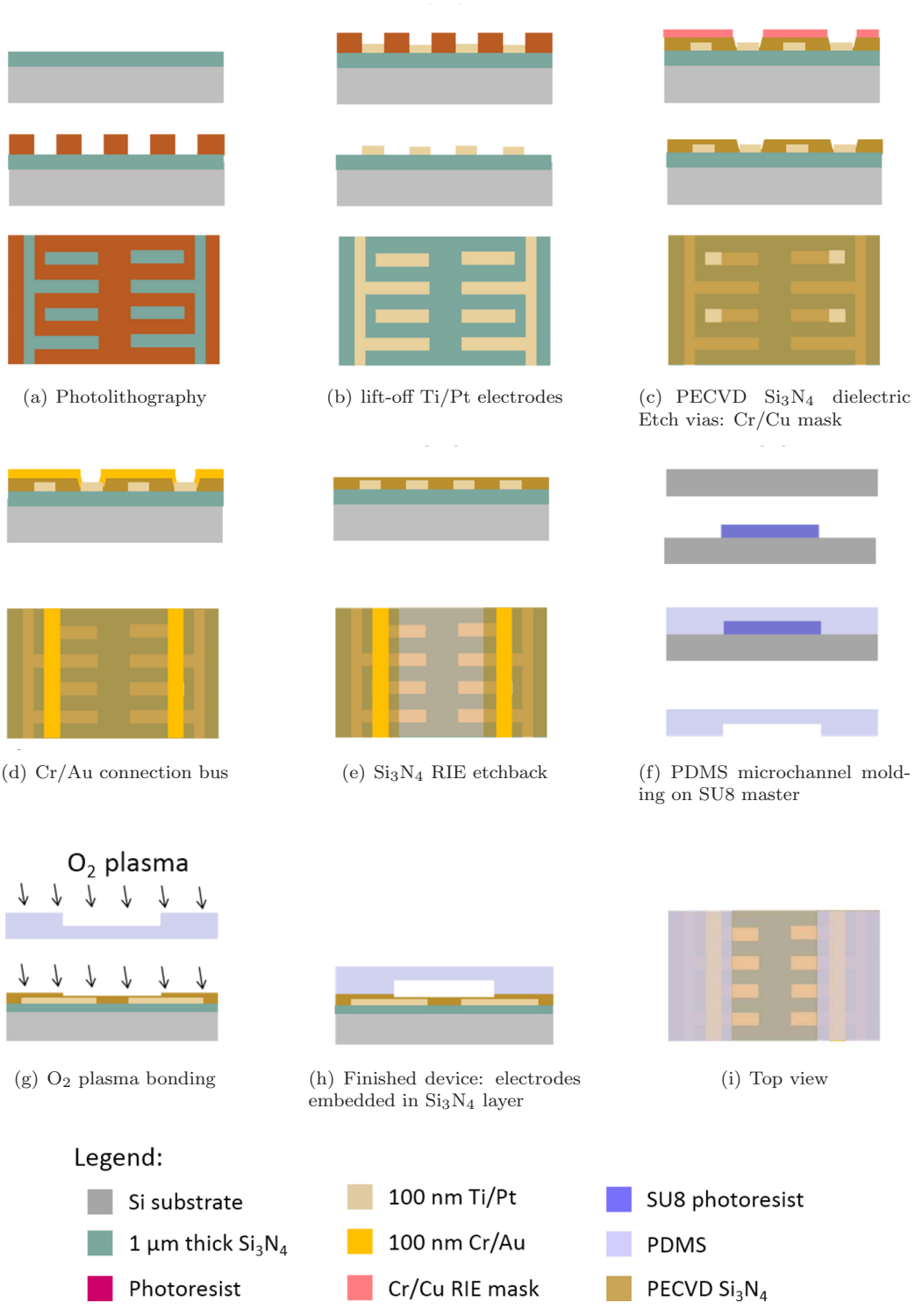

(a) Photolithography

(b) lift-off Ti/Pt electrodes

(c) PECVD Si_3N_4 dielectric Etch vias: Cr/Cu mask

(d) Cr/Au connection bus

(e) Si_3N_4 RIE etchback

(f) PDMS microchannel molding on SU8 master

(g) O_2 plasma bonding

(h) Finished device: electrodes embedded in Si_3N_4 layer

(i) Top view

Figure 3.5: Fabrication steps for the microfluidic colloid separation device.[6]

[6]Reproduced from [4], with permission from Springer Science+Business Media

3.3 Experimental

3.3.1 Microfabrication

Figure 3.5 shows a step-by-step fabrication sequence for the microfluidic colloid separation device. The substrate used is a 500 μm thick silicon wafer with 1 μm thick LPCVD silicon nitride that provides complete electrical isolation. Interdigitated electrodes are patterned through conventional photolithography of a bi-layer photoresist combination of lift-off resist LOR3A and photosensitive Shipley S1805 in step (a). This is followed by e-beam evaporation of 100 nm thick of Ti/Pt in a CHA evaporator and lift-off in NMP solvent (Microchem Remover PG) at $\sim 70°$C to reveal the electrodes in step (b). A 400 nm thick dielectric layer of PECVD Si_3N_4 is deposited using a dual frequency process in STS PECVD tool to cover the electrodes and passivate the metal surface from Faradaic reactions at high applied bias. In step (c), vias in the Si_3N_4 layer are isotropically etched using Freon RIE to reveal openings on the second electrode of each pair. This step uses a 100 nm thick Cr/Cu lift-off patterned layer as the etch mask. Subsequently, a 100 nm thick Cr/Au connection bus is sputtered (AJA deposition systems) and wet etch patterned on either side to complete the connections. Steps (c) and (d) are crucial for the electrical connections, while maintaining electrical isolation between the electrodes within each pair. In step (e), the Si_3N_4 dielectric is thinned down over the electrodes to $<$200 nm in the microchannel region using a Freon-based RIE process (Plasmalab RIE system). The microfluidic layer is fabricated out of PDMS molding in step (f). A 25 μm thick SU8 negative master of the microchannel is patterned using SU8-25 negative resist on a 500 μm thick bare silicon wafer. the SU8 is hardbaked to form a permanent structural layer as the negative master. A degassed mix of Sylgard® PDMS prepolymer and curing agent (10:1 ratio) is poured over the template, cured at 65°C for 6 hours, and peeled away to reveal the microchannel. Ports are cored into the PDMS for the electrical and fluidic connections. The substrate and PDMS microfluidic layer are irreversibly bonded after O_2 plasma treatment (step (g)) in a diener benchtop barrel plasma RIE. Immediately following plasma activation, precise alignment of the PDMS channel to the electrodes is performed in a Carl Suss MJB3 mask aligner (step (h)). Finally, tubing is inserted into the fluidic ports to form a leak-free compression fit. Figure 3.5(i) shows the top view schematic of a cut-section of the complete microfluidic device with embedded interdigitated electrodes inside the PDMS microchannel.

3.3.2 Sample preparation and experimental protocol

All separation experiments were performed using 0.75 μm beads (Thermo Scientific), with surface carboxylic acid functional groups that stabilized the suspension. Low conductive solutions were prepared by suspending the particles in Millipore® water, and the high salt buffer was made using 0.01X PBS for an ionic strength of 1.5mM. In both cases, the concentration of the colloids was ca. 10^7 particles-per-mL and the suspensions were agitated prior to each experiment. During the separation experiment, the colloids were fed into the microfluidic chip through two inlet channels at $\leq$30 nL/min using a syringe pump (Harvard Apparatus). Each pair of electrodes was electrically biased by a signal generator (Agilent 33250). Both the function generators were coupled through the external 10 MHz timebase card, and the waveforms were synchronized in-phase to an accuracy of $\pm$20 Hz using the internal triggering capability. The additional DC offset was applied for one pair of electrodes to establish the transverse DC bias. Particle flow and separation in the microchannel was optically imaged (Nikon FN-1 microscope) with a 20X magnification high-NA objective.

3.4 Results

3.4.1 Capture analysis and quantification of separation

Separation experiments were performed with the microfluidic device with two arrays or interdigitated electrodes, using 0.75 μm diameter particles in DI water that served as a low conductive medium. Figure 3.6 shows a series of time lapse snapshots of the colloidal particles getting collected between the 5 μm wide electrodes when a 2 V_{PP} 1 MHz AC signal was used. The transverse DC bias across the microchannel between the top and bottom electrode pairs was +1 V. Upon biasing the system, we observed particles gradually getting trapped over the top electrode pair and near the tips of the bottom electrodes. Some of the particles from the channel gap were also captured. Within about 60 seconds of applying the AC/DC bias, the colloids had redistributed themselves to the collection zones.

We analyze the timelapse capture experiment and extract quantitative information of relative particle separation by counting particles along a transverse profile using mean gray values of the pixels in the image. Figure 3.7 shows the analysis scheme and separation profile across the microchannel that has also been applied for the experiment shown in figure 3.6. We count the particles by comparing their gray value (dark) in contrast with that of the background (brighter). Every time a particle gets captured at a pixel, the intensity of that location shows as a local minimum in the gray value profile. The pixel size of $\sim$0.75 μm $\times$ $\sim$0.75 μm matches with the size of the particle and simplifies the counting procedure by minimizing the issue of false positives by eliminating duplicate counting events between adjacent pixels. Given the

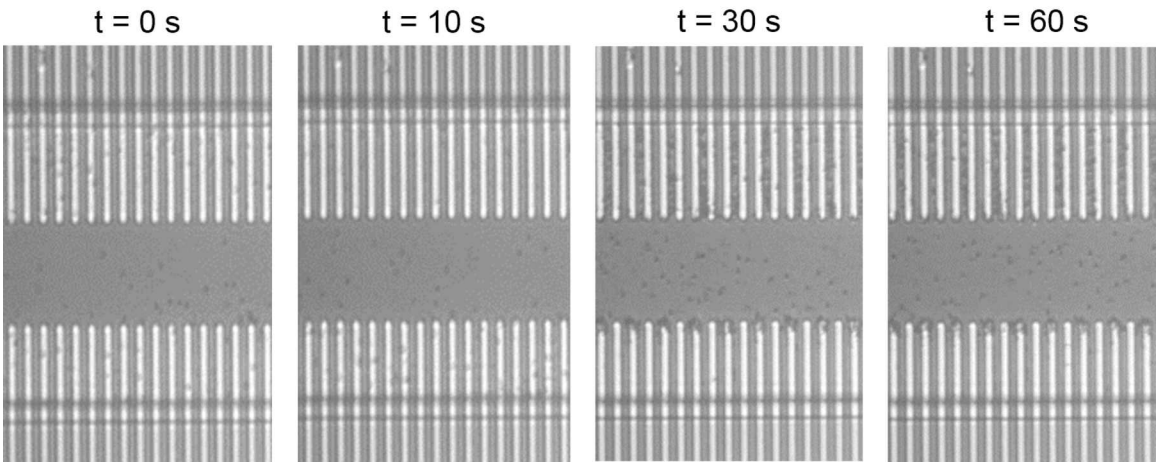

Figure 3.6: Snapshots of colloid separation (0.75 μm particles) using 2 V_{PP} and 1 MHz AC bias on each electrode pair, with +1 V_{DC} bias for the top electrodes. Sequential images were extracted at t = 0 s, 10 s, 30 s and 60 s, respectively, and show progressive increase in the collection with time.[7]

inherently heterogeneous nature of the background image and its gray values, we only count the existance of a particle when the decrease in gray value is statistically significant in comparison with overall noise, i.e. if it exceeds the standard deviation of all background points in that section. As shown in figure 3.7(a), two principal cross-sections of interest are directly over the electrodes (AA′) and through the midline of the electrode spacing (BB′). The mean grey values of the background before the separation experiment (blue) and after t = 60 seconds of separation (red) have been superimposed for both these cross-sections in figures 3.7(b) and 3.7(c), respectively. Due to the chosen AC frequency of this experiment, we observed that the colloids preferentially accumulated in the electrode gaps and the grey values also reflect this trend. The local minima in the red curves follow the occurrence of the colloidal particle (dark) and, hence, the grey value is lower in these collection zones. More colloids are collected at the top electrodes and the tips of the bottom electrodes as seen by the grey value distributions. While the gray values in the bulk region overlapped, as expected, a few local minima are also indicative of the instantaneous occurrence of some of the particles merely in the flow. The difference in grey values between separation and background for the BB′ cross-section within the electrode pairs has been used to determine the relative particle concentration of each snapshot. By averaging this over all points along the length of the electrodes, we obtain the relative concentration as a percentage. This is plotted for the electrode regions of each snapshot in figure 3.7(d). As seen in figure 3.7(d), the particle concentration using our novel separation approach and electrostatic enhancements increases over time until 71% at t = 30 s and saturates to ca. 75% by t = 60 s. We contrast the quantitative results of our approach against a conventional AC-only biasing scheme in section 3.4.2.

[7]Reproduced from [4], with permission from Springer Science+Business Media

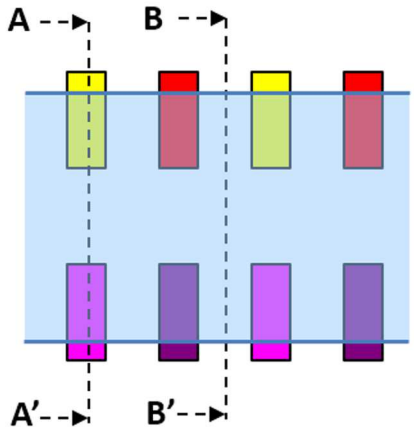

(a) Schematic cross-sections AA′ (overlapping the electrodes) and BB′ (in-between electrode gap) that were analyzed across the channel

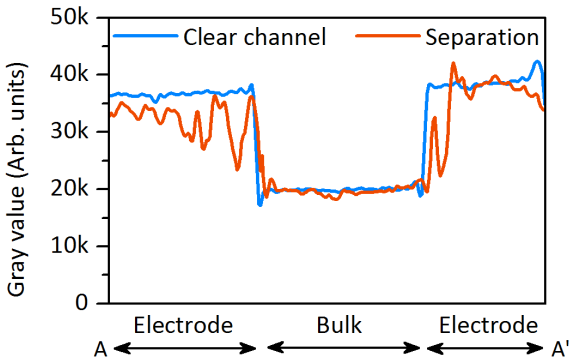

(b) Profile through section AA′ on top of electrodes

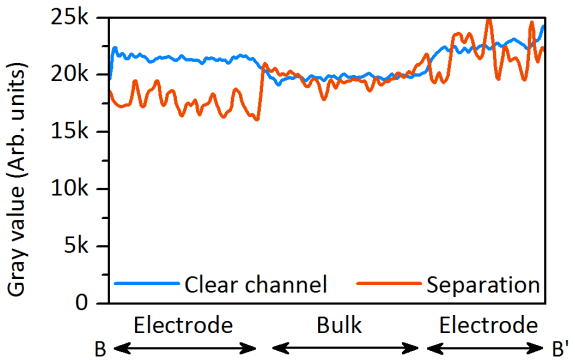

(c) Profile through section BB′ over the gap between the electrodes

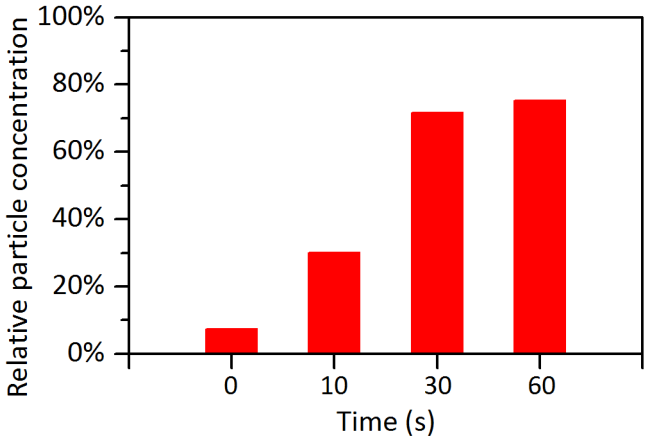

(d) Relative particle capture amount near the electrodes

Figure 3.7: Quantification of particle separation over time through mean gray value analysis of profiles across the channel.[8]

[8]Reproduced from [4], with permission from Springer Science+Business Media

3.4.2 Effect of biasing conditions on separation

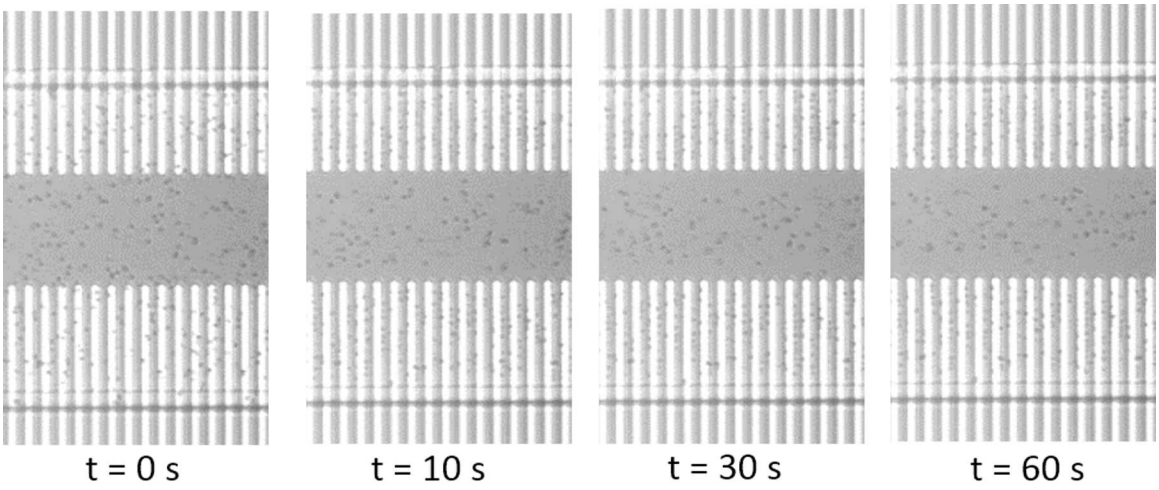

(a) In the AC-only bias, fields were localized over electrodes and the bulk stream was unaffected

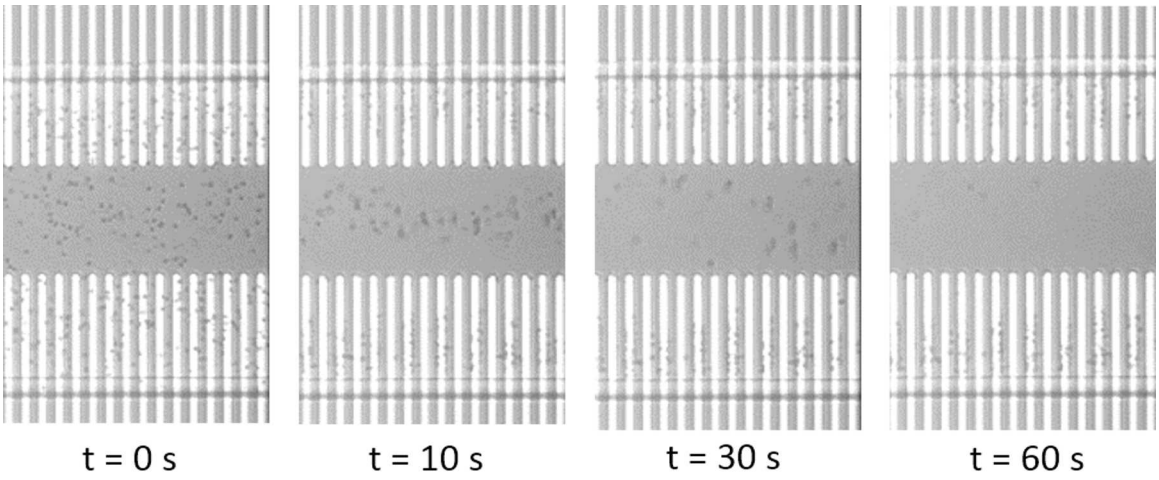

(b) Including the transverse DC bias enabled capture of the colloids from the bulk stream

Figure 3.8: Sequential snapshots of colloid separation (0.75 μm particles) without and with the mixed 1 V_{DC} transverse bias in addition to the 10 V_{PP} at 100 kHz AC bias.[9]

During separation, incorporating the additional transverse DC bias enables the electric field to penetrate fully across the channel for improved capture of the colloids from the bulk region of the channel. We experimentally verified the improvement over conventional AC-only DEP as a control. In the latter experiment, we performed DEP by applying only the AC bias (in-phase) at both pairs of electrodes. Figure 3.8 shows time lapse snapshots (t = 0 s, 10 s, 30 s and 60 s) of colloid separation without DC bias (figure 3.8(a)) and with +1 V DC bias (figure 3.8(b)). The AC bias applied was 10 V_{PP} and 100 kHz at which we can expect positive

[9]Reproduced from [4], with permission from Springer Science+Business Media

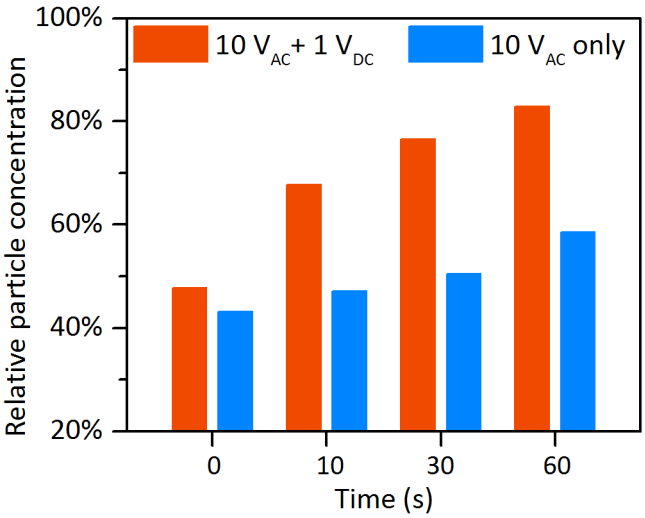

(a) Quantification at the electrodes

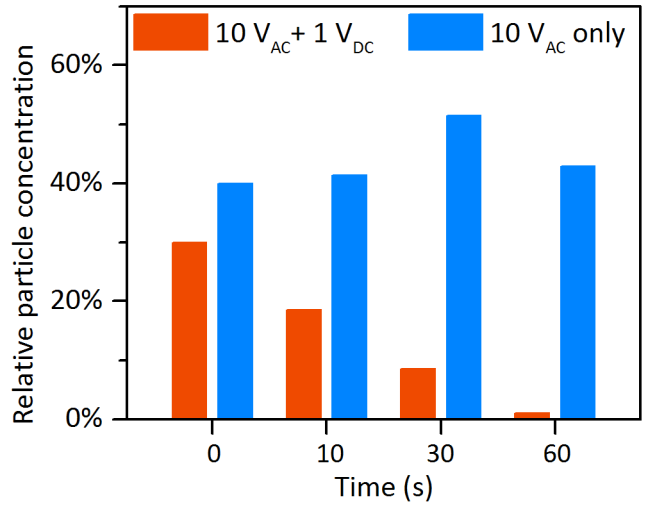

(b) Quantification in microchannel bulk

Figure 3.9: Relative particle concentration v/s biasing scheme as determined from gray value analysis.[10]

DEP effects on the colloidal beads. The relative particle concentrations have also been plotted for both cases over the electrode (figure 3.9(a)) and bulk (figure 3.9(b)) regions. As seen from the time lapse sequence of figure 3.8(b), the presence of a transverse DC bias greatly improved the capture form the bulk region outside the electrodes and most of the particles were trapped by t = 60 seconds. This is also consistent with the measured increase in concentration over the electrodes to 83% (figure 3.9(a)) and decrease from 30% to zero in the bulk region (figure 3.9(b)). In contrast, the AC-only case (figure 3.8(a)) showed particle trapping only over the electrodes (ca. 58%, as seen in figure 3.9(a)). The bulk region was largely unaffected, as seen

[10]Reproduced from [4], with permission from Springer Science+Business Media

in figure 3.9(b), except for minimal extraction from the fringing regions at the electrode tips. In this case, electric fields were localized over the electrodes and did not sufficiently extend across the microchannel.

3.4.3 Effect of salinity on separation

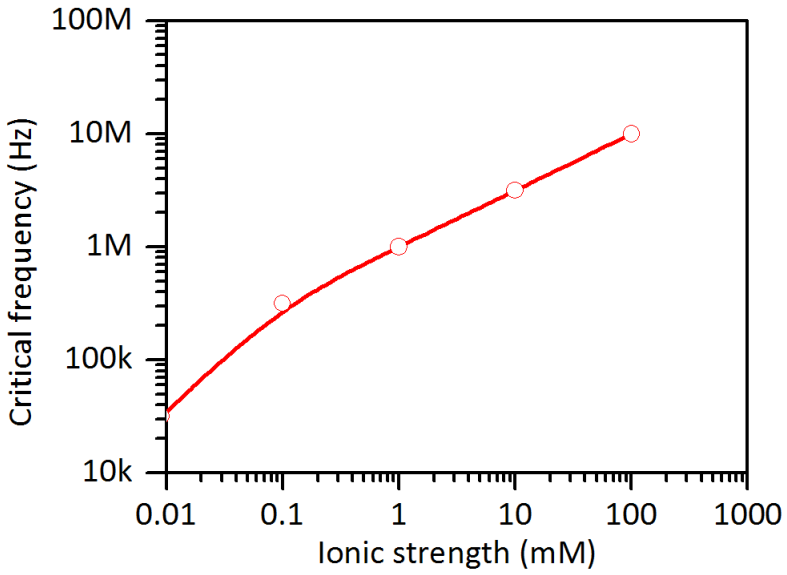

Figure 3.10: Variation of minimum ACEO depolarization frequency with salinity of separation medium.

The overall salinity of the background medium has dual effect on the separation capacity of the microfluidic system. Firstly, the ACEO depolarization frequency varies with salt as it follows the changes in the RC-characteristics of the microelectrodes as we had mentioned earlier in section 3.2.1 and figure 3.2(c). Secondly, the relative polarizability of the particles depends strongly on the conductivity of the medium as well and this directly affects the $K(\omega)$ values for both DEP and twDEP methods (figure 2.3). In figure 3.10, we plot (on a log-log graph) the critical frequency corresponding to the onset of ACEO depolarization v/s salinity. As we can expect from the shifting of the RC-constant, the critical frequency also strongly shifts rightward towards higher biasing frequencies when the salt content increases. We observe that the theoretical critical frequency shifts by one-half order of magnitude for every decade increase in salinity. Hence, in order to compare the DEP performance of two systems of different salt content, we cannot apply identical excitation frequencies. Rather, the critical frequency as seen in figure 3.10 dictates the lower bound for the AC-frequency in each case. For example, while we can apply a 100 kHz biasing frequency for DI water or low conductivity buffers, a more salty solution such as 0.01X PBS (~1.5mM) needs a minimum AC-bias frequency in the 1-10 MHz range.

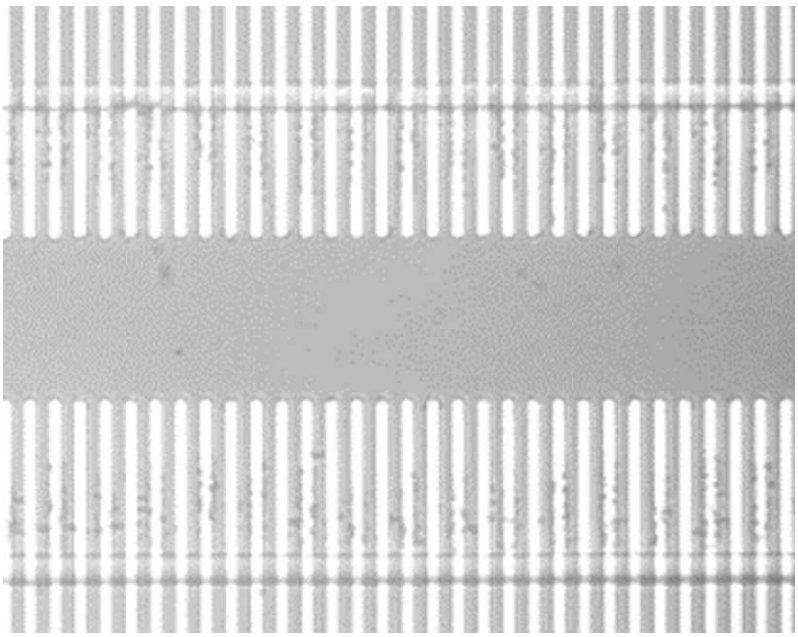

(a) Low salt (DI water) at 100 kHz

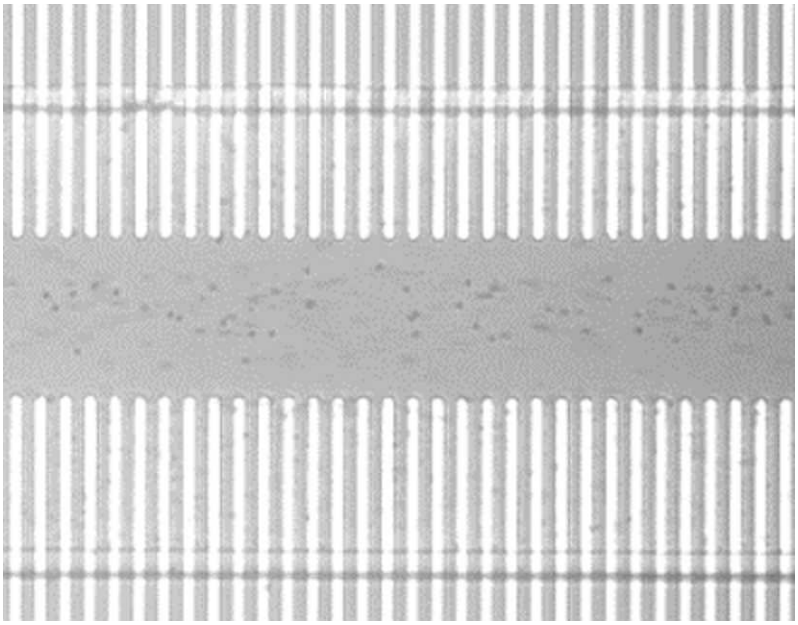

(b) High salt (0.01X PBS) at 10 MHz

Figure 3.11: Comparison of colloid separation profiles at t = 60 s between low and high conductivity solutions. The DEP excitation signal used was 10 V_{PP} AC bias and 1 V_{DC} transverse bias.[11]

Experimentally, the effect of salt concentration is analyzed by comparing low/high salt media (DI water/0.01X PBS) in figure 3.11. The separation results were obtained at t = 60 seconds in both cases, with an applied AC bias of 10 V_{PP} along with the transverse +1 V_{DC} bias between the top and bottom

[11]Reproduced from [4], with permission from Springer Science+Business Media

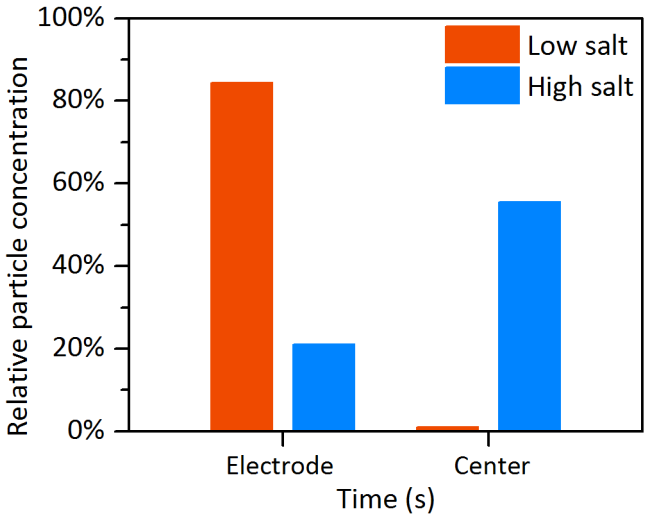

Figure 3.12: Relative particle capture at both electrode and bulk regions for low and high salt conditions as determined from gray value analysis of figure 3.11.[12]

electrode pairs. Figure 3.11(a) shows the result for low conductive case (DI water) at 100 kHz and this is identical with the t = 60 seconds snapshot from figure 3.8(b). The particles travelled towards the electrodes and were fully captured from the bulk as well due to the transverse electric field. The particle concentration data (figure 3.12) also shows high accumulation at the electrodes (83%) and complete depletion from the center regions of the microchannel. At high salt content in the case of 0.01X PBS at 10 MHz, however, the increased conductivity of the medium competes with the polarizability of the particle and hence $Re\,(K\,(\omega))$ <0 throughout the frequency spectrum. As a result, the colloidal particles can only experience negative DEP forces, which was apparent in figure 3.11(b). The relative particle concentration (figure 3.12) followed the exact opposite trend of low salt. At the electrodes, the collection was 4-fold lower (21%) and it increased to over 50% in the bulk region. From the images, the colloids appeared to aggregate at the edges of the electrodes and those in the bulk region of the channel were repelled away towards the centerline of the channel and focused into a narrower stream. We observe that the overall background salinity adds additional complexity to the separation system; nevertheless, knowing this information beforehand can be useful in designing well-defined spatial collection zones. Figure 3.13 shows schematics of separation systems that would fractionate sub-micron particulates using our enhanced DEP method and the filtrate/rejectate streams can be designated on the basis of feed salinity as well as relative particle polarizability.

[12]Reproduced from [4], with permission from Springer Science+Business Media

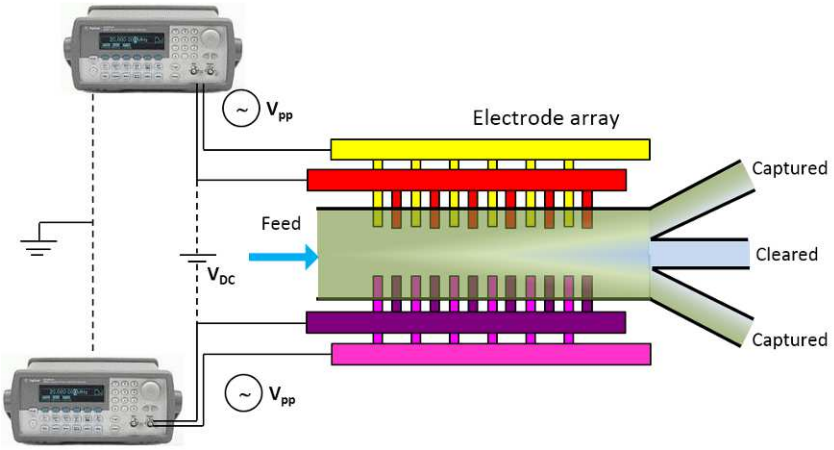

(a) Collection in low salinity

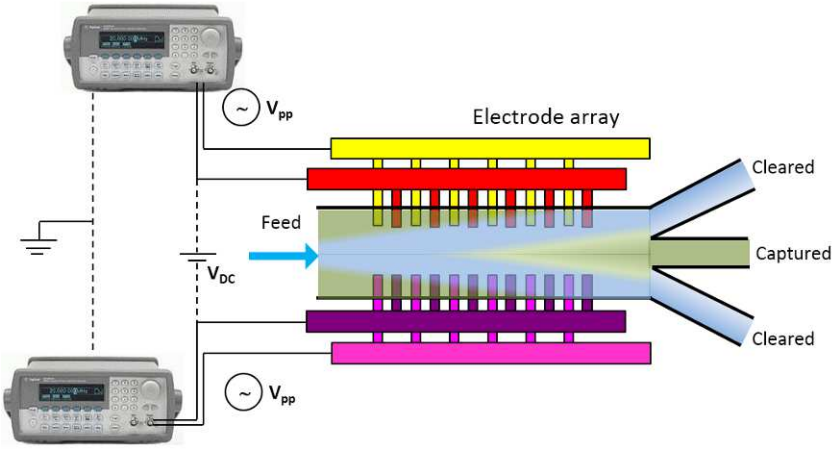

(b) Collection in High salinity

Figure 3.13: Schematics of colloid separation systems showing fractionation and collection zones designed on the basis of background salinity and particle properties.

Chapter 4

Direct molecular sensing with FETs: the role of salt ions

The second part of this thesis is based on a sensing problem. This study is based on an effort to develop label-free field effect nanobiosensors with improved sensitivity by overcoming the screening limitations due to salt ions. In this chapter, we present an overview of the field-effect nanobiosensors and identify the issues associated with excess salt ions in the background. As our approach to solve this problem is to implement an on-chip desalting scheme, we also need to establish certain constraints so that molecular stability will not be compromised. We experimentally examine the effect of diluting salt concentrations on the hybridization efficiency and dehybridization instability of miRNAs to get a better understanding of these limits.

4.1 Biosensors based on field-effect devices

Field-effect biosensors provide a label-free method for detection of biomolecules. Label-free electrical detection schemes eliminate the need for complex and expensive instrumentation so that diagnostic platforms can be made more portable and serviced at the point-of-care. Based on ion sensitive field-effect transistors (ISFETs) developed initially by Bergveld [41], decades of subsequent advances in indirect pH-based detection [42] have met with success towards DNA sequencing [43, 44]. This culminated in the commercial demonstration of a fully integrated CMOS chip for genome sequencing by Rothberg et al. [45].

In the last 15 years, following the early demonstration of nanowire-based FET devices by Cui et al. [46], direct molecular sensing of analytes has been achieved for a range of small analytes that include nucleic acids, proteins and other biomolecules [47]. Bunimovich et al. [48] used silicon nanowire arrays to detect 16bp oligonucleotides up to nanomolar concentrations and used this platform to study and quantify kinetic parameters of the hybridization reactions. Gao et al. [49] used silicon nanowire arrays with peptide nucleic acid (PNA) capture probes to detect complimentary target DNA at 10fM limit of detection (LOD). Zhang et al. [50], showed a similar assay to detect microRNAs at concentrations as low as 1fM and also performed studies of detecting single base mismatches. Dorvel et al. [51] have shown nanowire FETs with improved gate dielectrics and molecular binding protocols to achieve 1fM LOD, and further studied the effect of geometric

parameters on sensitivity to achieve ∼0.1 pg/mL detection of mouse IgG [52]. Stern at al. [53] performed one of the first experimental studies of salt ion screening of nanowire FET assays using streptavidn-biotin detection. Zheng et al. [54] were able to demonstrate multiplexed detection with the nanowire FET sensors and used monoclonal antibodies to achieve 0.9 pg/mL LOD to detect PSA cancer markers on silicon nanowire arrays. Krivitsky et al. [55] combined the dual capability of silicon nanowire forest for preconcentration with nanowire FETs to extract, concentrate and detect 50pM of troponin-T from blood samples. Other studies have included virus detection with nanowires as well. Patolsky et al. [56] have also shown capture of single influenza virus particles on silicon nanowires, while Ishikawa et al. [57] have developed antibody mimic proteins (AMPs) in conjunction with In_2O_3 nanowires for sensing of SARS virus at sub-nanomolar concentrations.

While nanowire-based devices have benefited from the scalability of nanofabrication techniques towards multiplexing [54], considerable advances from the semiconductor side have also improved the sensitivity and robustness through incorporation of high-K gate dielectrics [58, 51] and optimization of device geometry [59, 60]. However, given the inability for direct electrical detection from physiological samples because of screening limitations, a commercially viable solution has been elusive for integrating nanowire FETs within portable-scale diagnostics. In the subsequent sections, we analyze the screening problem both from the standpoint of device sensitivity and molecular stability.

4.2 The working concept of a nanowire biosensor

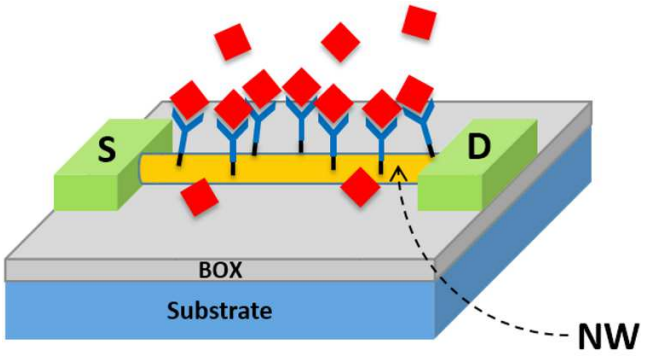

Figure 4.1: Schematic of a field-effect nanowire biosensor.

Figure 4.1 shows a schematic of field-effect nanowire biosensor. The system consists of a Si-nanowire between two electrodes whose surface is functionalized with specific receptors that recognize and bind only to

the target molecules. The electrodes are protected from the solution by an oxide layer to avoid any undesired conductance change. Some of the target analytes diffuse through the solution and reach the nanowire to get captured by the receptors. The charge density of the analyte, σ, (-ve charge for DNA, and pH dependent charge for proteins) interacts with the nanowire to induce changes in device conductance, G, as follows:

$$\Delta G = \frac{\pi d \mu \sigma}{L_{NW}} \tag{4.1}$$

where, $G_0 = \dfrac{e\mu N_D \pi d^2}{L_{NW}}$, N_D is the number density of charge carriers, μ is the mobility, d is the diameter of the nanowire and L_{NW} is its length. The sensitivity of the nanowire, S, which is the relative change in conductance to its intrinsic conductance is given by

$$S = \frac{\Delta G}{G_0} = \frac{4\sigma}{edN_D} \tag{4.2}$$

which shows that scaling down in the critical dimension, d of the nanowire-FET helps achieve improved sensitivity. However, the extent of device transduction by the analytes, i.e. σ, is adversely affected by the screening from salt ions in solution which causes loss of device sensitivity.

4.3 EDL screening effects on the response of nanobiosensors

Physiological fluids, such as blood, plasma and serum, have very high salt content with ionic strength of up to 150mM. At these concentrations, $\lambda_D < 1$ nm. In a typical DNA hybridization reaction over a sensor, negative charges are added or an associated change in pH follows when a target DNA strand (1-10 nm) hybridizes with a capture probe functionalized on the sensor surface. In principle, the excess (or deficit of) molecular charge from the analyte residing on the surface of a biosensor can change the gating condition and, therefore, conduction through the device 4.1. However, most of these charges will likely be outside the Debye length limit of the EDL, as described in equation 1.1. As a result, surface charges residing on biomolecules cannot actively participate in modulating the gate voltage of the FET and would appear to be electrically invisible to the sensor. The schematic in figure 4.2(a) describes this scenario.

Nair and Alam have extensively analyzed factors that affect the performance of field-effect nanobiosensors [61, 62, 63]. In their numerical simulations of a test charge transducing a nanowire from its vicinity, in different salt solutions, their findings showed a dramatic two-order of magnitude difference in sensitivity between low salt ($\sim$1mM) and high salt ($\sim$100mM) conditions. Sorensen et al. [64], in their analysis of the

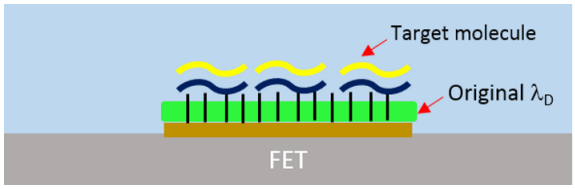

(a) Debye length in high salt is too small and screens the analyte charge from the sensor

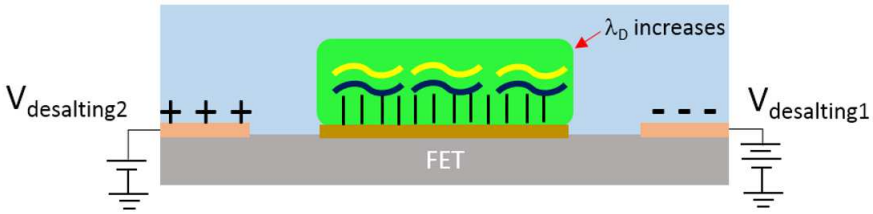

(b) Desalting aorund the device extends the Debye length to include analyte charge

Figure 4.2: Schematic of improved field-effect biosensing of analytes with localized electrostatic desalting.

screening effect on nanowire performance, have shown how the relationship between the critical geometric dimensions of a nanowire (its radius or thickness) and λ_D can affect sensitivity. A dimensionless sensitivity parameter, Γ_l, also captures the effect of salt concentration through λ_D:

$$\Gamma_l = 2\frac{\dfrac{R}{R+l}}{1+\sqrt{\dfrac{R}{R+l}}\exp\left(\dfrac{l}{\lambda_D}\right)} \tag{4.3}$$

where, R is the radius of the nanowire and l is the thickness of the analyte layer. The sensitivity (Γ_l) decreases exponentially with decrease in λ_D due to salt concentration. In order to maximize both signal and sensitivity, the physical and phenomenological lengthscales, l and λ_D respectively, must meet. Thus, it is essential to minimize the ion concentration near the surface so that the largest fraction of the molecular charge from the target can be transferred to the device. On the face of it, swapping solutions to low salt buffers ($\leq$1mM) may appear to easily solve the sensitivity issue. However, as we discuss in section 4.5, the salts play a strong role in molecular stability. Therefore, an alternate approach that does not compromise the analytes is necessary.

A method of reversible depletion of the salt environment can be envisaged in which, the application of electrophoretic forces or a pair of electrodes in small voltage bias can absorb salt ions away from the vicinity of the sensor (figure 4.2(b)). From the point of view of device sensitivity, this desalting effect could increase

the apparent Debye length sufficiently that the analytes are well within the modified EDL around the device. Under this condition, a greater fraction of the molecular charge will be coupled with the sensor. Sensing in this depleted condition, before ions diffuse back, would elicit maximum response from the device. In this study, we have sought to implement *in-situ* desalting of the field-effect nanobiosensor so that its sensitivity can be improved for detection from realistic salt conditions.

4.3.1 Effect of orientation and density of analytes at the sensor surface

The size of analyte molecules and their geometric orientation can directly affect the effectiveness of transduction. miRNAs are 22bps long (ca. 7.1 nm long and 2.4 nm wide), with two complete helical turns. A couple of orientation scenarios that are commonly seen are depicted to scale in the schematics of figure 4.3, depending on the choice of linker chemistry [65], which is usually a silane-based self-assembled monolayer (SAM) on the gate oxide ($HfO_2/Al_2O_3/SiO_2$). The SAM itself is generally 3-carbon atoms or longer and can offset the molecule by at least 10 Å from the sensor. The molecules can be vertically oriented (amine-epoxy chemistry) as shown in figure 4.3(a) or horizontally oriented flat (DNA backbone-amine chemistry) on the sensor as shown in figure 4.3(b). Either case has its own advantages and shortcomings. In the vertical orientation, the molecules tend to be more closely packed and hence this configuration maximizes the number density of analyte capture per unit area. However, even at a reduced salt concentration of 10mM, about 70% of the analyte charge will be outside λ_D and unlikely to perturb the sensor. In the flat orientation, conversely, the molecules are much closer to the surface and most of the analyte charge lies just about within λ_D at 10mM and can transduce more effectively. However, the number density of bound molecules is several folder less than in the vertical orientation because each molecule occupies a greater footprint on the surface and fewer SAM sites are linked. Thus, the comparison between both configurations reveals that it is a trade-off between proximity and number density of molecules on the sensing surface. At physiological concentrations (>100mM), the analyte lies almost entirely outside λ_D in both cases and completely screened from the device. In order that the analyte (and therefore its charge) is fully enveloped by the EDL, we need $\geq$98.5% desalting for the vertical orientation or $\geq$90% desalting for the flat orientation.

4.4 Workarounds for the screening problem in literature

Given the fundamental limitation imposed by salt concentration, sensing methods have often resorted to low ionic strength buffers to offset the loss of sensitivity. Either entire binding-sensing steps were performed at low strength, as was demonstrated by Stern et al. for streptavidin-biotin detection [53]; Or, using

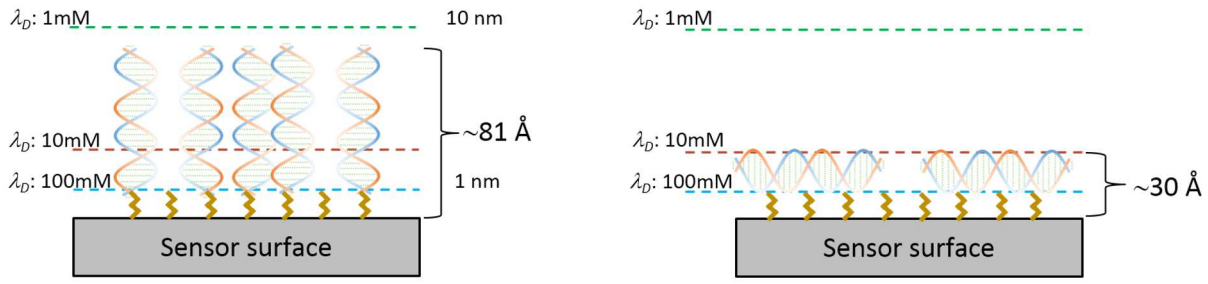

(a) Vertically linked configuration gives higher density

(b) Horizontally linked configuration gives better proximity

Figure 4.3: Schematic of dsDNA molecular orientation on sensor surface, relative to λ_D at various salt conditions.

more complex sample handling protocols for swapping between the diluting and sensing buffers [66], which can be lossy due to decreased viability and low binding efficiency [67, 68]. Microfluidic preconcentration through capture and release scheme has enabled improved detection limits for sensing cancer antigens with nanoribbons from whole blood [69]. Using microstructure arrays functionalized with antibodies, analytes were captured and concentrated on the surface of the microposts in a purification process and subsequently released from the surface into dilute sensing buffers for detection with improved selectivity. From the measurement side, reconfigurable gating methods have opened up possibilities to control ionic conduction in field-effect nanochannel devices [70], but these too work best at low ionic strengths (<1mM). Biolinking strategies also have a contributing effect to the capture efficiency as well as relative proximity and orientation of analytes w.r.t the sensor surface. Even as systematic protocols for proper choice of biolinkers have been developed and reported for sensing with nanowires by Zhang et al. [71] and Dorvel et al. [65, 52], their monolayer thickness (5-10 Å) is comparable with the Debye length and has adverse implications for detecting the target charges. Vapor phase deposited monofunctional silanes provide maximum SAM uniformity and density so that the capture probes may be tethered with the best possible proximity and orientation in a practical setup.

Other novel workarounds have included the engineering of biorecognition layers [72] that bind the analytes closer to the surface. Elnathan et al., used antibody fragments to capture cardiac Troponin T. After enzyme digestion and chemical cleavage, the antibody was fragmented so that the cTnT-Fab complex would bind closer to the sensor and facilitate improved detection (up to 2pM) from physiological samples. Vacic et al. [73], used the salt modulation as a means of studying molecular conformation of the bifunctional CA15.3 cancer marker. Depending on whether the antigen was C/N-terminus bound on the sensor surface, the molecular charge transduction varied and by measuring in different salt buffers, the authors were able to identify through a combination of Debye length and device conduction if the molecule was oriented

horizontally or vertically. In a vastly different approach with CNT sensors, Kulkarni and Zhang [74] used high-frequency AC measurements to study the response of streptavidin-biotin. Rather than directly measure device conduction modulated by the protein, they used ACEO mixing to perturb the molecular dipoles. While this process was modulated by the salt concentration in the 1-100mM range, the intrinsic frequency spectra in each salt solution was very different and the mixing current was non-linear w.r.t gate bias. An independent analysis of the ACEO process may provide further insight into the processes that are coupled with the sensor. While there have been several demonstrations of addressing the screening issues, a reversible scheme for localized desalting and in-situ salt modulation around the field-effect biosensor has remained open for demonstration.

4.5 The role of salt ions on molecular binding and stability

In section 4.3, we discussed the role of salt concentration purely from the standpoint of device sensitivity. We established that the more we deplete the background salts, the better it is for molecular sensing. However, salt ions play a very crucial role in the stability of bimolecules, viz., proteins, DNA, miRNA etc. The kinetics of binding and hybridization efficiency of DNA are directly related to the salt concentration [75] and specific ions such as Mg^{2+} [76]. Schildkraut and Lifson (1965) have famously provided the emprirical equations establishing the logarithmic dependence on Na^{+} concentration of the melting temperature (T_m) of DNA [77]. These models have been improved upon over time and, even until recently, more accurate calculations that factor in free-energy considerations and nearest neighbor relationships have evolved [78, 79, 80]. Online T_m calculators based on these empirical models are also readily available from many sources. Salt ions stabilize the excess negative charge in the helical structure of dsDNA. By drastically decreasing the salt concentration far below physiological conditions, the structure and, consequently, function of the analytes may be seriously compromised [67].

4.5.1 Experimental study of miRNA hybridization and dehybridization with ionic strength

Considering the fact that miRNAs of interest in our study (miR21, let-7a) are short, 22bp long sequences the T_m values of these oligonucleotides are usually quite low (45-50°) in most $\geq$50mM ionic strength buffers. As a result, these molecules can be very adversely affected by direct physical interchange of salt ions. We analyzed the effect on hybridization efficiency as well as dehybridization tendency in low salt through optical measurements of labelled target strands. In these experiments, we also built-in selectivity by comparing

On/Off ratios between matched (complimentary) and mismatched pairs.

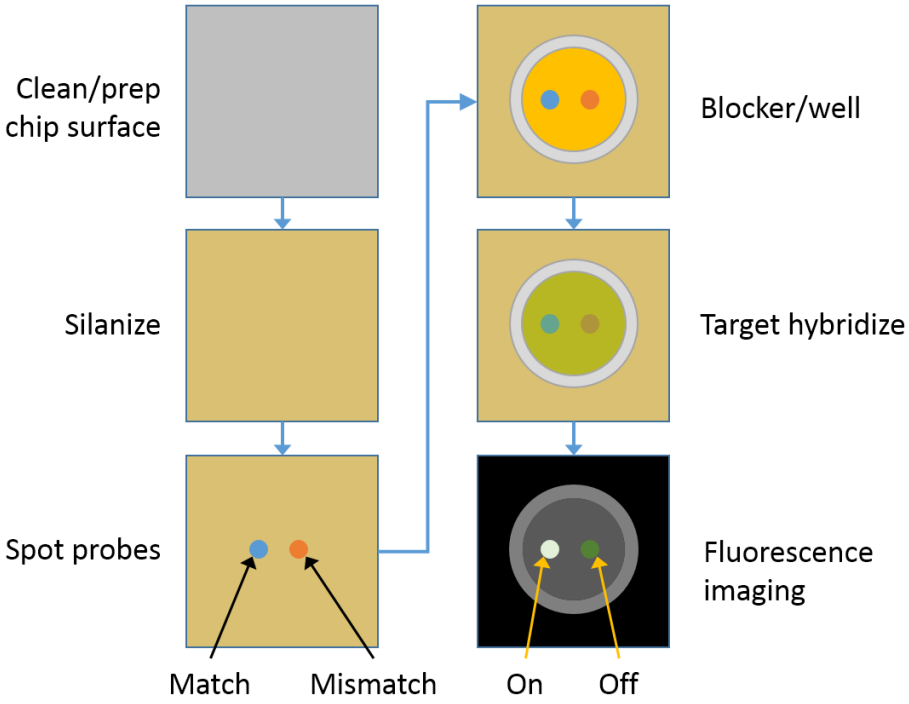

Figure 4.4: Experimental protocol for analyzing salt dependence on miRNA hybridization/dehybridization.

Figure 4.4 outlines the experimental protocol. Match (miR21) and mismatch (let-7a) probe molecules were functionalized on the surface of silicon chips with 100 Å thick HfO_2. The chips were cleaned and treated with an O_2 plasma RIE (Thierry Corp., MI, USA) to activate hydroxyl groups. This was followed by vapor phase silanization [65, 52] with 50 μL of 3-aminopropyldimethylethoxysilane (APDMES) in a septum vial, under mild vacuum, at 85°C for 8-24 hr to achieve a dense monolayer surface with a water contact angle of ca. 45°. Probes were spotted at 50μM in a 25% glycerol/DI water medium using an IM-300 programmable microinjector (Narishige, Japan), allowed to settle for 2 hrs are room temperature under high humidity and baked on a hotplate for 1 hr at 85° for attachment with the silane. Using a PDMS well, a 1X Casein/PBS protein solution was used to block unattached amine groups outside the probe spots for 1 hr. Finally, the target oligos (miR21-TxRed) were introduced at 1μM in the respective salt background (various dilutions of PBS) to hybridize for 90 min. the chips were rinsed in the background buffer and dried before imaging the spots.

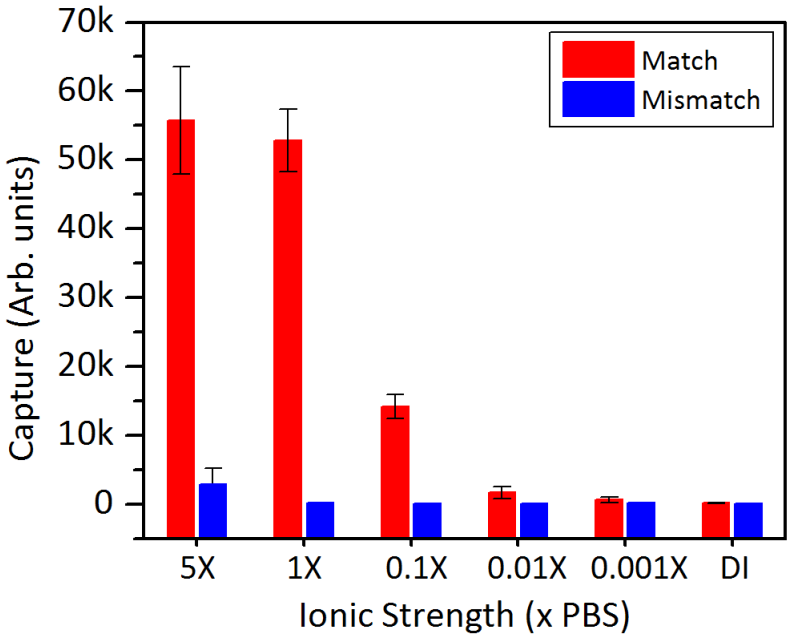

(a) Raw fluorescence data after target hybridization

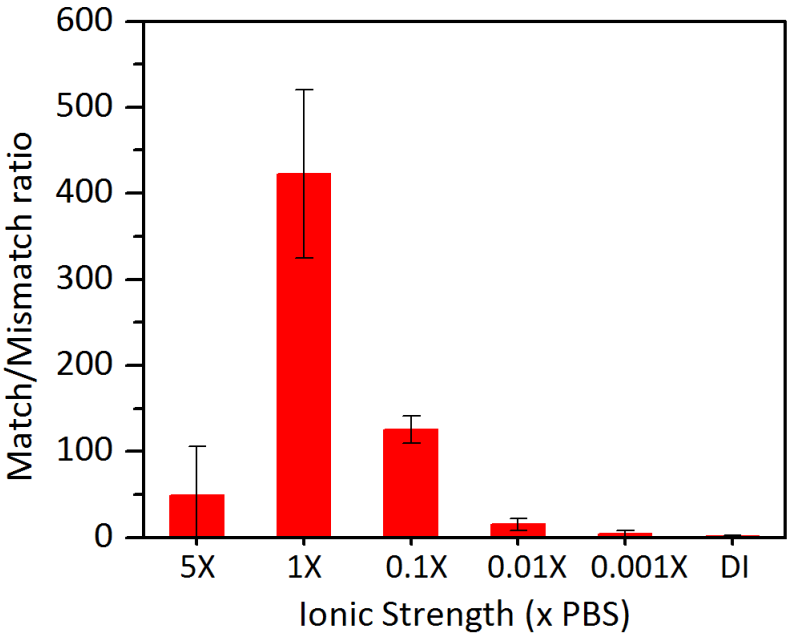

(b) Match to mismatch On/Off ratios

Figure 4.5: Fluorescence data for labelled miRNA target upon hybridizing with surface attached match and mismatch probes in various salt conditions.

4.5.2 Hybridization

Figure 4.5(a) shows the effect of salt concentration on hybridization efficiency. The TxRed intensity directly measures the relative number of target molecules that conjugated with the probes. At $\leq$1mM, the double strand formation cannot be stabilized due to deficiency of salts and we also see very poor match/mismatch selectivity. Thus low salt hybridization that has been often employed to circumvent shielding issues is very suboptimal for analyte capture. The hybridization efficiency is strongly modulated by the ionic strength in the 1mM - 500mM (0.01X - 5X) range. Figure 4.5(b) presents a clearer picture by factoring in selectivity as we calculate On/Off intensity ratios between the matched and mismatched pairs at each concentration. The physiological concentration (1X PBS) emerges as the optimal condition for maximizing the capture of analytes. Even though the miRNAs could hybridize well in the highest salt condition (5X PBS), the blocking process was weaker at that extreme. This is reflected in the decreased On/Off selectivity ratio. A practical experiment in this condition would suffer from specificity issues. Overall, from this experiment, we inferred that the hybridization efficiency at 0.1X PBS and 1X PBS were 9-fold and 30-fold, respectively, greater than the same in low salt at 0.01X PBS. It is therefore imperative that the analyte capture condition be optimized for molecular sensing systems.

4.5.3 Dehybridization

For the dehybridization experiment, the matched miR21 pair with TxRed labelled target were first hybridized as outlined above in 1X PBS (optimal, as established) and the solution was subsequently swapped with respective dilutions of PBS in each case. The dsDNA spots were imaged at intervals of every 5 minutes over a 1 hour period to analyze denaturation through decrease in fluorescent intensity on the surface. Figure 4.6 plots normalized intensity values due to dehybridization. The raw intensity at each time-point was normalized against the value in 1X PBS at that respective time-point in order to factor out photobleaching and other extraneous effects. We observed that the decay curve in 1X and 0.1X PBS practically overlapped each other. By diluting a factor of 10 from 1X to 0.1X PBS, we may still retain the molecules intact on the device surface. This can be useful in decreasing the work of electrostatic desalting. However, at 0.01X PBS and below, the spot intensity showed sharp decay within the initial 10-15 min, followed by a trend of linear decrease. This indicates that even if we hybridize in high salt, swapping solutions to very low salinity could destabilize the analytes and denature them rapidly over the course of the experiment. This adds additional complexity to the sensing process, especially when the settling times are long, and necessitates factoring-in the temporal variations.

From the hybridization and dehybridization v/s salt data of figures 4.5 & 4.6, the following counter-

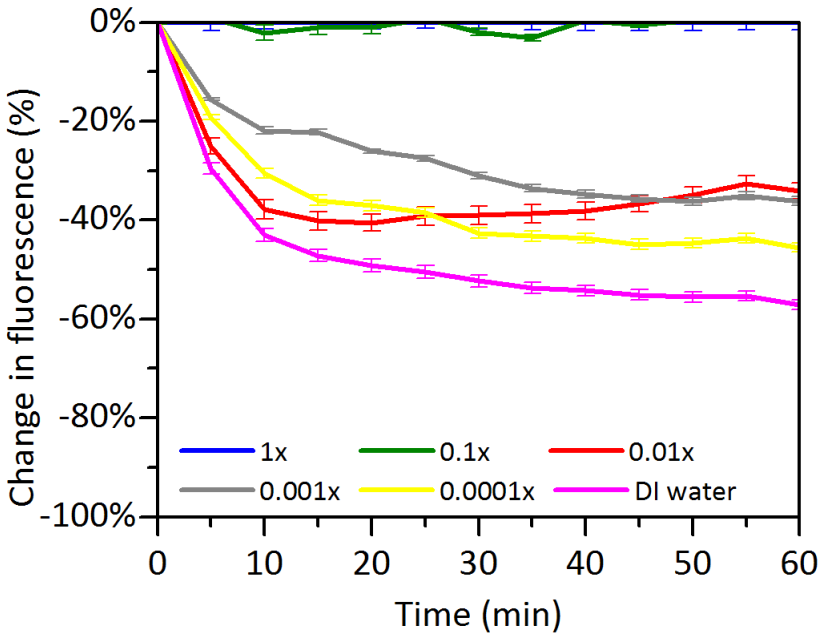

Figure 4.6: Fluorescence data for labelled miRNA target dehybridizing from surface probes across various dilutions of PBS. Data has been normalized to the response from the hybridization buffer (1X PBS).

intuitive result emerges: High salinity is necessary to maximize hybridization efficiency and selectivity. Physical dilution to 0.01X strength causes denaturation. However, we may be able to retain most of the bound analytes by diluting down to 0.1X strength, and then perform on-chip desalting to improve the sensitivity as well. This result, as we discuss in chapters 5 and 6, is an important requirement that ties well with the feasibility and constraints of our desalting approach.

Chapter 5

A scheme for localized electrostatic desalting on-chip

5.1 Concept: manipulating ions with electrostatics

The salt microenvironment around a field-effect biosensor controls the extent of charge transduction from analyte molecules and plays a key role in limiting the device sensitivity. An elegant approach would allow us to locally control the salt concentrations *in-situ*. DC electrostatic fields can be used to perform localized desalting by adsorbing excess ions in the EDL capacitance of charged microelectrodes in solution. This has been demonstrated in supercapacitors [81], large-scale seawater desalination technologies, viz., capacitive deionization (CDI^{TM}) [82, 83, 84, 85] and electrodialysis [86] and studies of blocking electrodes [87]. We have adapted this approach and scaled it down suitably to meet the features of a CMOS electronic platform over which desalting can be implemented[1].

Figure 5.1(a) shows a schematic representation of localized electrostatic desalting with on-chip microelectrodes. In an unbiased droplet, spatial distribution of both positive, p, and negative ions, n, is uniform throughout i.e., $n = p = n_0$, where n_0 is the initial bulk concentration. During desalting, some of these ions move from bulk to accumulate as counter-ions within the EDLs of the respective opposite polarity electrodes. At sufficiently high applied bias and electrode area, this causes substantial decrease in n and p from the rest of the droplet. To minimize side effects such as redox reactions, gas bubbling and heating under strong forcing fields due to overpotentials [89], we can design the desalting scheme to work well below the electrolysis limit of water (1.23 V) in a limited volume. Figure 5.1(b) shows an image of a extended gate field effect transistor (EG-FET) sensor surrounded by micro-patterned electrodes and a microinjected droplet in air within which experiments were performed.

[1]Results discussed in this chapter are published in [88]. Reproduced with permissions from AIP.

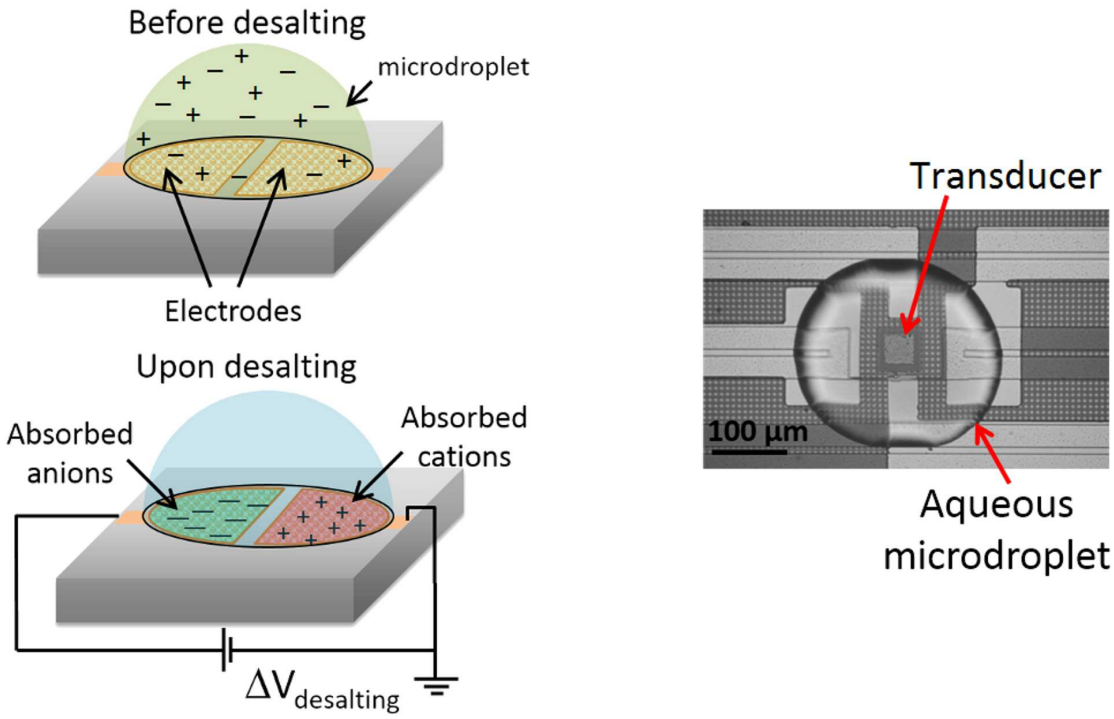

(a) Initially, salt ions are uniformly distributed. By absorbing ions in EDLs during desalting, the bulk can be depleted

(b) Micrograph of electrodes around an EG-FET within a droplet. Device response can be modulated by desalting

Figure 5.1: Schematics and concept of electronic desalting around a transducer in a droplet.[2]

5.2 Theory

5.2.1 Solutions of salt ion profiles based on double layer models

The surface charge density, σ_e of a charged EDL provides a measure of the desalting capacity of our system. In order to determine the desalting capacity at an arbitrary bias, V_e, and initial condition, n_0, we need to solve for the potential distribution, ψ throughout the droplet. Unlike a typical semi-infinite electrode-electrolyte problem, in which the bulk capacity is infinitely greater than local salt ion distributions in the EDLs, the bulk salinity will continuously decrease with EDL charge uptake in our case. As a result, the numerical solution had to be self-consistent such that ψ and σ_e would define an EDL that was equilibrium with the current salt concentration of the droplet, n_i. The Gouy-Chapman model [90, 91, 3] for dilute solutions has been most widely used to study the decay of electric fields and the EDL capacitance. Treating the ions as point charges that follow an equilibrium Boltzmann distribution, ψ varies in accordance with the Poisson-Boltzmann equation

[2]Reproduced with full permission from [88]. Copyright 2015, AIP Publishing LLC.

$$\nabla \cdot (\varepsilon \nabla \psi) = -2zen_0 \sinh\left(\frac{ze\psi_0}{k_B T}\right) \tag{5.1}$$

where ψ_0 is the total voltage drop, with the EDL surface charge density given by

$$\sigma_e = -sgn(\psi_0) 4zen_0 \lambda_D \sinh\left(\frac{ze\psi_0}{2k_B T}\right) \tag{5.2}$$

In reality, σ_e and ψ follow a highly non-linear relationship and the well-known exponential distribution of equations 5.1 and 5.2 from dilute solution theory breaks down. Kilic et al. [92] have extensively analyzed this problem and provided a useful analytical framework for solving the EDL of high salt/high bias systems. Steric effects due to finite ion sizes at high ionic strength and large applied voltages are incorporated through Modified Poisson-Boltzmann (MPB) models [93, 94], in which ψ decays as follows:

$$\nabla \cdot (\varepsilon \nabla \psi) = -zen_i \frac{2\sinh\left(\frac{ze\psi}{k_B T}\right)}{1 + 2\nu \sinh^2\left(\frac{ze\psi}{2k_B T}\right)} \tag{5.3}$$

and surface charge density, σ_e in the EDL is given by

$$\sigma_e = -sgn(\psi_0) 2zen_0 \lambda_D \sqrt{\frac{2}{\nu} \log\left[1 + 2\nu \sinh^2\left(\frac{ze\psi_0}{2k_B T}\right)\right]} \tag{5.4}$$

The packing fraction, $\nu = 2n_i a^3$, accounts for finite size of ions, a in equation 5.3, so that ion density does not exceed the physical limit of $1/a^3$. For simplicity, we consider only the salt ions and neglect the contribution of H^+ and OH^- ions. Equation 5.3 is highly nonlinear and no general solution exists in a complex geometrical system such as a droplet placed on rectangular electrodes. We therefore resort to a numerical solution that provides considerable insight into the desalting properties of the system.

5.2.2 A composite double layer model for estimating the EDL charge uptake from highly saline media

The potential profile within a droplet can be estimated analytically based on the Modified Poisson-Boltzmann model (equation 5.3) of the EDL. At high salt concentrations, the diffuse EDL assumption cannot accom-

modate enough ions to balance the electrostatic field. Ionic charge, thus, begins to condense into a more concentrated EDL than predicted using the Boltzmann distribution. Kilic et al.'s 1-D composite diffuse layer (CDL) model closely approximates the MPB solution but breaks down the EDL into components that have known analytical solutions: an inner compact layer of thickness, l_c, adjacent to the Stern layer in which excess ions condense with density $1/a^3$, and an outer diffuse layer identical with that of the Gouy-Chapman EDL theory. The compact layer accommodates the steric effects that arise out of ion crowding at high salt or large voltage bias. Consider a droplet placed on two opposite polarity electrodes, as shown in figure 5.2.

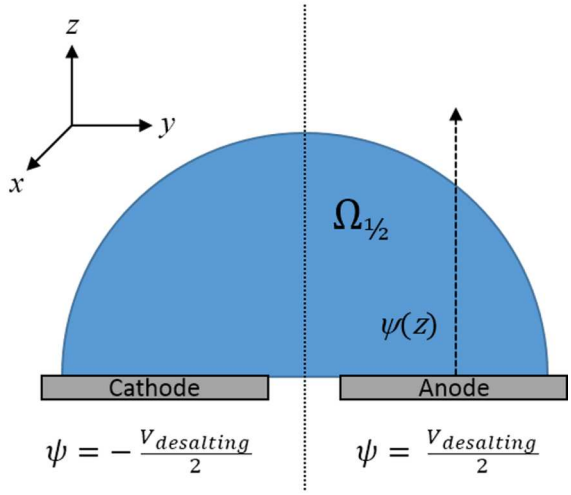

Figure 5.2: Numerical solution domain showing a droplet placed on desalting electrodes.[3]

Based on ionic charge conservation:

$$\int_{\Omega} n_0 \mathrm{d}V = \int_{\Omega_{1/2}} \left(n\left(\vec{r}\right) + p\left(\vec{r}\right)\right) \mathrm{d}V \tag{5.5}$$

where $n\left(\vec{r}\right)$ and $p\left(\vec{r}\right)$ represent the negative and positive ion distributions, respectively, and $\Omega_{1/2}$ denotes the region with half the droplet volume.

$$n_0 V_\Omega = \int_{\Omega_{1/2}} \left(n\left(\vec{r}\right) + p\left(\vec{r}\right) - 2n_i\right) \mathrm{d}V + \int_{\Omega_{1/2}} 2n_i \mathrm{d}V \tag{5.6}$$

Applying the CDL approximation, equation 5.6 yields

[3]Reproduced with full permission from [88]. Copyright 2015, AIP Publishing LLC.

$$n_0 V_\Omega \approx \frac{l_c A_e}{a^3} + \int\limits_{\Omega_{1/2}} 2n_i \left(\cosh\left(\frac{e\psi}{k_B T} \right) - 1 \right) \mathrm{d}V + \int\limits_{\Omega_{1/2}} 2n_i \mathrm{d}V \tag{5.7}$$

We assume a thin double-layer (valid because $\lambda_D \ll \vec{r}$), and neglect the fringe effects along the edges, so that the volumetric potential profile simplifies to a 1-D potential distribution:

$$\psi(x, y, z) \approx \psi(z) \tag{5.8}$$

Within the diffuse Boltzmann layer of the CDL, $\psi(z)$ is given by the classical Gouy-Chapman solution:

$$\psi(z) = \frac{4k_B T}{e} \mathrm{arc\,tanh}\left(\tanh\left(\frac{e\psi_0}{4k_B T} \right) \exp\left(-\frac{z}{\lambda_i} \right) \right) \tag{5.9}$$

where, λ_i is the modified Debye length based on the applied desalting bias at the electrode. The critical voltage, V_c, above which we observe the onset of double layer compaction and CDL formation is given by

$$V_c = \frac{k_B T}{e} \log\left(\frac{1}{n_i a^3} \right) \tag{5.10}$$

In general, the potential drop across the diffuse Boltzmann layer, $V_b = \min(V_e, V_c)$. Below the critical voltage, all EDL charge resides within the Boltzmann layer and, hence, $l_c \longrightarrow 0$. The accumulated charge density in the Boltzmann layer increases as $\exp\left(\frac{eV_e}{2k_B T} \right)$. Subject to this condition, equation 5.7 yields the following solution:

$$n_0 V_\Omega = \frac{l_c A_e}{a^3} + 8 n_i \lambda_i A_e \sinh^2\left(\frac{eV_b}{4k_B T} \right) + n_i V_\Omega \tag{5.11}$$

where, $V_b = V_c = \frac{k_B T}{e} \log\left(\frac{1}{n_i a^3} \right)$ for $V_e > V_c$ and $V_b = V_e$ for $V_e \leq V_c$.

Thus, the compact layer thickness is given by

$$l_c = \lambda_0 \sqrt{2\nu_0} \left(-1 + \frac{f\nu_0}{2} + \sqrt{\left(1 - \frac{f\nu_0}{2} \right)^2 + \left(\left| \frac{eV_e}{k_B T} \right| - \log\left(\frac{2}{f\nu_0} \right) \right)} \right) \tag{5.12}$$

for V_e>V_c and $l_c = 0$ for $V_e \leq V_c$, with $\nu_0 = 2n_0a^3$ and $f = \dfrac{n_i}{n_0}$. n_i can be solved using equation 5.11 for any ionic concentration, n_0, and applied bias, V_e for a given electrode area and droplet volume. Further, at very large bias, $\left|\dfrac{eV_e}{k_BT}\right| \gg 1$, so the compact layer thickness simplifies to $l_c \approx 2\lambda_0\sqrt{n_0a^3\left|\dfrac{eV_e}{k_BT}\right|}$. Hence, the maximum droplet volume that can be depleted to a fraction, f, with a given electrode area is

$$V_{\Omega,max} = A_e\left(\frac{8\sqrt{f}}{1-f}\lambda_0\sinh^2\left(\frac{eV_b}{4k_BT}\right) + \frac{l_c}{n_0a^3\left(1-f\right)}\right) \tag{5.13}$$

The total EDL surface charge absorbed on the electrodes during the desalting process is given by

$$Q_e = A_e\sigma_e = \mp\int\limits_{\Omega_{1/2}} e\left(n-p\right)\mathrm{d}V \tag{5.14}$$

where, the $-$ and $+$ signs correspond to the positive and negative electrode polarity, respectively.

$$Q_e \approx \mp A_e\frac{el_c}{a^3} \mp \int\limits_{\Omega_{1/2}} 2A_en_i\sinh\left(\frac{e\psi}{k_BT}\right)\mathrm{d}x \tag{5.15}$$

Using equation 5.9 with the thin double layer assumption, we get

$$Q_e = A_e\sigma_e \approx \mp A_e\frac{el_c}{a^3} \mp 4en_i\lambda_i\sinh\left(\frac{eV_b}{2k_BT}\right) \tag{5.16}$$

This gives

$$\sigma_e = \mp\frac{el_c}{a^3} \mp 4en_0\lambda_0\sqrt{f}\sinh\left(\frac{eV_b}{2k_BT}\right) \tag{5.17}$$

5.2.3 Numerical solutions of salt profiles and concentrations

In order to numerically simulate the ionic distribution profiles in microdroplets ($\sim$ 300pL) over 6100 μm^2 electrodes, we implemented the CDL framework to solve equation 5.1. The simulations were subject to ion conservation (equation 5.5) and steric constraints of maximum density to prevent artificial overcrowding that arises with the point-charge aprroach of the GC model. For $p \leq 1/a^3$ and $n \leq 1/a^3$

$$p = n_i \exp\left(-\frac{e\psi}{k_B T}\right) \quad , \quad n = n_i \exp\left(\frac{e\psi}{k_B T}\right) \tag{5.18}$$

However, when the steric limit was approached (equation 5.10)

$$p = \frac{1}{a^3} \ , \ \ n = 0 \quad | \quad p > 1/a^3 \tag{5.19a}$$

$$n = \frac{1}{a^3} \ , \ \ p = 0 \quad | \quad n > 1/a^3 \tag{5.19b}$$

The Dirichlet boundary conditions ($\psi = \pm 0.5 V_{Desalting}$) were used on the electrodes and Neumann boundary conditions $\vec{\nabla}\psi \cdot \hat{n} = 0$ on the outer boundaries of the droplet. By updating the bulk concentration to n_i instead of n_0, the numerical scheme would converge self-consistently.

The numerically determined ionic concentration profiles in a 300 pL droplet, under various conditions, are plotted in figure 5.3. At an applied desalting bias of 1 V, comparisons between 1μM and 10μM salt concentrations are reflected in the negative ion density profiles of figures 5.3(a) and 5.3(b). At the lower concentration, enough ions are forced to pile up near the electrodes and, consequently, deplete the droplets to less than 1% of the original ionic concentration. For the same electrode area, the desalting effect (measured by decrease in the bulk concentration of the droplet n_i over the initial concentration n_0) decreases with increasing background concentration. Further, in figures 5.3(c-f), we compare between the negative and positive ion distributions for both the ionic concentrations at low (0.4 V) desalting bias, respectively. As expected from the symmetry for a 1:1 electrolyte with identical electrodes, the solutions are identical and mirror each other. While the low applied bias is insufficient to achieve any desalting in the 10μM droplet, increasing the applied bias to 1 V could enable more substantial salt depletion (figures 5.3(g & h)) as we approached closer to more realistic environments (1mM).

Ionic charge absorbed as a function of desalting bias, is plotted for various ionic concentrations in figure 5.4(a). In low ionic strength droplets, the charge absorbed saturates with voltage due to the limited number of total available ions in the droplet. This is a consequence of the self-consistent solution within a species-limited system. At higher concentrations, steric effects dominate and are responsible for diminished capacity. Figure 5.4(b) shows the variation of bulk ionic concentration, n_i, in the droplet as a function of initial salt concentration, n_0. As we see the concentration curves shift leftward, it follows that the desalting efficiency of the system increases as we raise the applied bias from 0 to 1.0 V. For small ionic concentrations,

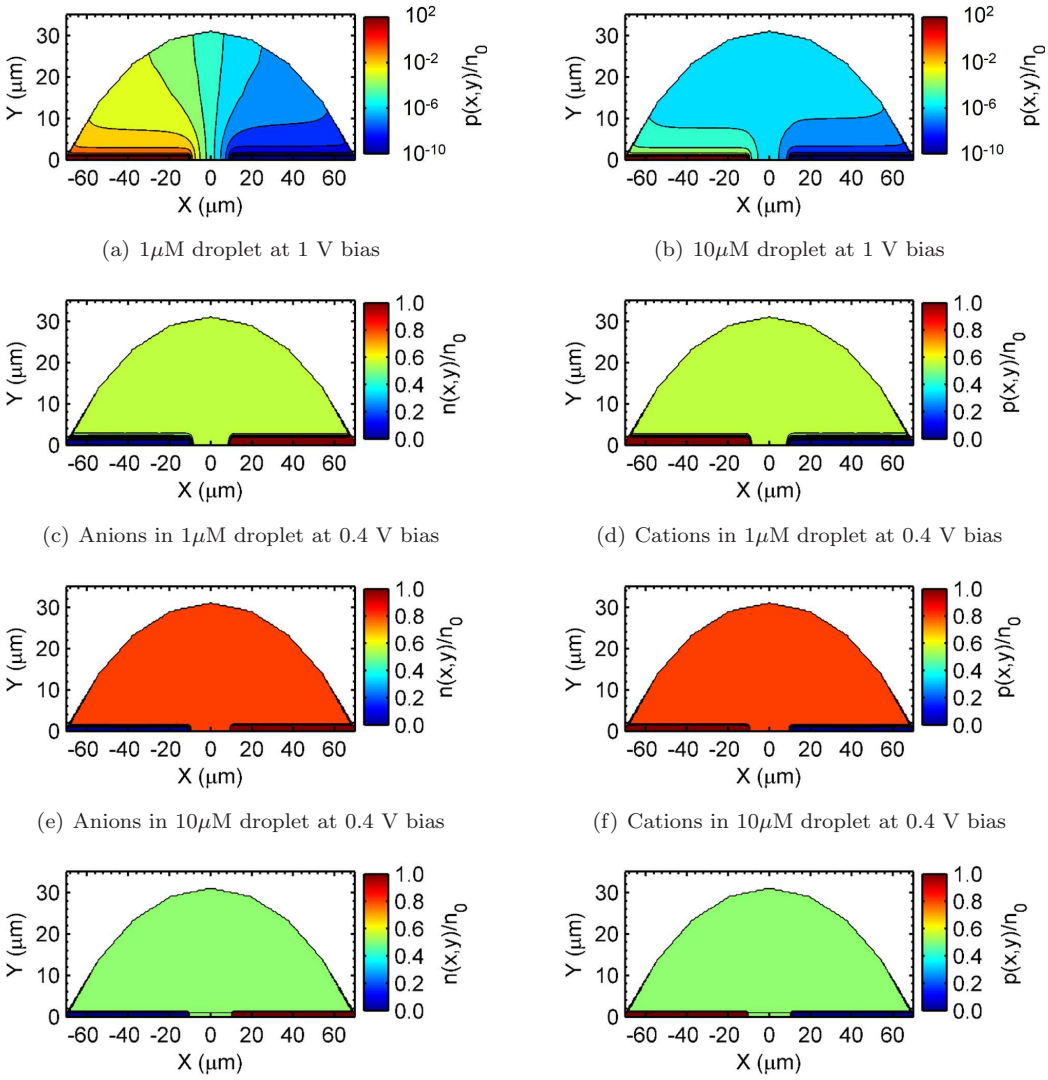

(a) 1μM droplet at 1 V bias

(b) 10μM droplet at 1 V bias

(c) Anions in 1μM droplet at 0.4 V bias

(d) Cations in 1μM droplet at 0.4 V bias

(e) Anions in 10μM droplet at 0.4 V bias

(f) Cations in 10μM droplet at 0.4 V bias

(g) Anions in 1mM droplet at 1 V bias

(h) Cations in 1mM droplet at 1 V bias

Figure 5.3: Numerical simulation of ion profiles in 300 pL droplets by desalting with 6100 μm^2 electrodes.[4]

the critical voltage (V_c) for ion compaction is large, hence, the droplet is considerably desalted. For large ionic concentrations ($\geq$10mM), however, we see that the desalting efficiency is drastically reduced due to the limited absorption capacity of electrodes for EDL charge uptake. At these conditions, V_c is very small and charge accumulation is forced to occur within the compact layer while desalting bias is applied on the droplet. Since, the thickness of this compact layer is weakly dependent on the applied bias as $\sqrt{V_e}$, this leads to substantially lower desalting at high salt concentrations ($\sim$100mM).

[4]Reproduced with full permission from [88]. Copyright 2015, AIP Publishing LLC.

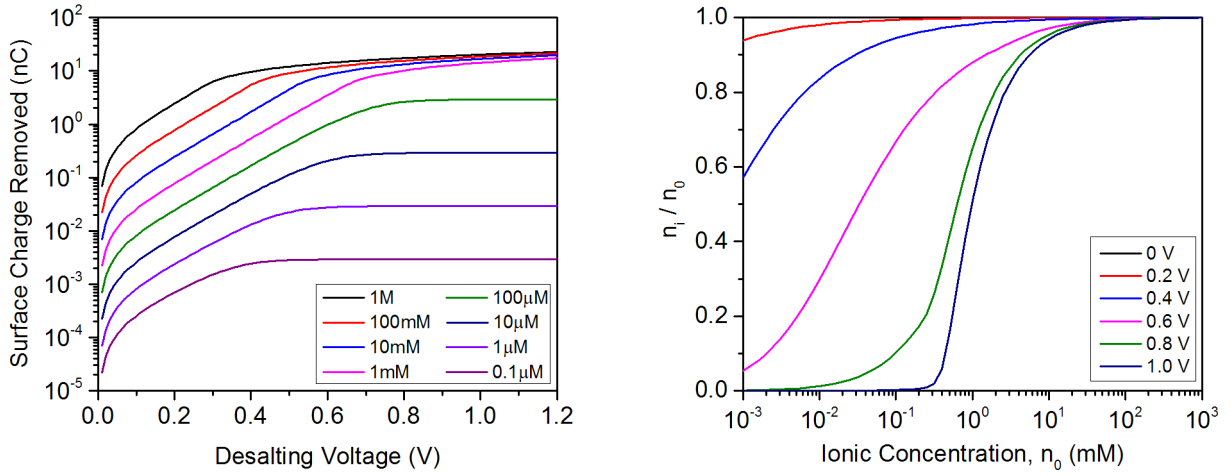

(a) A self-consistent calculation of surface charge absorbed in the EDL v/s applied bias during the desalting process

(b) Achievevable final/initial salt concentrations ($^{n_i}/_{n_0}$) in a microdroplet v/s desalting bias for various ionic strengths

Figure 5.4: Numerical simulations of EDL absorption and bulk ionic concentration during desalting.

5.2.4 Comparisons between EDL theories

A numerical comparison of the EDL solutions between all three models highlights the key limitations of the Gouy-Chapman model and the need for more accruate modifications that account for the size and crowding of ions. The exponential relationships for $\psi(z)$ and σ_e (equations 5.1 and 5.2) have been very widely applied to get a better understanding of many nanofluidic systems, including field-effect sensors. However, as most realistic situations lie far outside the tightly bound constraints of low salt (O(μM))) or very low bias (<100 mV), quantitatively, inaccuracies are bound to affect the results. Figure 5.5 shows direct comparisons of the three models, viz. GC point-charge theory (dash-dot), the MPB analytical (dashed) and the self-consistent CDL scheme (solid lines). The ionic charge per unit area absorbed as a function of desalting bias has been plotted for three representative ionic concentrations that span the very low and very high salt solutions, including the transitional point of 1mM salinity.

In all three models, the desalting efficiency of the system increases as expected with applied bias from 0 to 1.0 V. In low salt (10μM), the exponential approximation of the GC model for σ_e is valid and agrees closely with the MPB model. The self-consistent solution differs from both semi-infinite model solutions because it is also constrained by limited availability of ions within the droplet. However, the MPB solution (equation 5.4) substantially deviates in high salt conditions ($\geq$1mM). At these conditions, the steric effects of ion crowding become dominant (as discussed in the self-consistent solution of figure 5.4(a) as well) and the effect of large applied bias cannot be ignored. The GC model over-predicts EDL charge absorption, and hence the desalting capacity, by nearly three orders of magnitude over the MPB solution. Furthermore, when

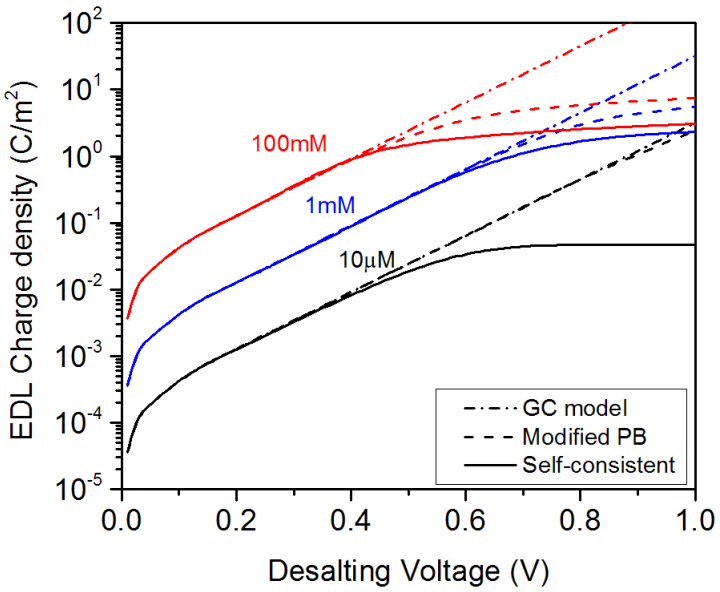

Figure 5.5: Prediction of EDL specific charge absorption v/s desalting bias: a comparison between various models.[5]

we take into account the finite volume of the droplet, the self-consistent solutions flatten out even more than the MPB prediction and indicates that desalting capacity is significantly reduced. Ironically, the shifting of the background equilibrium concentration due to desalting adds additional burden on the desalting process. Therefore, idealizations based on the dilute solution theory with a semi-infinite EDL cannot sufficiently constrain the electrode-electrolyte interface.

5.2.5 Scaling considerations for desalting from high salt conditions

To further relate the degree of desalting to applied bias and salt concentration, we determine the maximum droplet volume V_{max} that can be desalted to a fraction f of the original salt concentration n_0. This expression is captured by equation 5.13 for a given available surface area, A_e of the desalting electrodes. Using the ratio of V_{max}/A_e as a metric, it is possible to gauge the scaling requirements of the dimensions of the desalting construct. Figure 5.6 plots the droplet volume to electrode area (V/SA) ratio that is required for desalting the droplet of various salt concentrations to a fraction $f = 0.5$. For desalting from small ionic concentrations ($\leq$1mM), the V/SA ratio can be considerably large (>100 μm). However, in order to deplete salts from large ionic concentrations ($\geq$100mM) below the reduction potential, this ratio must be considerably small (<1 μm). This places a steep cost on the surface area of the desalting electrode that needs to be packed inside a very tiny droplet. For example, with 100 μm $\times$ 100 μm electrodes, the theoretical prediction suggests that

[5]Reproduced with full permission from [88]. Copyright 2015, AIP Publishing LLC.

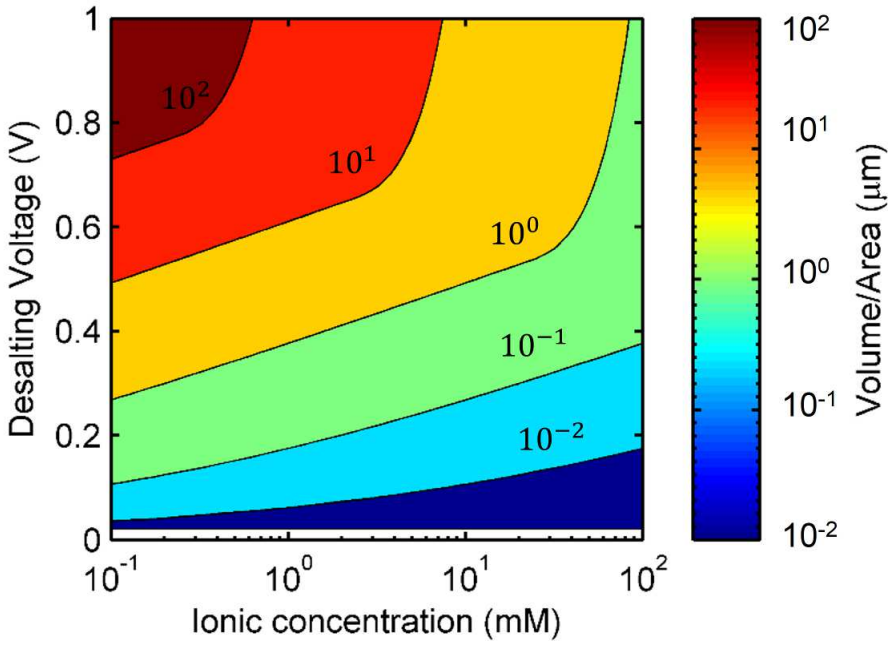

Figure 5.6: Scaling of desalting capacity with electrode area. A plot of droplet volume-over-electrode area ratio required in order to deplete salts by 50% across ionic strengths and applied bias.[6]

sub-nL droplets should be deposited for effective desalting at these conditions.

5.3 Imaging the ion redistribution during desalting

The desalting effect was experimentally tested in microdroplets (1000 pL volume) through optical measurements with the pH sensitive SNARF-5F dye. SNARF-5F is known to fluoresce well within the 5-8 pH range so that, under neutral initial pH conditions, the dye intensity would locally vary in accordance with the $[H^+]$ or $[OH^-]$ ion distribution that followed during desalting. The calibration curves (figure 5.7) show response of SNARF-5F over the 0.01-100mM ionic strength range with good dynamic range for pH 5-8. Applying pH equalization control suppressed the activity of the dye.

5.3.1 Surface dye attachment

The HfO_2 chip surfaces were functionalized with a monolayer of the SNARF-5F dye molecule using the covalent NHS-amine attachment chemistry. Prior to functionalization, the chips were cleaned and surface activated in a diener oxygen plasma RIE (Thierry Corp., MI, USA); following this step, they were silanized

[6]Reproduced with full permission from [88]. Copyright 2015, AIP Publishing LLC.

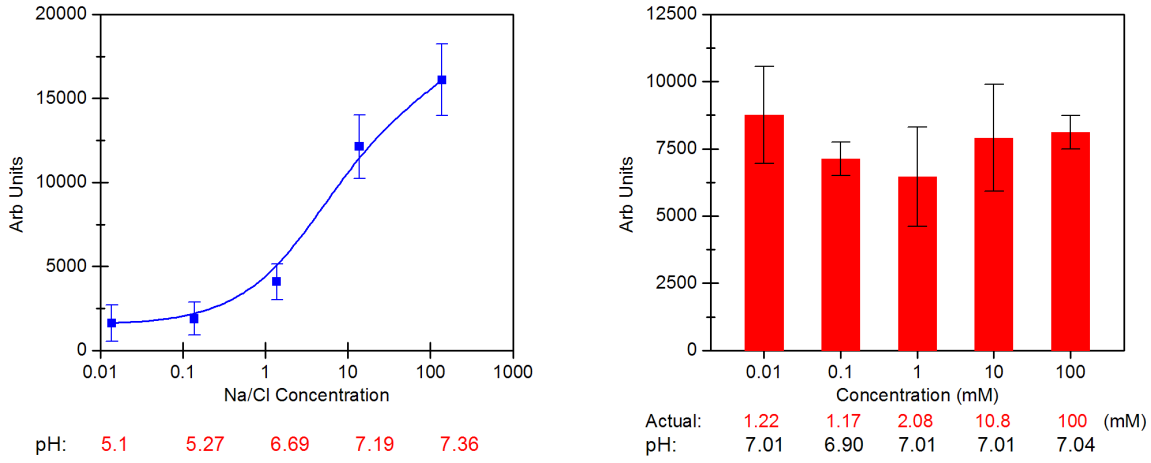

(a) Without pH equalization

(b) With pH equalization to ~7.00

Figure 5.7: Fluorescence calibration plots showing response of SNARF-5F dye functionalized on a HfO_2 device surface at various ionic strengths, without and with pH equalization.[7]

for 8-24 hrs with APDMES in the vapor phase at 85°C. Next, using a well-known activation chemistry [95], the SNARF-5F dye was modified at room temperature with ethyl(dimethylaminopropyl)carbodiimide (EDC) leaving group and N-hydroxysulfosuccinimide (sulfo-NHS) to form a water soluble intermediate that, subsequently, reacted with the surface amine in 0.5X PBS buffer at pH of 6 for 2 hr. After reaction completion, the chips were rinsed in DI water, dried and stored in a dark vacuum dessicator until experiments. Dye imaging during desalting experiments was performed on a Nikon Eclipse FN-1 Fluorescent Microscope with high NA objectives and 540-580/600-660nm Y-2-E/C filterblock (Nikon, Japan).

5.3.2 Analysis of dye profiles on devices within microdroplets

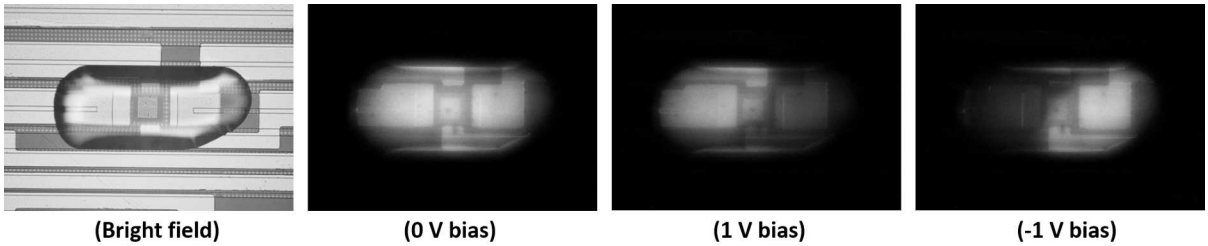

Figure 5.8: Fluorescent images of the dye profile over the device during desalting process, showing forward and reverse bias and negative controls.[8]

Each experiment was performed over a duration of ca. 30 seconds, and repeated for 3 different devices in droplets. Figure 5.8 shows a device within a microdroplet and its fluorescent response at 1V desalting

[7,8]Reproduced with full permission from [88]. Copyright 2015, AIP Publishing LLC.

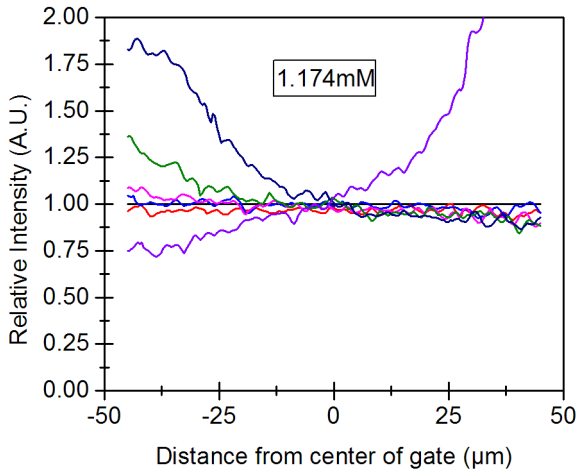

(a) Dye intensity v/s desalting bias and reverse control in 1.174mM salts

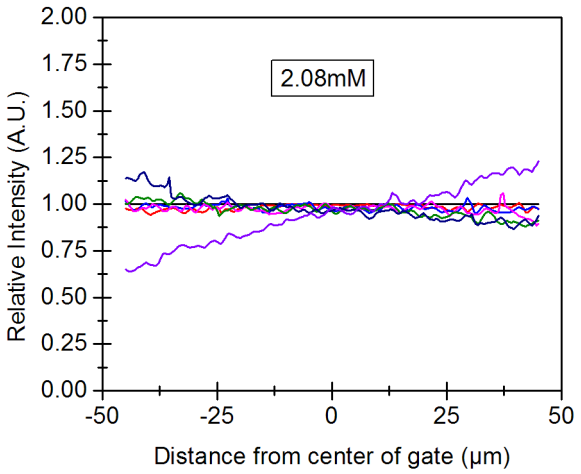

(b) Dye intensity v/s desalting bias and reverse control in 2.08mM salts

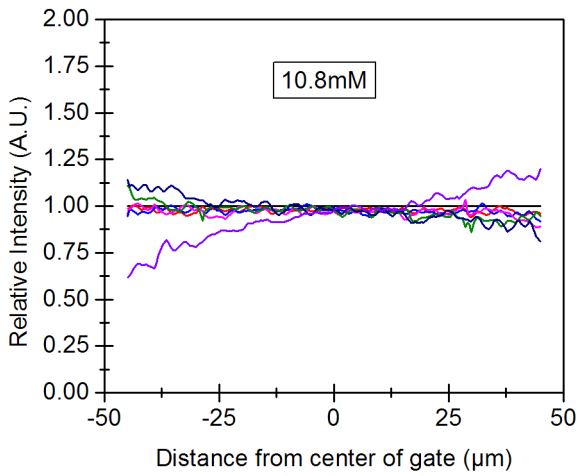

(c) Dye intensity v/s desalting bias and reverse control in 10.8mM salts

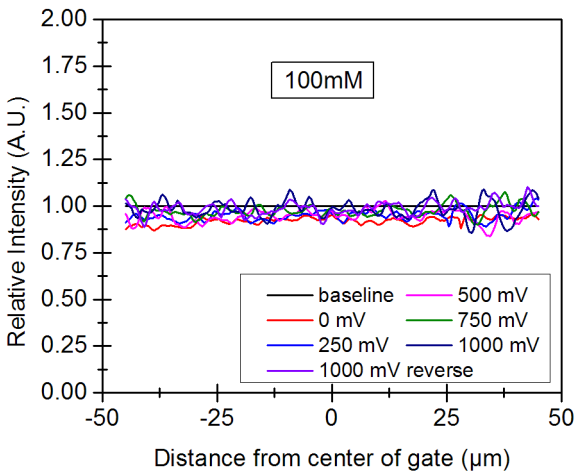

(d) Dye intensity v/s desalting bias and reverse control in 100mM salts

Figure 5.9: Analysis of desalting in a microdroplet using a pH sensitive dye (SNARF-5F), in a 4-electrode desalting configuration. The device main diagonal in the normalized gray value analysis (b-e) spans from -28 μm to +28 μm.[9]

after 30 seconds, with both forward and reverse bias control. In order to quantify, the fluorescent intensity was analyzed using mean gray value profile along the line of symmetry through either half of the blocking cell established with the desalting electrodes. The placement and configurations of desalting electrodes play a crucial role in redistributing salts around the device. Both 2-electrode (figure 5.10(c-d)) as well as 4-electrode (figures 5.9(a-d) & 5.10(c-d)) configurations were tested, in 1-100mM ionic strength solutions. In the 2-electrode configuration, only the East-West electrode pair were biased, while the North-South pair were left to float. In the 4-electrode configuration both pairs were biased such that the North/West and

[9]Reproduced with full permission from [88]. Copyright 2015, AIP Publishing LLC.

South/East were at $V_{Desalting1}$ and $V_{Desalting2}$ respectively.

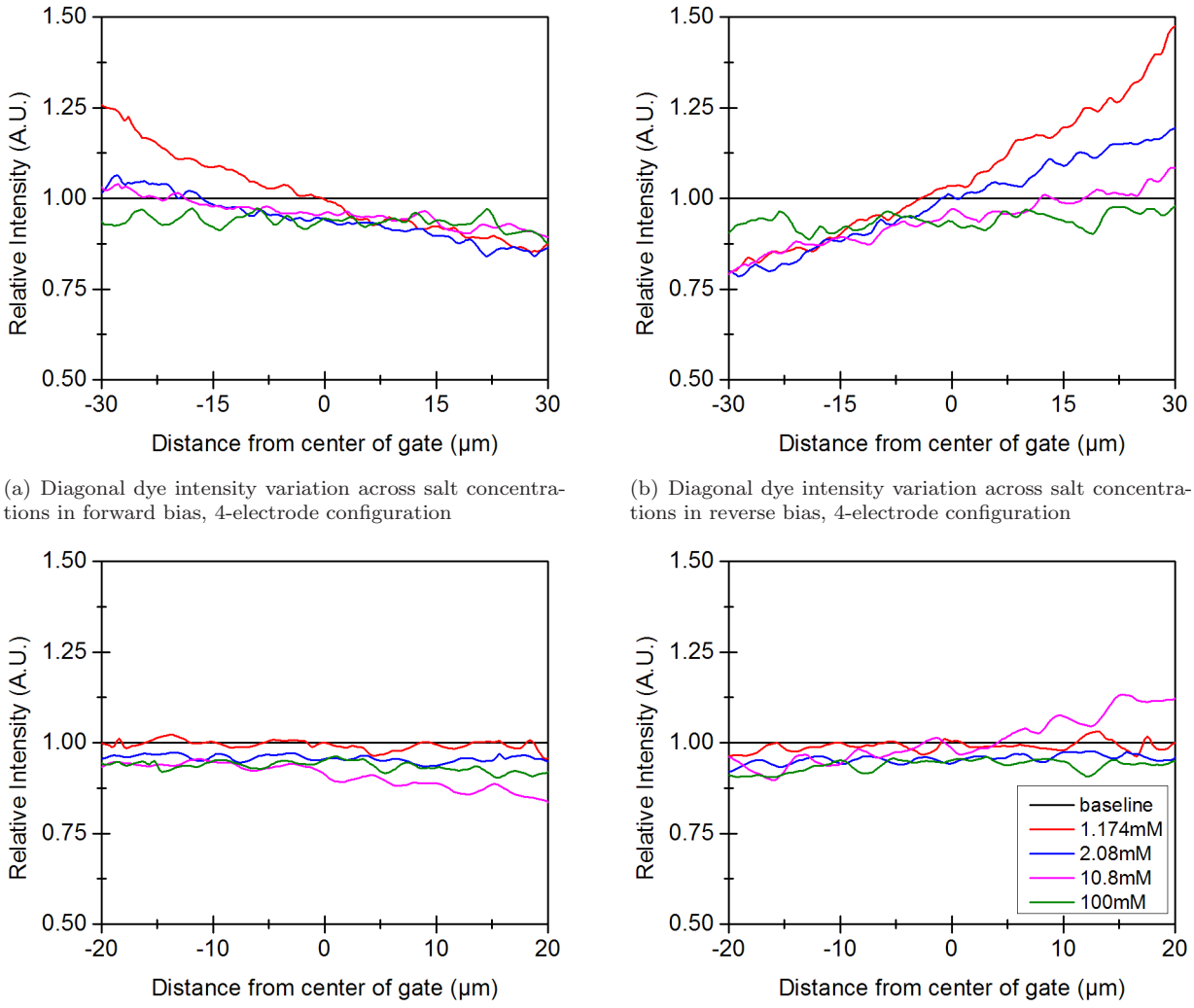

(a) Diagonal dye intensity variation across salt concentrations in forward bias, 4-electrode configuration

(b) Diagonal dye intensity variation across salt concentrations in reverse bias, 4-electrode configuration

(c) Diagonal dye intensity variation across salt concentrations in forward bias, 2-electrode configuration

(d) Diagonal dye intensity variation across salt concentrations in reverse bias, 2-electrode configuration

Figure 5.10: Normalized fluorescence intensity of SNARF-5F dye response to ±1 V desalting, showing mean variations with ionic strength. The device main diagonal spans from -28 μm to +28 μm.[10]

Measured relative changes in the fluorescent response of the dye to the desalting conditions were analyzed over the sensor region. While this region fell within the bulk of the droplet, a net change in the fluorescence over the gate would reflect on the depletion over the region of interest. We expected dye partitioning about the vertical (2-electrode) or left diagonal (4-electrode) planes. Therefore, for quantifying the fluorescent intensity, the region of interest was the left-diagonal (4-electrode) or the horizontal width (2-electrode) overlapping with the EG-FET pad inside the droplet. In both cases, dye response was consistent with

[10]Reproduced with full permission from [88]. Copyright 2015, AIP Publishing LLC.

the applied desalting bias and the partitioning effect became optically prominent at 0.75 V and 1 V, with the -1 V case showing reversal symmetry as expected. As visualized from the transverse profile across the plane of symmetry (figure 5.9(a-d)), on-chip desalting was effective up to the 10.8mM ionic strength, with no statistically significant change at 100mM. Between the two biasing configurations, using the 4-electrode scheme, by virtue of additional surface area to absorb ions into the EDL, showed increased desalting activity over the 2-electrode configuration (figure 5.10(c-d)). In these experiments, we expected to observe a binary intensity profile between the bulk and electrode surface upon desalting. However, the fact that there was partitioning with a continuously varying profile meant that the flat electrodes only had limited desalting capacity. There were still excess ions remaining in the bulk of the microdroplet as indicated by dye intensity.

5.3.3 Control experiments

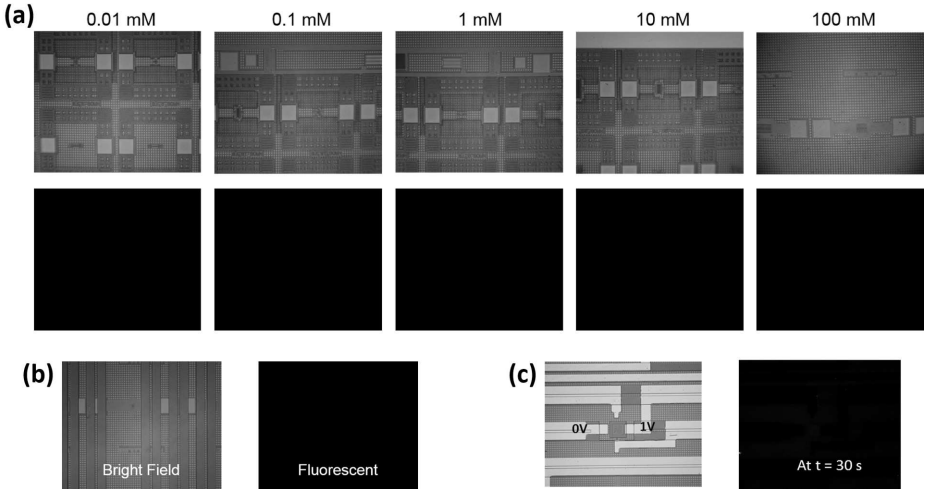

Figure 5.11: Negative control experiments showing device response in wet (a), (b) dry condition and (c) dry device with 1 V applied bias in the absence of SNARF-5F dye.[11]

Figure 5.11 shows fluorescent response across the electrolytes in negative control experiments. The conditions tested were (a) chip regions that were devoid of the surface dye and dye fluorescence under dry conditions when no ions were present, both without (b) and with desalting bias applied (c). In order to contrast with the droplet experiments, the dye response during 4-electrode desalting experiments in a bulk well (figure 5.12) did not show partitioning and salt depletion over the device. This was indicative of the overwhelming background excess of salt ions that remained even after capacitive adsorption over the electrodes during desalting. Desalting in a DI water droplet (figure 5.13) returned minimal response at ± 1 V

[11]Reproduced with full permission from [88]. Copyright 2015, AIP Publishing LLC.

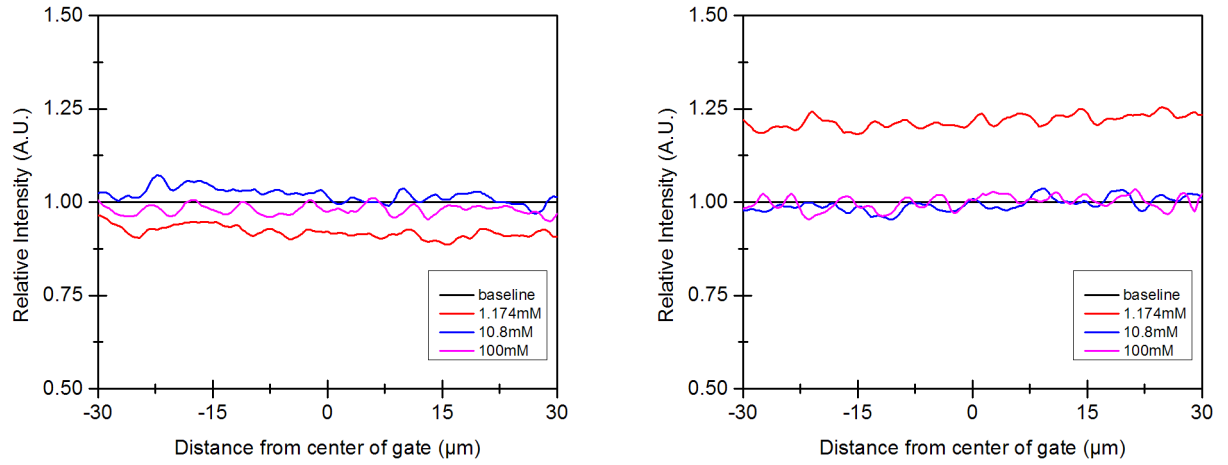

(a) +1 V forward desalting bias

(b) -1 V reverse desalting bias

Figure 5.12: Normalized fluorescence intensity of SNARF-5F dye response over the device region to desalting in a bulk well (150 μL), at different ionic strengths.[12]

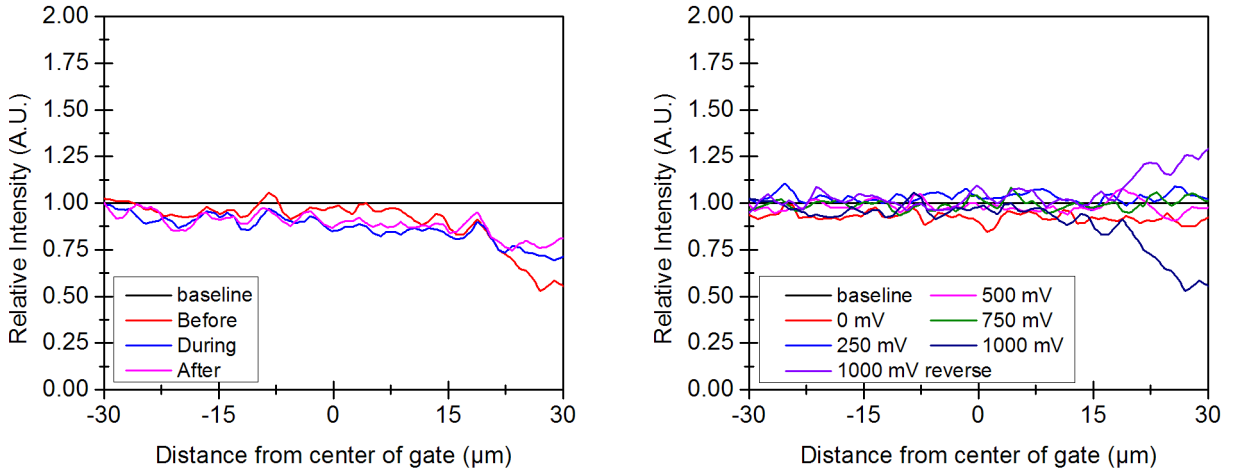

(a) Before, during and after applying 1 V desalting bias

(b) Variation with 0 to 1 V desalting bias

Figure 5.13: Normalized fluorescence intensity of SNARF-5F dye response over the device region to desalting in a DI water droplet.[13]

due to the already depleted state of the trace ionic charges.

[12,13]Reproduced with full permission from [88]. Copyright 2015, AIP Publishing LLC.

5.4 Summary

Theoretical models that describe the evolution of EDLs give us considerable insight to the requirements and constraints of electrostatic desalting. The CDL approximation of Kilic et al., provides a useful framework with which analytical predictions of the EDL charge absorption can be made in droplets with a finite number of ions. This establishes the scaling relationship (V/SA) that serves as an indicator of the feasibility of desalting at any given ionic strength. Experimental analysis by optical tracking of pH sensitive SNARF-5F also confirms the expected behavior of on-chip electrodes under non-Faradaic desalting potentials. However, in order to achieve substantial desalting from physiologically relevant concentrations, both calculations and experiments indicate that it is necessary to dramatically enhance the quantity of EDL absorption. In part, this can be solved by a superhydrophilic electrode surface [96] over which droplets settle into shallow configurations. However, for larger, more addressable droplet volumes ($\geq$100 pL) near the 100mM concentration, high surface area electrodes that can be defined in a CMOS-compatible manufacturing process are needed.

Chapter 6

On-chip electrodes for the FET-in-droplet platform

In the previous chapter, we reviewed the conceptual background and described various theories to analyze the EDL phenomena that facilitate the desalting process. On the basis of scaling considerations in section 5.2.5, we established that high surface area electrodes and sub-nL droplets were necessary to meet the V/SA ~ 1 μm requirement for significant desalting of 1-100mM electrolytes. Establishing a solution potential within such a tiny droplet would be practically impossible through a conventional (rather bulky) reference electrode, even using a Luggin-Haber capillary. It will be beneficial to localize the reactions for maximum efficacy and sensitivity using on-chip electrodes. In this chapter, we demonstrate a biasing scheme through which we are capable of desalting $\leq$10mM concentration as well as apply the solution potential. Thus, the on-chip electrodes would serve the dual purpose of electronic desalting as well as gate biasing in order to facilitate sensing experiments in a tiny droplet. In addition, we also outline a pathway for fabricating CMOS compatible high surface area desalting electrodes and examine their capacity to meet these specifications[1].

6.1 Biasing the transistor-in-a-droplet

Figure 6.1 shows a schematic of biasing the FET inside a microdroplet. An important advantage of the desalting electrodes in this system is that they can act as compact reference electrodes. We can leverage the fact that the desalting electrode pairs exhibit bilateral symmetry about the device. During the desalting process, they are also electrically biased in a symmetric manner so that ions redistribute equally away from the sensor. Although these electrodes polarize, the apparent solution potential is always neutral and (ideally) at the midpoint with respect to both electrodes. Therefore, it may be possible to offset the reference solution potential about which the desalting voltages are applied on either electrode without any diminishing effect on the desalting process itself. By matching this reference solution potential with the transistor gate bias, we will end up turning on the FET while the desalting process is occurring in the background electrolyte. In essence, the desalting bias $V_{Desalting1}$ and $V_{desalting2}$, respectively, are applied in such a way that the gate

[1]Results discussed in this chapter are published in [88], [97] and [98]. Reproduced with permissions from AIP and RSC.

bias, V_g follows from equation 6.1:

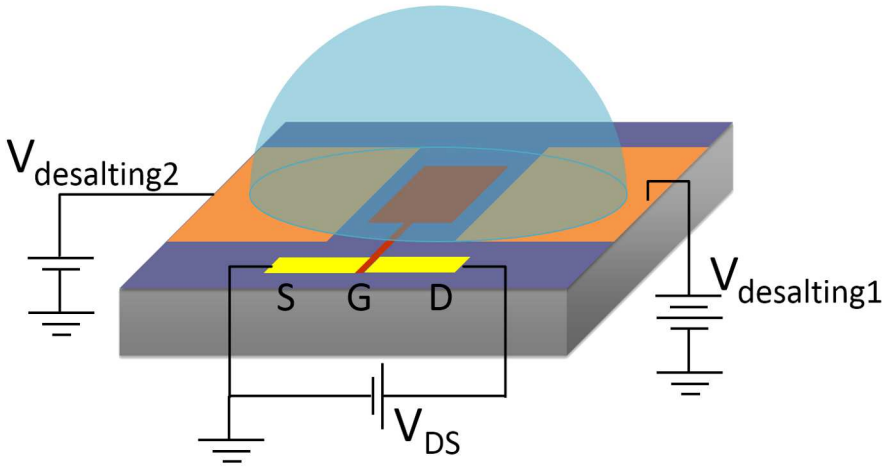

Figure 6.1: Schematic of a field-effect sensor in droplet with simultaneous desalting and gate-baising using on-chip electrodes.

$$V_g = \frac{1}{2}\left(V_{Desalting1} + V_{Desalting2}\right) \tag{6.1a}$$

$$\Delta V_{Desalting} = |V_{Desalting1} - V_{Desalting2}| \tag{6.1b}$$

6.1.1 Back-diffusion of ions v/s sensing process

An important consideration pertains to the time-scale of desalting pulses so that they are compatible with sensing schemes. Following the desalting step, if we ordinarily turned off the desalting bias and applied the gate voltage, sensing would have to be completed within a time window that is limited by ion back-diffusion. The latter follows a timescale of $\tau = {}^{L^2}/_{2D}$, where, L is the characteristic separation length and D is the ion diffusivity. With L ranging from 10-100 μm and $D \approx 10^{-9}\ m^2/s$ [99], back-diffusion occurs within seconds of turning off the polarizing field. It is, therefore, vital to combine both desalting and sensing in a single step before the background shielding recurs. Our on-chip electrodes and biasing scheme described above in equation 6.1 can provide both functions simultaneously and circumvent the back-diffusion problem altogether. Such a construct can also be scaled out to enable sensing in droplets that can each be independently addressed in a multiplexed system.

6.1.2 Device response in microdroplets when gating with on-chip electrodes

Transfer characteristics for both NMOS and PMOS devices were analyzed using the on-chip Ti/Pt electrodes for gating. Microdroplets (1mM) were deposited using an IM-300 programmable microinjector (Narishige, Japan), with a 4 μm inner diameter glass transfer-tip (Eppendorf, NY, USA) positioned precisely by a 3-axis micromanipulator. Electrical characteristics of FET devices and desalting measurements were recorded using a Keithley 4200-SCS 4-Channel Parameter Analyzer (Keithley Instruments Inc., OH, USA). the solution included 13.5% glycerol added in order to stabilize the droplet in air and prevent evaporation, without significantly modifying the electrical conductivity [100]. In these experiments, both on-chip electrodes were swept at a constant rate of 20 mV/step. $V_{Desalting1}$ was biased over the range of -0.5 V to 2.5 V for NMOS (figure 6.2(a)) and 1.5 V to -1.5 V for PMOS (figure 6.2(b)) devices. A fixed offset was maintained with respect to $V_{Desalting1}$ for sweeping $V_{Desalting2}$ in order to introduce simultaneous desalting, i.e., both the on-chip electrodes were swept, but $V_{Desalting2}$ had a voltage lag of $\Delta V_{Desalting}$. The FET was cycled between off-on-off states for 5 cycles in each case, with ample time for ions to equilibrate between the desalting experiments.

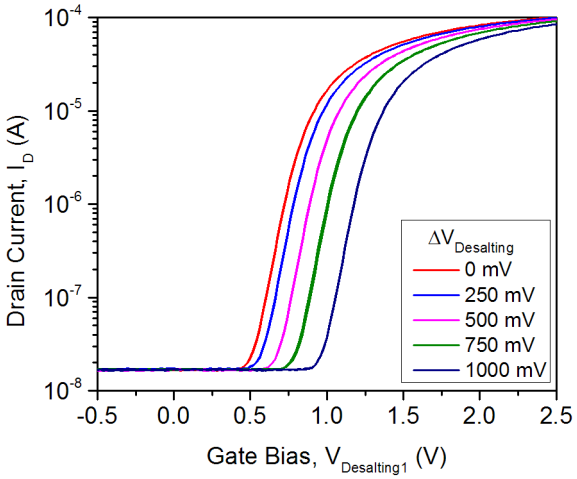

(a) $I_d - V_g$ characteristics of an NMOS device (W/L = 0.5 μm/0.3 μm)

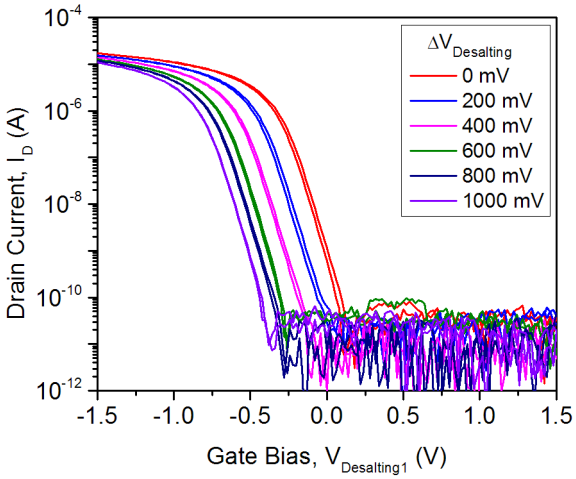

(b) $I_d - V_g$ characteristics of an PMOS device (W/L = 2 μm/0.3 μm)

Figure 6.2: FET gating with on-chip Pt electrodes by sweeping the apparent gate bias in a 1mM <1 nL droplet. Curves are plotted w.r.t $V_{Desalting1}$ to demarcate the desalting offset in each case.

As seen in figure 6.2 for both NMOS and PMOS devices, the on-chip electrodes provide stable gating conditions for conduction through FETs. To clearly differentiate the $\Delta V_{Desalting}$ between the experiments, we have plotted the characteristics with respect to $V_{Desalting1}$ alone. With each increment of the desalting bias, we observed that the characteristic curve shifted by a value (nominally $\frac{1}{2}\Delta V_{Desalting}$) that followed

the apparent gate potential established in the bulk of the droplet. We also analyzed the variations across 5 sweeps in both cases. For the NMOS device, the standard deviation in apparent V_g value was 3.43 mV (at $I_{DS} = 10\ nA$) while the PMOS device was more stable 1.34 mV standard deviation in V_g (at $I_{DS} = 100\ nA$). For an ideal HFO_2 gate dielectric with 59 mV/pH sensitivity, these would translate to pH resolution of 0.058pH and 0.023pH units, respectively. Between the various experiments, the desalting process did not cause any apparent irreversibility that interfered adversely with the FET characteristics. The desalting transients during these experiments are discussed in section 6.4, where the performance of the on-chip desalting is analyzed together for smooth as well as increased area electrodes.

6.2 pH sensitivity with on-chip quasi reference electrodes

The on-chip electrodes can overcome size limitations of conventional reference electrodes to provide a convenient method of biasing the transistor in a microdroplet. Metals used as quasi reference electrodes (QREs) are polarizable and are therefore capable of desalting as well, subject to their redox potentials. However, unlike a standard reference like Ag/AgCl, their native pH response is non-zero and can also be very unstable in solution. In a recent study, we analyzed how the pH response of a Pt electrode can negate that of the HfO_2 surface of an EG-FET and render the device pH insensitive. As a workaround, by flipping the device and passivating the FET surface using a spin-on PVC coating, we could operate it as a Pt/PVC-REFET so that the pH response of Pt would be reflected in the gating potential [98]. This Pt/PVC-REFET had a sensitivty of $\sim$35 mV/pH and could be used to detect loop mediated isothermal amplification (LAMP) reactions.

Towards achieving an ideal micro-QRE, several methods have been studied as microfabrication techniques and sensors have evolved over the last two decades [101]. Van den Berg et al. [102] demonstrated one of the early miniaturized Ag/AgCl reference electrodes for ISFET pH sensors; but their performance was strongly limited by uniformity issues as well as choice of electrolytes. Issues associated with gate biasing of ISFETs through noble metal electrodes have also been studied in detail [103]. For the droplet-scale platform to be robust for large-scale indirect pH sensing applications, it is necessary to improve the on-chip electrodes to serve as ideal QREs. Although miniaturized Ag/AgCl has stability issues, Polypyrrole (PPy) deposition has worked as a very viable alternative for realizing the QRE on-chip. We have successfully implemented an electrodeposition process on various base metals and studied the pH sensitivity, resolution, stability and drift characteristics of PPy as a gating electrode (Duarte et al. [97]). Figure 6.3(a) shows details of the electrodeposition process with which PPy could be deposited near an EG-FET (top panel). Using cyclic

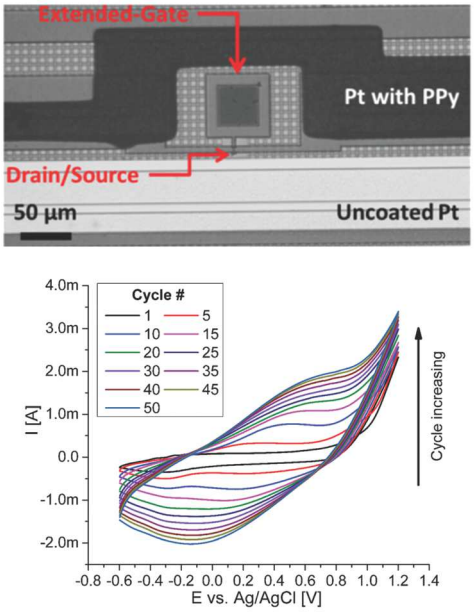

(a) Picture of PPy QRE near an EG-FET (top) and CV deposition process (bottom)

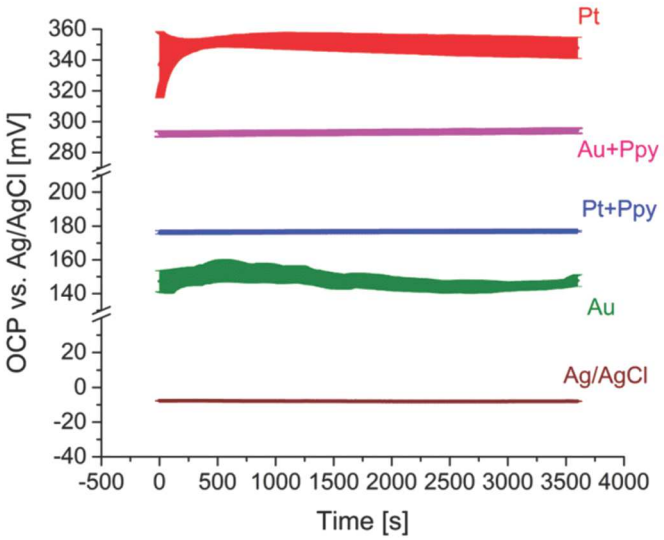

(b) Open circuit response v/s Ag/AgCl of PPy and noble metal QREs

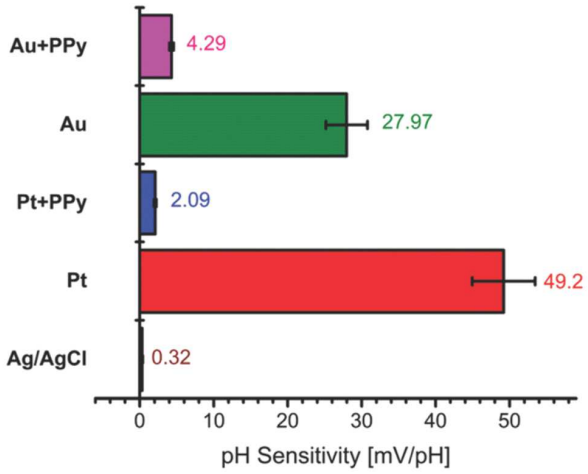

(c) pH sensitivity of PPy and noble metal QREs

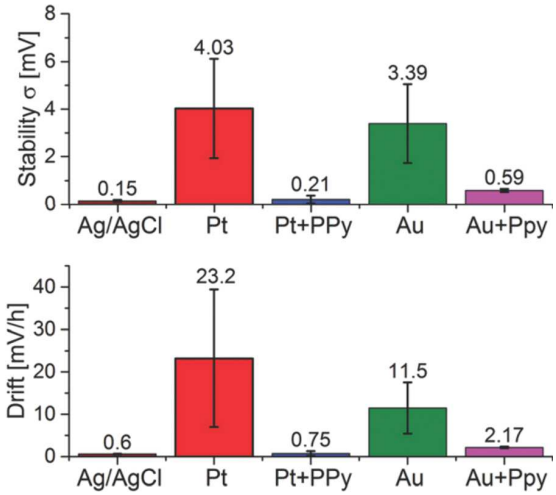

(d) Stability and drift characteristics of PPy and noble metal QREs

Figure 6.3: Polypyrrole QRE electrodeposition and characterization for pH sensing with EG-FETs.[2]

voltammetry (CV) with Ti/Pt as the working electrode that was cycled from -0.6 V to +1.2 V v/s. Ag/AgCl, we were able to deposit a thick film of PPy. The film thickness, surface area and morphology grew with the number cycles as indicated by the progressive increase in peak current. Figure 6.3(b) compares the open circuit voltage (OCV) of PPy with other QREs and the Ag/AgCl reference. While the noble metals, although inert are very noisy and drift in solution, PPy was very stable and had minimal drift. The pH

[2]Reproduced from [97], with permission from The Royal Society of Chemistry.

sensitivity of PPy was also dramatically reduced, especially with Pt as the base layer, and we achieved a 2 mV/pH performance. Further, the stability and drift parameters, which decrease the pH resolution, are summarized in figure 6.3(d). The PPy on Pt QRE again outperformed the noble metals with <1 mV/hr drift and a stability of 0.21 mV that nearly match the ideal case scenario of 0.15 mV measured for Ag/AgCl. Therefore, the PPy could effectively mask the pH response and instabilities of Pt, so that using this QRE for gating ISFETs can recover the near-ideal (59 mV/pH) pH sensitivity and 5X improved resolution.

6.3 High Surface Area Desalting Electrodes

In order to achieve the ultra-low V/SA ratio of 1 μm outlined in section 5.2.5, we need two orders of magnitude enhancement in the desalting surface area within the droplet. At the same time, the electrode surface must be electrochemically inert at large applied bias near the electrolysis limit, and also manufacturable in a CMOS-compatible process. Many options towards fabricating such high surface area (HSA) electrodes meet some (if not all) of these requirements. These include porous carbon black electrodes used in supercapacitors [104] and CDI systems [83, 89], nanostrutured nickel electrodes used in impedance sensing [105] or electroless gold electrodes deposited in nanofluidic platforms [106] . Platinum electrodes present a convenient choice of noble metal surface that can be easily electrodeposited [107]. Recently an electroless method has also been developed in the auto industry for two step conversion of magnesium, through dendritic silver, to porous platinum nanotubes by galvanic displacement reactions [108]. Although this process is not entirely CMOS compatible, the Ag to Pt conversion step can be coupled with Ag dendrites that deposit in the Ag^{+}/Si MACEtch process [109, 110] that is known to create nanostructures in crystalline silicon. However, we chose the Pt-black electrodeposition over other options on the basis of the process simplicity and controllability.

6.3.1 Electrodeposited Pt-black electrodes

High surface area platinum-black electrodes were prepared by known methods of electrodeposition [107, 111] of Pt-black. The deposition and electrochemical characterization were performed by a Gamry Reference 600 Potentiostat (Gamry Instruments, PA, USA). Pt-black was galvanostatically deposited over a seed layer of 1000 Å thick Ti/Pt from dihydrogen hexachloroplatinate (0.08mM $H_2PtCl_6.6H_2O$, Sigma Aldrich, with 0.25 g/L of $(CH3COO)_2Pb$, Alfa Aesar). Trace quantities of Pb^{2+} are known to facilitate better adhesion of the Pt atoms as they deposit on the cathode. The electroplating cell was configured as a conventional 3-electrode setup (figure 6.4). As shown in the schematics of the cell connections and the cartoon of the electroplating cell, the sample was connected to the working electrode of the potentiostat.

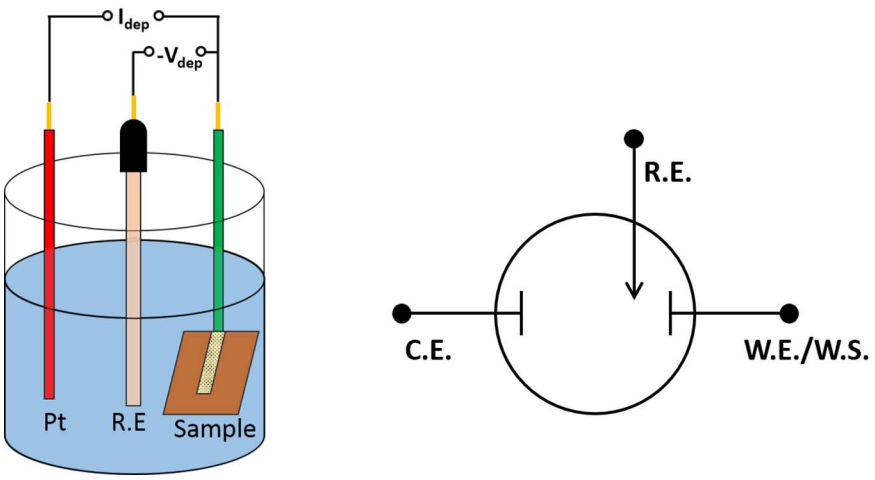

Figure 6.4: Schematics of the platinization process using a conventional 3-electrode electroplating setup.

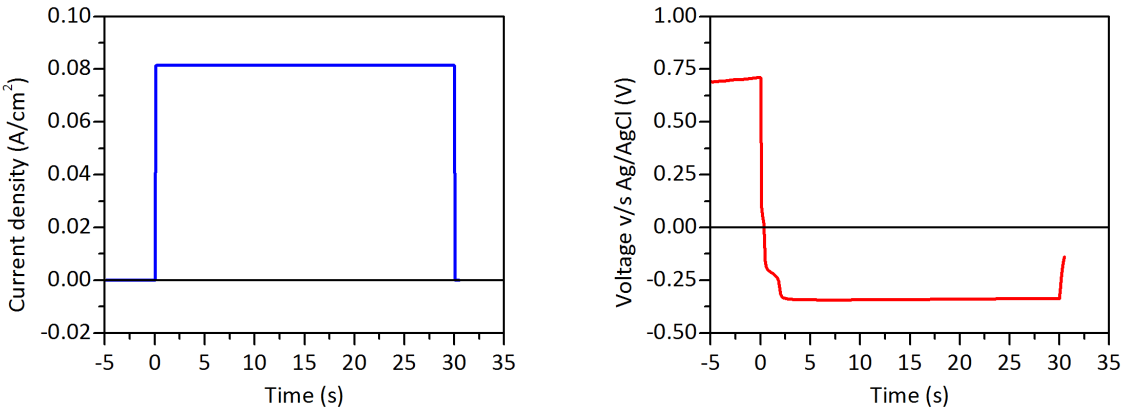

(a) Current density

(b) Cathode voltage

Figure 6.5: Electrodeposition conditions for coating Pt-black on Ti/Pt seed layers.

Galvanostatic deposition offers an important advantage over conventional potentiostatic deposition. By applying fixed voltages, although we can establish precise overpotentials at the cathode, the voltage drop due to uncompensated cell resistance cannot be controlled from one deposition to another. Alternatively, at a fixed current density in the galvanostatic mode, the voltage adjusts internally, the reaction rate is predictable and can be directly tuned to control the rate at which the metal layer thickness grows. Hence the reaction will be more repeatable to the tolerances of microelectrodes. Figure 6.5 shows the current density settings and measured cathode voltage during the Pt-black deposition on a test electrode. A constant current density of -0.08A/cm^2 was supplied to the W.E. v/s a leak-free Ag/AgCl (Warner Instruments, Boston, MA) that served as the reference electrode in the setup. However, the current was carried by a Pt auxiliary electrode

(C.E.). The nature of this electrochemical cell is that the electrolyte acts as the sacrificial source of Pt^{4+} ions that reduce to Pt at the W.E., so the anode (C.E.) is not consumed during the reaction. Therefore, the C.E. is a usually an ultra-pure Pt-wire or Pt foil. However, in order to deposit over micropatterned seed electrodes with low clearances, and maintain electrical isolation between electrodes, we modified the deposition cell such that the nearest neighbouring Pt electrode would serve as the C.E. while depositing on a given device. Further, reducing the current density by a factor of 5 gave better process control. Since the deposition was performed in galvanostatic mode, the constant current density ensured that mass transport rate during the Faradaic reaction was uniform throughout, and black platinum had deposited over the seed layer for a period of 30 s. The micrographs in figure 6.6 show test electrodes and on-chip electrodes around a FET before and after Pt-black conversion. Only one pair of the on-chip electrodes were converted in figure 6.6(b), and the structural photoresist that defined the reaction window was able to completely mask and passivate the traces. Using this process, we were able to repeatably platinize electrodes with high fidelity and achieve ($\sim$20 μm) isolation tolerance between adjacent electrodes or the device pad.

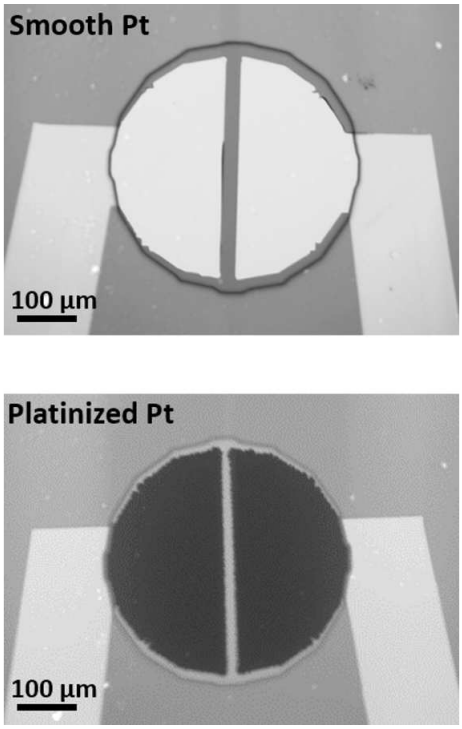

(a) Circular test electrodes on oxidized substrate before (top) and after (bottom) Pt-black deposition

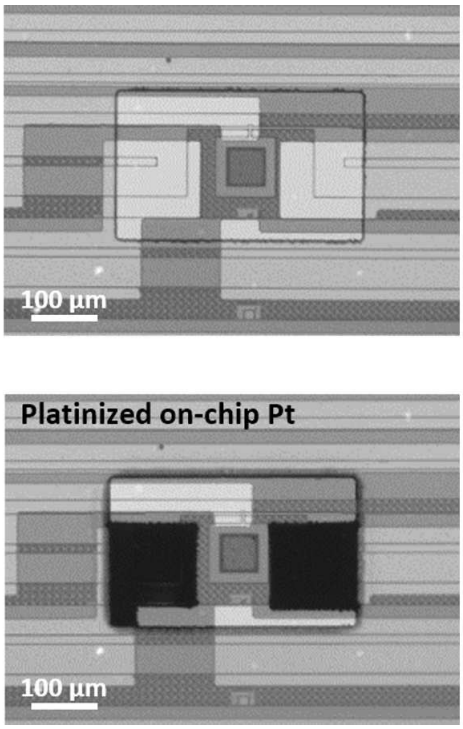

(b) On-chip electrodes around an EG-FET before (top) and after (bottom) Pt-black conversion of one pair

Figure 6.6: Micrographs of Pt-black electrodes deposited on Ti/Pt seed layers on chip.[3]

[3]Reproduced with full permission from [88]. Copyright 2015, AIP Publishing LLC.

6.3.2 SEM and AFM analysis

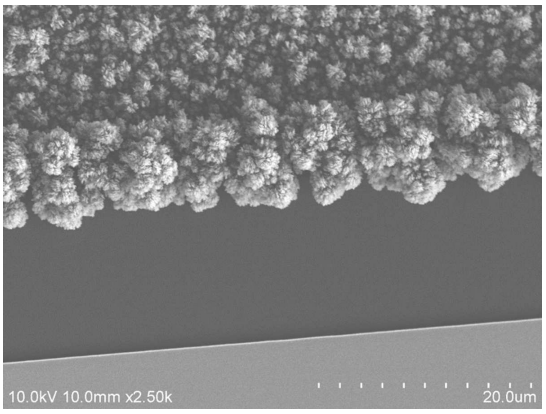

(a) Low mag. (2500X) indicates rough surface topology

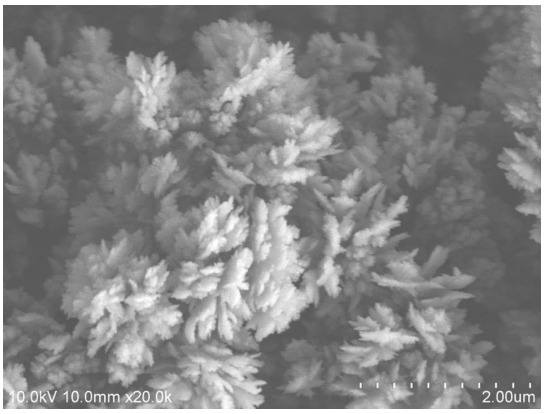

(b) At 20000X, the dendritic microstructure is visible

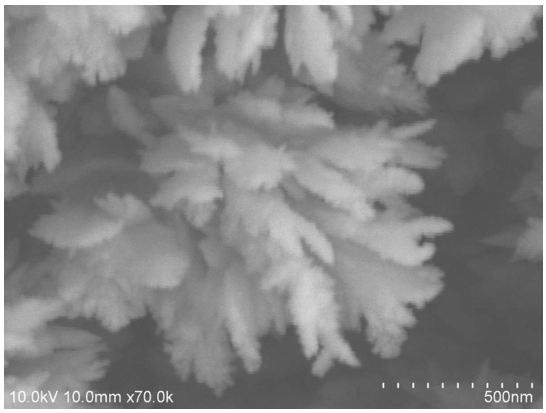

(c) High mag. (70000X) reveals ≤50 nm features

Figure 6.7: Scanning electron micrographs of Pt-black electrodeposited on semicircular test electrodes.[4]

Figure 6.7 shows scanning electron micrographs (SEM) of the electrodeposited Pt-black. The low magnification panel in figure 6.7(a) juxtaposes the edges of the post-deposition Pt-black electrode and the flat smooth Pt electrode below it. The smooth Pt was identical with the seed layer of Pt over which the electrodeposition was performed. By comparing both the electrodes, we infer that the Pt-black has an extremely rough, puffed up morphology that could be accompanied by significant area increase. Higher magnification (figures 6.7(b)) shows that the Pt-black had deposited with a very branched structure that was composed of dendrites arranged in a fractal pattern. This is typical of many electrodepositions that are performed at high current densities. A closer look at 70000X (figure 6.7(c)) revealed that the thickness of the dendrites and their tips were on the order of ≤50 nm. The microstructure and topology of the Pt-black electrodes in the SEM images of figure 6.7 are indicative of the large surface area increase that is required in order to

[4]Reproduced with full permission from [88]. Copyright 2015, AIP Publishing LLC.

magnify the EDL absorption for improved desalting.

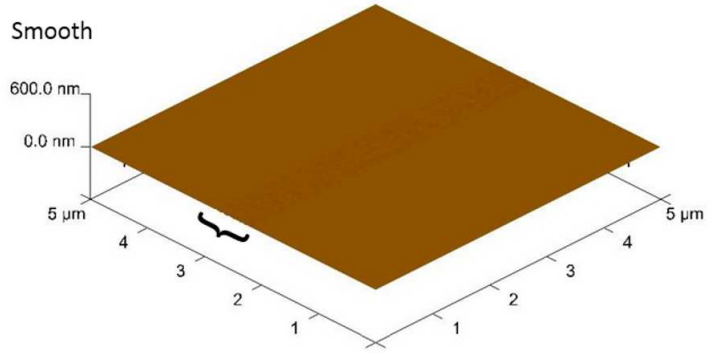

(a) 5 $\mu m \times 1\ \mu m$ scan of smooth Pt

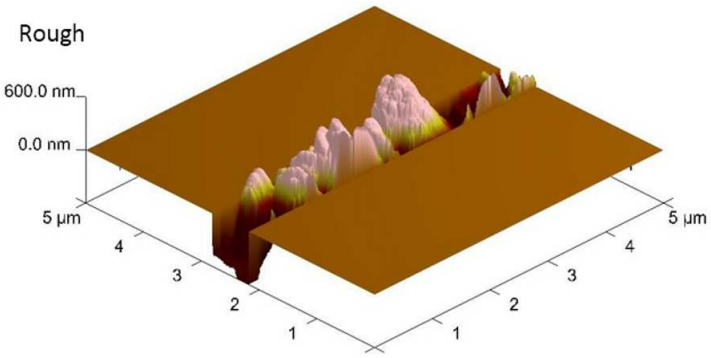

(b) 5 $\mu m \times 1\ \mu m$ scan of Pt-black

Figure 6.8: AFM scans of smooth Pt and Pt-black electrode surfaces.

AFM analysis of the platinized electrodes revealed the increase in surface roughness associated with the electrodeposited Pt. Figure 6.8 shows AFM scan profiles of 5 μm $\times$ 1 μm regions on the smooth as well as Pt-black electrodes. Table 6.1 also quantifies and summarizes this data over the scan region and a smaller 0.25 μm^2 sub-domain. Although SEM images revealed a characteristic branched and dendritic morphology, the AFM tip was only capable of scanning the peaks and valleys to within the tip's diameteric tolerance. The limited degrees of freedom of this measurement cannot afford the capability of direct physical scanning into the underlying fractal network of the electrode morphology. Nevertheless, we can still derive valuable information from the AFM data. From figure 6.8(a), we see that the smooth Pt had a nearly defect-free surface with <2 nm peak-to-valley roughness. However, we saw this increase by ca. 1000-fold in the case of the Pt-black electrode (figure 6.8(b)). RMS height deviations, which average over the region to smooth out point defects also confirmed a two-orders-of magnitude increase in the electrode roughness. However, although the surface area differences showed a similar trend, they cannot be used as a reliable standard to characterize these electrodes given the measurement limitations. For that purpose, it may be necessary to

obtain indirect measurements of area enhancement through adsorption phenomena.

	$5\mu m \times 1\mu m$ area		$0.5\mu m \times 0.5\mu m$ area	
Electrode designation	Smooth	HSA	Smooth	HSA
Projected area (μm^2)	3.08	3.08	0.249	0.254
Measured surface area (μm^2)	3.16	8.31	0.256	0.781
Surface area difference	2.65%	169%	2.71%	208%
Mean peak/valley height (nm)	1.77	265	1.78	159
RMS height deviation (nm)	2.26	320	2.25	184
Mean peak to valley depth (nm)	19.5	1512	13.3	850

Table 6.1: AFM surface roughness analysis of smooth Pt and Pt-black electrodes.

6.3.3 Electrochemical Impedance Spectroscopic Characterization

A rigorous examination of the surface area enhancement due to nanostructured rough electrodes over smooth Pt was performed using electrochemical impedance spectroscopy (EIS), a very well established technique for surface analysis of electrodes and electroactive microenvironments [112, 113, 114]. EIS measurements provide a convenient and reliable technique for identifying and analyzing various lengthscales and their associated phenomena in the electrochemical cell. Using a low magnitude 1-10 mV_{PP} signal and a 3/4-electrode potentiostat, we can perturb the electrodes across the frequency spectrum without driving any irreversible reactions. Figure 6.9(a) shows Bode plots of the impedance of circular test electrodes in bulk 1X PBS. These plots were generated by measuring the non-Faradaic response to small AC perturbations (10 mV_{PP} v/s Ag/AgCl) to determine the impedance of the desalting electrode as the working electrode. The AC sweep was performed across the frequency spectrum from 1 MHz to 1 Hz, with 10 points measured per frequency decade so as to span bulk, mass transport as well as surface dominant regimes. The plot shows a comparison of the impedance spectra between flat evaporated Pt electrodes and electrodeposited Pt-black. At high frequencies ($\geq$100 kHz), regardless of the electrode surface, impedance was dominated by bulk solution characteristics. However, interfacial characteristics became apparent at low frequency as we approached DC-like conditions. Surface area increase from smooth Pt to Pt-black is reflected in the large decrease in impedance magnitude at 1 Hz, or *left-shifting* of the phase minima towards lower frequency because of the increase in EDL capacitance.

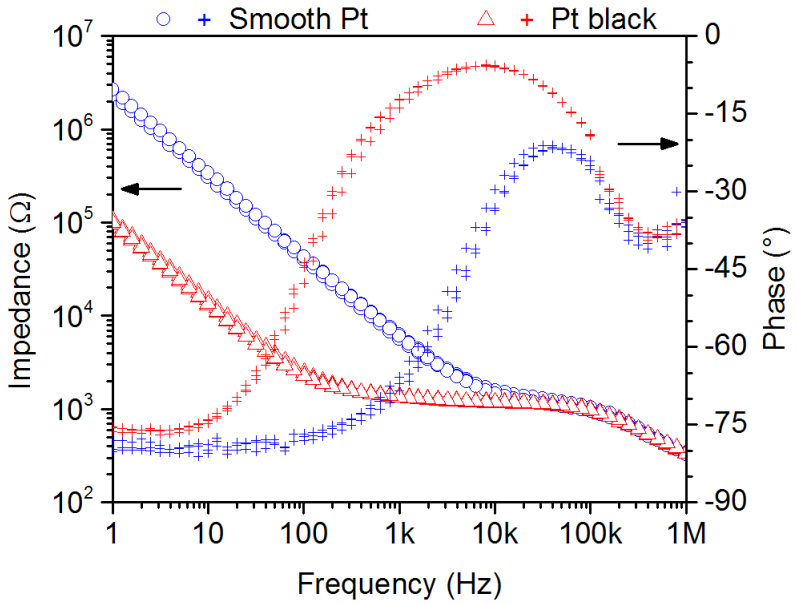

(a) Bode plot in 1X PBS

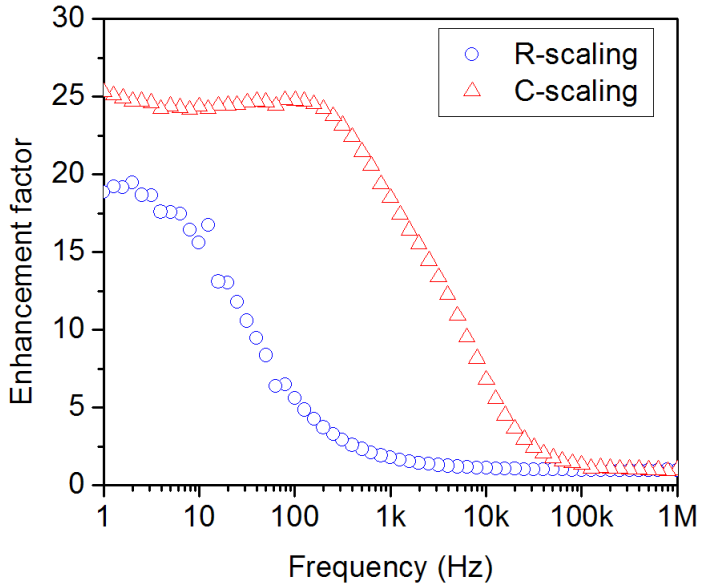

(b) C/C_{smooth} and R_{smooth}/R ratios

Figure 6.9: EIS analysis of smooth and nanostructured circular test electrodes for area enhancement.[5]

With the impedance (Z) and phase (ϕ) data, it is possible to decouple the various electrochemical phenomena as discrete circuit elements and construct equivalent circuits. Firstly, we can extract the components of Z— the resistive (real, $|Z\cos\phi|$) and capacitive (imaginary, $(2\pi f\,|Z\sin\phi|)^{-1}$) terms. Further,

[5]Reproduced with full permission from [88]. Copyright 2015, AIP Publishing LLC.

the phase is related to the frequency and R/C components as $\phi = \arctan\left((2\pi f RC)^{-1}\right)$. From both the resistance and capacitance data, we observed that the solution-limiting response at high frequency was independent of the interface whereas the clear scaling of nanostructured surface area came into play at low frequencies. The ratios of capacitances (C/C_{smooth}) or resistances (R_{smooth}/R) were then used to characterize the extent of surface area enhancement. Figure 6.9(b) shows a plot of the apparent area enhancement due to Pt-black versus frequency on the basis of these ratios. Note that because these calculations are based on phenomenological effects, the relevance of these values will follow the circuit elements that are factored-in and their respective frequency-responses. Hence the $1/R$ ratio trails the C-ratio albeit converging at the low frequency. From the circuit analysis, it was evident that although the dendritic nanostructure was expected to provide at least 2 orders of magnitude increase in surface area, we observed that the electrically available increment was limited to only ca. 25-fold.

6.3.4 Absorption enhancement through electrochemical treatment of Pt black

The SEM images and AFM data of the surface of Pt-black discussed in section 6.3.2 indicate drastically enhanced physical area. However, our experimentally observed increase in EDL absorption capacity from EIS measurements was limited to an order of magnitude (25X). This deficiency from expected improvement may be suggestive of a couple of limiting factors in play:

a) Incomplete coverage of the surface in contact with the droplet.

Nanostructured surfaces, by virtue of their roughness can exhibit hydrophobic characteristics and turn superhydrophobic. Due to the high surface area on the Pt-black and the tortuous morphology, the increased surface energy cost of the nanostructured electrode could have opposed proper wetting of the electrode and, hence, only a fraction of the true area might have been in apparent contact with the electrolyte.

b) Exclusion effects and steric hindrance to ion absorption.

The physical features of the electrode surface approached $\leq$50 nm, which was comparable with the phenomenological lengthscale, λ_D. The EDL formation on such a non flat, highly constrained surface with extreme curvature could be non-ideal, with exclusion effects coming in play at local regions of overlap. The apparent EDL capacitance could be dramatically diminished on such a heterogeneous surface [115].

Qiang et al. [116], have analyzed the problem of poor performance of Pt-based electrodes in microfluidic biosensors. By conditioning the electrode surface through repeated cyclic voltammetry (CV) treatment, they have shown that Pt surfaces, which appear typically passive immediately after microfabrication, can

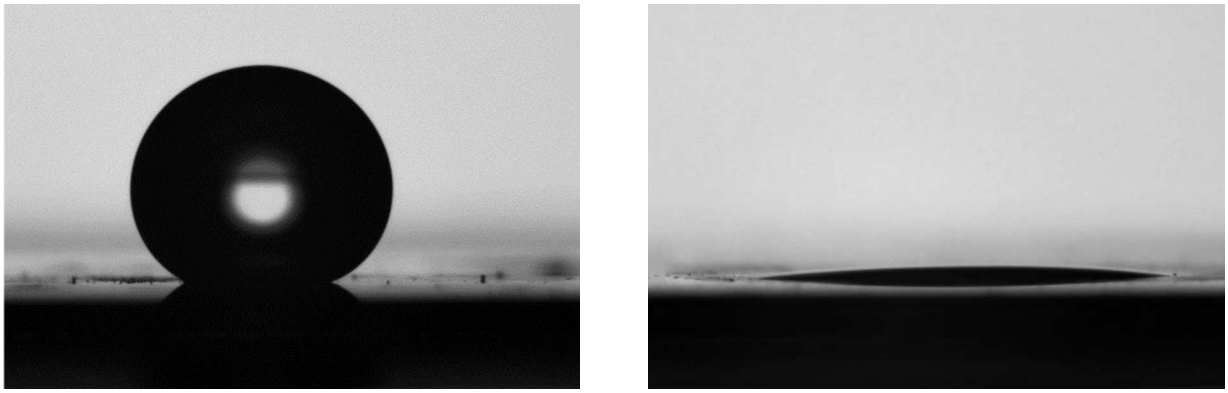

(a) Immediately after electrodeposition ($\theta = 166.4 \pm 5.2°$)

(b) After 5 CV-treatment cycles in 1X PBS ($\theta = 7 \pm 1.9°$)

Figure 6.10: Static contact angles measured with a DI water droplet on a Pt-black test surface.

be made sensitive for detection of H_2O_2 with several hours of stability. Incorporating this approach in our experiments, we were able to further improve and stabilize the surface characteristics of Pt-black for increased ion absorption during desalting. Test electrodes were cycled 5 times between -0.5 V and +0.9 V v/s Ag/AgCl at the rate of 100 mV/s in 1X PBS. Immediately after the conditioning step, we firstly observed a complete reversal in the wettability (figure 6.10). The Pt-black surface was extremely hydrophobic immediately after electrodeposition (figure 6.10(a)), with contact angle measured at 166.4°. However, after CV-treatment, the contact angle fell to as low as 7°, as seen in figure 6.10(b). The droplet spread spontaneously on the surface to confirm extreme hydrophilicity. This can provide the dual advantage of improved surface coverage for better EDL absorption, as well as easier microdroplet delivery and manipulation over the electrodes.

EIS results following the CV-treatment are also superimposed with the response of as deposited Pt-black and smooth Pt in figure 6.11(a). From the Bode plot in figure 6.11(a), we observed further decrease in the impedance at 1 Hz and left-shifting of the phase minimum to even lower frequency. These effects are both dominated by the contributions of increased surface capacitance to the circuit impedance ($1/2\pi fC$) at low frequency. From the overall EIS data, the resistive and capacitive components are both plotted in figures 6.12(b) and 6.12(a) respectively, for smooth Pt, Pt-black conversion as well as for the CV-treated Pt-black from a single specimen. The ratio of capacitances or inverse ratio of resistances capture the aparent decrease in impedance with the deposition of Pt-black and its subsequent electrochemical treatment. This decrease in impedance translated to a 4-fold further increase in area over as deposited Pt-black. Therefore, with CV treatment, the effective area of Pt-black electrodes approached ca. 100-fold over that of smooth Pt (figure 6.11(b)) which agreed with expected physical area increase in literature [107, 111]. With two-orders-of-magnitude effective surface area enhancement through nanostructured Pt-black and surface conditioning,

we can approach the desired V/SA ratio of 1 μm for the droplet that enables desalting of 10-100mM microdroplets as large as 100 pL to 1 nL around a field-effect sensor.

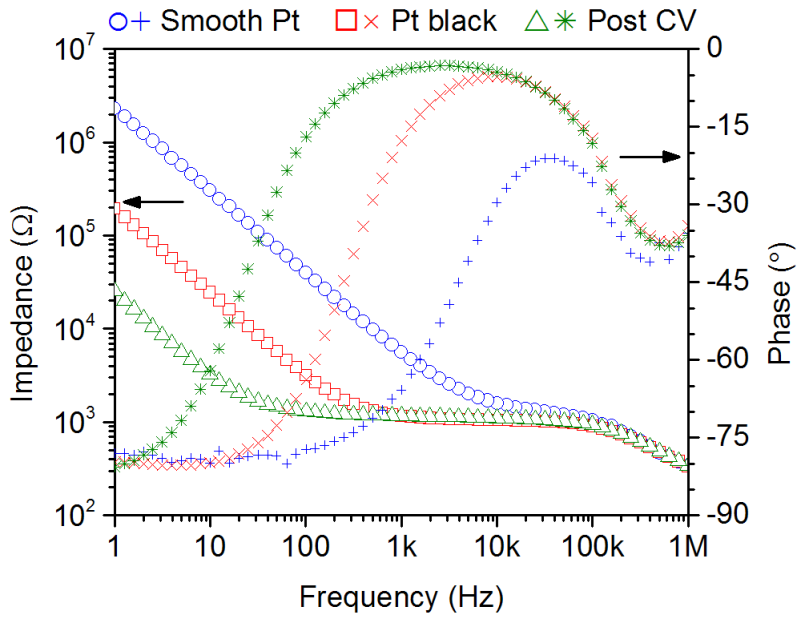

(a) Bode plot in 1X PBS

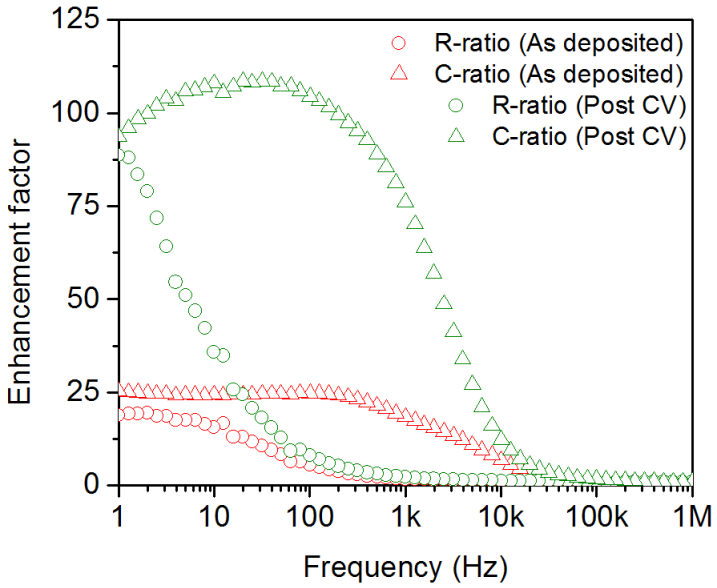

(b) C/C_{smooth} and R_{smooth}/R ratios

Figure 6.11: EIS analysis of nanostructured electrodes after CV-treatment, comparing with smooth and as deposited Pt-black electrodes.[6]

[6]Reproduced with full permission from [88]. Copyright 2015, AIP Publishing LLC.

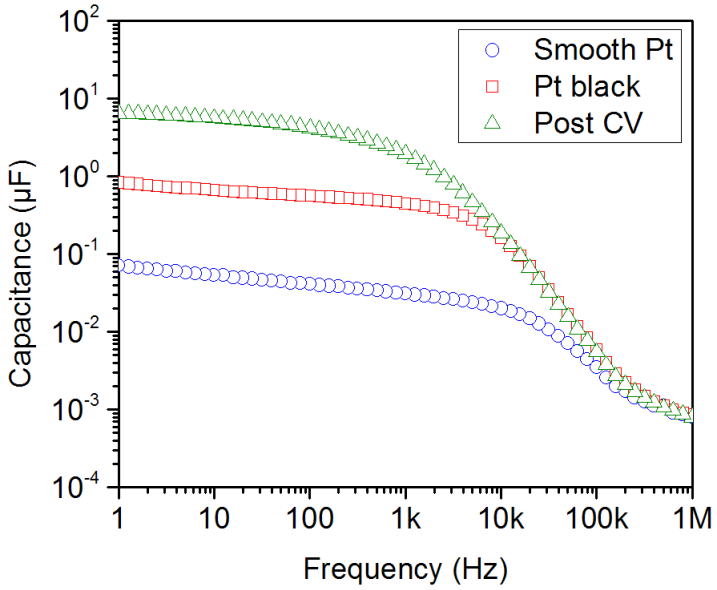

(a) Capacitive component versus frequency

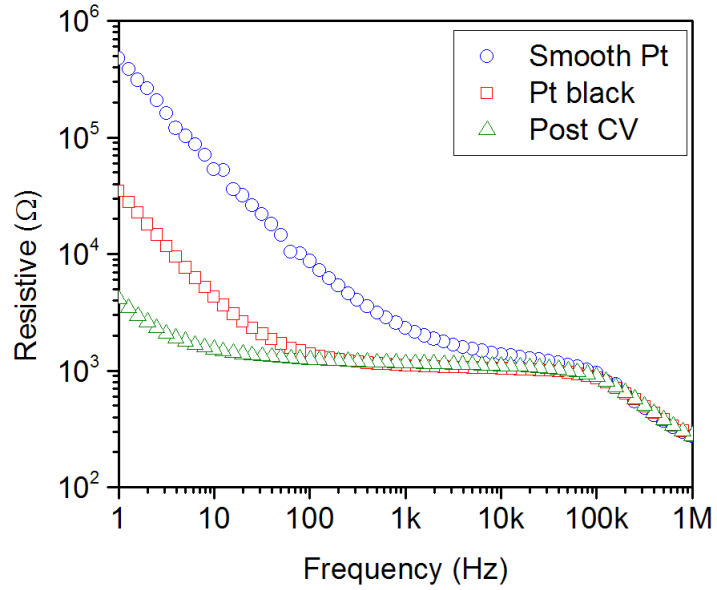

(b) Resistive component versus frequency

Figure 6.12: Plot of resistive (real) and capacitive (imaginary) components from the EIS response versus frequency for smooth Pt, as deposited Pt-black and post CV-treated sample.[7]

6.4 Electrical measurement of desalting performance

In the preceding sections, we established a biasing scheme in droplets, which can be implemented using the same on-chip electrodes while desalting, as well as a technique of increasing the electrode area to achieve the

[7]Reproduced with full permission from [88]. Copyright 2015, AIP Publishing LLC.

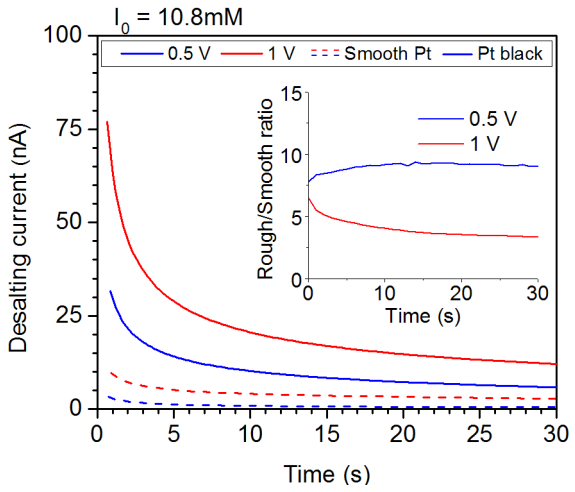

(a) Circular (250 μm dia) test electrodes. Inset shows HSA/smooth ratio at each time-point

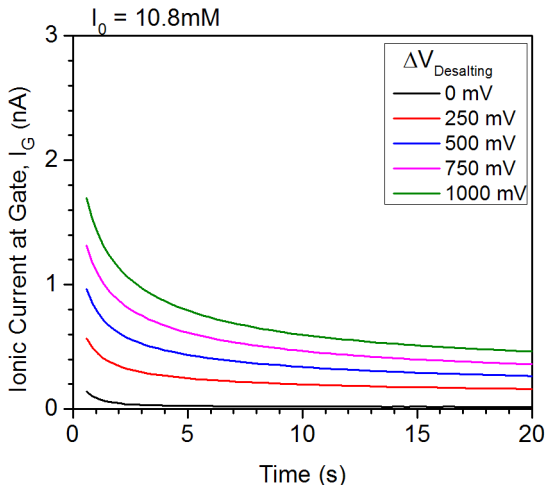

(b) Smooth on-chip Ti/Pt electrodes during PMOS biasing experiment

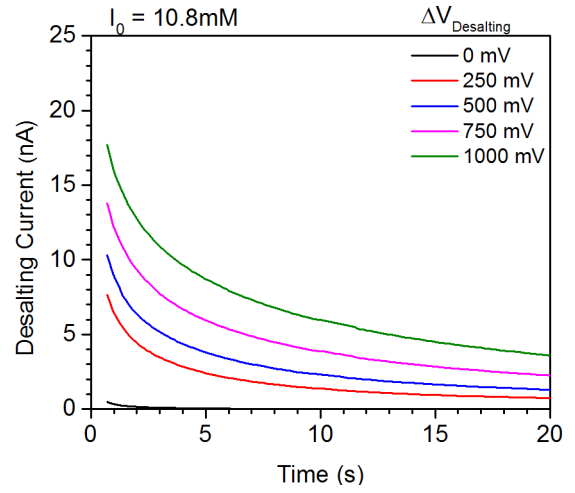

(c) HSA Pt-black (as deposited) on-chip electrodes during PMOS biasing experiment

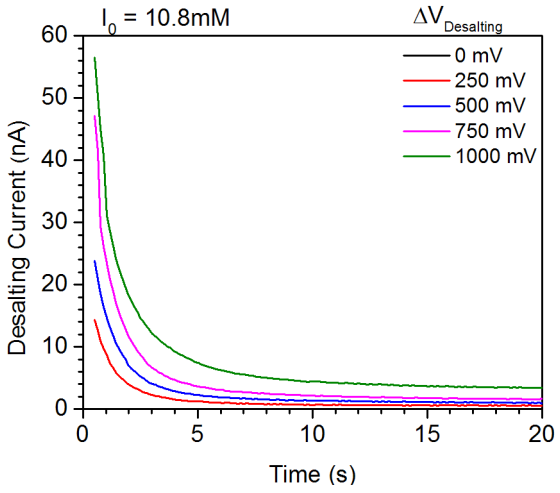

(d) HSA on-chip electrodes (after CV-treatment) during PMOS biasing experiment

Figure 6.13: Desalting performance characterization of test/gating electrodes, and surface area enhancements, using chronoamperograms of salt polarization with applied desalting bias. The curves are plotted for 10.8mM solution with neutral pH control.[8]

desired V/SA target. While electrochemical characterization showed that 100-fold eventual improvement of Pt-black EDL capacitance over smooth Ti/Pt was possible, the realistic desalting capacity can be analyzed from how the polarization transients scale in each case. As the electrodes absorb salts in the EDLs through capacitive charging, the blocking current (which tracks the flow of ions as they deplete out from the droplet) sharply decays over time. We show the increase in EDL absorption from smooth Pt to Pt-black, which was reflected in an equivalent increase of the ionic current.

Figure 6.13 shows the chronoamperograms that quantify the desalting capacity on both circular electrodes

[8]Reproduced with full permission from [88]. Copyright 2015, AIP Publishing LLC.

(figure 6.13(a)) and on-chip electrodes around a PMOS device (figures 6.13(b-d)), in 10.8mM (pH=7) 500 pL microdroplets, at various desalting voltages. During the experiments of figure 6.13(b-d), the FET was also simultaneously turned on. Note that the y-axis scales are different in each case and were chosen for better clarity to represent the data. Across all experiments, as expected from the theoretical discussion of chapter 5, we observed that the desalting ionic current sharply decreased over time with EDL absorption, as well as, increased at all time-points with increasing the desalting bias. Between the circular electrodes and on-chip electrodes, the trends were identical. The magnitudes in each case also scaled in close agreement with the ratio of their flat areas ($^{A_{circular}}/_{A_{onchip}} \approx {}^{24500\ \mu m^2}/_{\sim 10000\ \mu m^2}$). This confirmed the fact that although desalting and sensing processes are done in a combined manner, there is no coupling between the two phenomena as evident from the I-V's and desalting transients.

For the circular test electrodes (figure 6.13(a)), the ionic current transients at both low (0.5 V) and high (1 V) desalting bias scaled by an order of magnitude from smooth Pt to Pt-black. As depicted by the desalting current ratios in the inset of the figure, We saw an effective increase of 5 to 10-fold in charge uptake while desalting with Pt-black HSA electrodes in sub-nanoliter droplets. Again, this single order of magnitude increment was in general agreement with EIS data (figure 6.9), although we did not achieve 25X ratios because of the double layer compaction issues that are also at play in a full desalting experiment.

As the available surface area for desalting increased with Pt-black conversion of the on-chip electrode, the desalting transients measured during the FET operation also scaled in the same manner as that of the test electrodes. The current flowing through both the desalting electrodes perfectly mirrored each other ($I_{Desalting1} = -I_{Desalting2}$) and we did not observe any leakage current while the FET was simultaneously biased. Note that if any of these electrodes forms a short circuit with the source/drain terminals, then

a) gate leakage, $I_g > 0$, I_{DS} through the sensor will saturate such that $I_{DS} \approx I_g$

b) $I_{Desalting1} \neq -I_{Desalting2}$ and $I_{Desalting1} + I_{Desalting2} = I_g \neq 0$

In all three experiments, we observed both from I-V's and the ionic current (figure 6.13(b-d)) that the device was free from any leakage issues. Further, the effect of CV treatment was also evident from desalting current traces with the FET (figure 6.13(d)), which corresponded to ∼3X increase seen in EIS (section 6.3.3). With 100-fold effective surface area enhancement through nanostructured Pt-black and surface conditioning, we saw the effect of achieving the desired V/SA ratio of 1 μm that enabled realistic desalting of sub-nL droplets.

6.4.1 Net desalting capacity

The total desalting capacity of both smooth and HSA electrodes from these experiments is summarized in table 6.2[9]. Bulk measurements of the desalting capacity (in large 0.1 μL droplets) were also included as a control along with data for the microspotted droplets (500 pL). In the bulk system, with smooth electrodes, we observed negligible salt removal from solutions that contained more than 1mM of salt. This was in agreement with our calculations in chapter 5 (figure 5.6) as V/SA ratios ($\gg$100) were extremely unfavorable for desalting. The capacity improved as we approached the micro-droplet scale (V/SA$\simeq$100), although it was only realistic for depleting at the low end of electrolyte strength (<10mM). The HSA electrodes (V/SA$\simeq$1), however, demonstrated significant salt removal and we were able to deplete as much as 42% from 10mM and 5% from 100mM electrolytes.

Initial salt content	Percent salts depleted at 1 V desalting bias		
	Smooth electrodes in Bulk	Smooth electrodes in Droplet	HSA electrodes in Droplet
100mM	0.0025%	1.07%	4.73%
10.8mM	0.16%	6.85%	41.41%
1.17mM	1.5%	>99%	>99%

Table 6.2: Desalting capacities of various electrodes measured in bulk and micro-droplet.

Initial salt content	Initial λ_D(nm)	Final λ_D (nm)	Energy density (kJ/m^3)
100mM	0.96	0.99	912
10.8mM	2.93	3.82	862
1.17mM	8.87	$\gg$10	224

Table 6.3: Final depleted condition of microdroplet with HSA electrodes.

Table 6.3[10] further elaborates on the performance of HSA electrodes, From the point-of-view of field-effect biosensors, the effective Debye length would be the target metric for determing the effectiveness of desalting. The HSA electrodes in droplets achieved an effective value of $\lambda_D = 3.82$ from 10mM solutions. This would translate to ca. 30% improvement in molecular charge proximity to the sensor surface. With the area enhancement, surface treatment and reduction to the microdroplet-scale, electronic desalting can

[9,10]Reproduced with full permission from [88]. Copyright 2015, AIP Publishing LLC.

improve the response transducers such as nanowire FETs (whose sensitivity varies logarithmically with salt [62]) by perturbing at the biomolecular length-scales. Finally, table 6.3 also indicates the energy density from the amperometric measurement of the desalting process. Purely on the basis of electrostatic depletion, by treating the EDLs as ideal rejectate ($V_{Rejectate} \ll V_{Feed}$), it would require ca. 10-13 passes through an equivalent EDL desalinator to remove salt ions from a 100mM brackish sourcewater down to a target salinity in the 1-10mM range.

Chapter 7

Molecular sensing with arrays of FETs

7.1 The benefits of large FET arrays over individual devices

The size and scalability of FETs are ideal for label-free sensing platforms capable of high-throughput, multiplexed detection. This was particularly exemplified in the demonstration of whole human genome sequencing on chip by Rothberg et al. [45]. In addition to the need for transistor arrays for performing large sets of experiments, the capacity to package devices to high density on chip enables multiple measurements of every reaction. While most demonstrations of molecular sensing have been performed using a single device per reaction, these experiments would benefit greatly from improved statistical confidence of measurements that can effectively address errors that arise from yield issues, inhomogeneities within small reaction volumes and other external electrostatic disturbances. Using arrays of transistors and small reaction volumes will allow both sensing and control experiments in tandem under identical conditions. In this chapter, we discuss experiments of molecular sensing of miRNAs performed on large-scale transistor arrays.

7.2 Experimental

7.2.1 Array architecture and electrical testing

Figure 7.1 shows a foundry fabricated CMOS chip with large arrays of NMOS devices (Taiwan Semiconductor Manufacturing Company, Taiwan). As indicated in the figure, the chips contains either 128×128 (16384) or 1024×1024 (>1 million) device arrays and decoder circuits that toggle through individual FETs during electrical testing. Each sensor in the array can be thought of as a pixel. The schematic on the right shows the basic layout of a pixel, which is composed of two dual gate FETs [117]. Only one of the FET's gate oxide (100 Å thick) is exposed in solution and that serves as the actual sensor. The second transistor is embedded within a thick interlayer dielectric (1 μm thick SiO_2) and is used for row/column addressing of the pixel. The pixel to pixel pitch is 6.5 μm, which allows packing several devices (100's of FETs in a sub-nL droplet) in small reaction volumes. The wirebonded chip was tested using a custom-built PE16A/PEMU32 testing

board (OpenATE, Taiwan) and PXI-1033 platform (National Instruments, TX, USA). For all experiments described, the fluidic gate bias used was 2 V, supplied through a leak-free Ag/AgCl reference electrode.

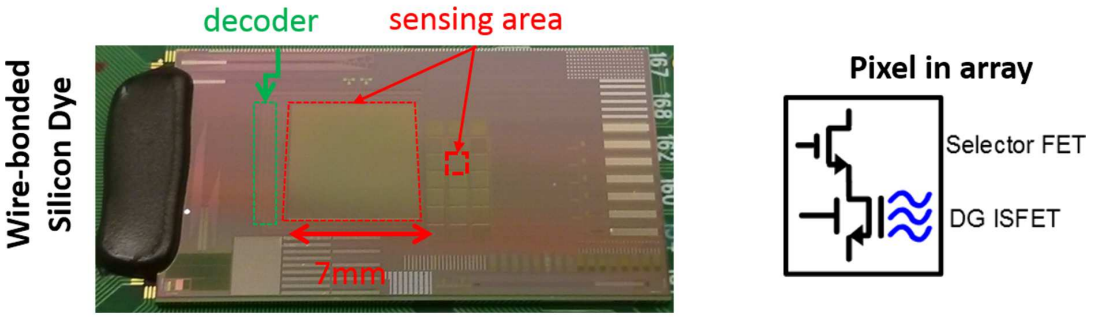

Figure 7.1: Photograph of the FET array chip indicating the positions of 128 × 128, 1024 × 1024 pixel arrays and decoder. Each pixel (schematic) represents an individual pair of sensing and selector FETs.

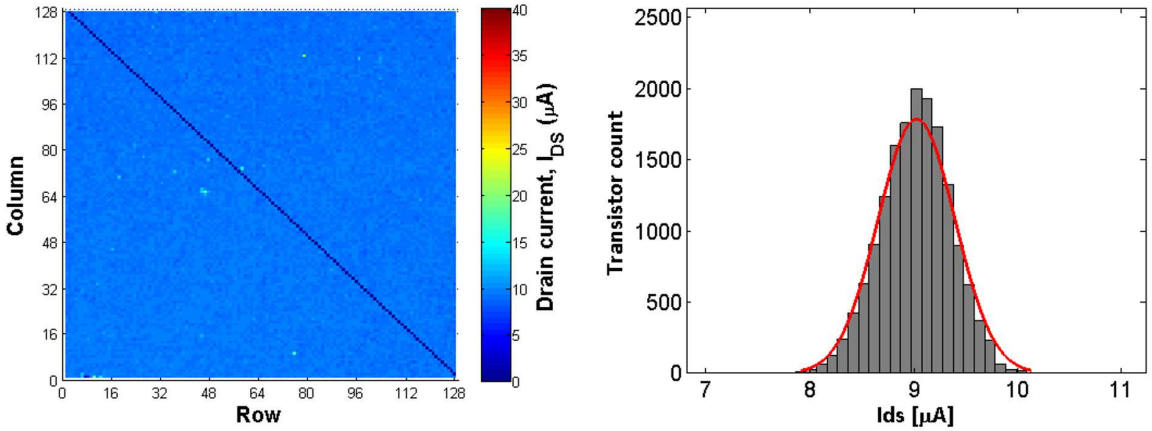

(a) Array heat map of I_{DS}

(b) Histograms of I_{DS}

Figure 7.2: Sample drain current (I_{DS}) measurements for a 128 × 128 FET array.

Figure 7.2 shows a complete measurement of all devices in a 128 × 128 array. The drain current through all of the FETs are plotted as a heat map (figure 7.2(a)) that spans the rows and columns of the entire array. Each pixel on the heat map corresponds to a single FET and the pixel color intensity is scaled according to the I_{DS} value as shown in the colorscale. The left diagonal of the array shows individual devices that were programmed as dummy pixels (always off) as a negative control for electrical test. Figure 7.2(b) shows a histogram plot derived from the heat map, with a normal distribution fit after eliminating the diagonal pixels. From the histogram data, even within such a large, dense array of identical devices, we can see that the statistical variations are significant to require multiple devices measuring each reaction. In the

experiments described subsequently, all data has been quantified using 10×10 pixel area (30-50% of the devices) within each reaction to account for the statistical variations.

7.2.2 Experiments performed

In order to study aspects of both upright and flat orientation of dsDNA over the sensor surface (section 4.3.1), we implemented two functionalization protocols using monofunctional silane SAMs [65]. To obtain the flat orientation, the reaction between the phosphate groups on the single strand and APDMES SAM was used. For vertical orientation, we used the covalent chemistry between amine-modified probe and epoxysilane SAM (3-glycidoxypropyldimethylethoxysilane (GPDMES)). Multiple spots of miR21 (match), let7a (mismatch) and DI water (negative control) defined both the capture and control analyte probes. We performed the following molecular experiments:

a) dose experiments (aminosilane chemistry) of probe dilutions from 50 μM to 100 pM to analyze threshold levels for probe attachment.

b) full molecular experiment (aminosilane chemistry) with probe dilution from 50 μM to 100 pM.

c) full molecular sensing experiment (aminosilane chemistry) with match/mismatch selectivity study using the highest concentration of 50 μM probes and 1 μM target.

d) full molecular experiment (epoxysilane chemistry) with probe dilution from 50 μM to 100 pM.

Electrical measurements were recorded after each of the following stages: silanization, probe attachment, blocking and, finally, after target hybridization. A low-salt buffer (0.01X PBS/2mM $MgCl_2$/0.02%SDS) was used after each step for the measurement. Optical measurements (after the probe attachment and hybridization steps) were also performed after rinsing and drying the chips following the electrical measurement.

7.2.3 Functionalization protocols

Chips were cleaned by degreasing with acetone, methanol, DI water and acetone rinses and dried with nitrogen. In order to protect the wirebonds, the rinsing steps (and all wet protocols) were performed in a 300 μL PDMS well. Surface hydroxyl groups were activated by treatment in a 100 W/1 mtorr oxygen plasma RIE (Thierry Corp., MI, USA). Following this step, the chips were placed in an airtight glass bottle with 50 μL of the silane solution and silanized in the vapor phase at 85°C overnight. After silanization the chips were cooled to room temperature and degreased to rinse away non-specific silane molecules from the surface. Sub-nL droplets of miRNA capture probes suspended in 5% glycerol/DI water were microspotted on the

chip surface using an IM-300 microinjector (Narishige, Japan) with the help of a 4 μm inner diameter glass transfer-tip (Eppendorf, NY, USA). After spotting, the chip was incubated at room temperature for 1 hour to allow molecular diffusion to the surface and subsequently heated in an oven at 85°C for 15 min to complete the probe-SAM attachment. The chips were then rinsed in a series of washing buffers (4X SSC/0.2% SDS for 5 min, 2X SSC/0.2% SDS for 1 min, 0.2% SDS for 1 min and DI water) with vigorous agitation through pipetting. After washing away any non-specifically attached probes, the chips were incubated for 30 min to 1 hour in a blocking buffer to cover any unbound functional groups. For APDMES chemistry, the blocking buffer was freshly prepared 1X Casein/PBS blocker. For GPDMES chemistry, a 50mM ethanolamine solution in 100mM Tris-HCl (pH 9.5) served as the blocker. Chips were rinsed again with DI water and hybridized with TxRed-labelled miR21 target (1μM) in a high salt buffer consisting of 0.8X PBS/2mM $MgCl_2$/0.02% SDS for 90 min. The chip was rinsed thrice with blank hybridization buffer and swapped with the low-salt sensing buffer (0.01X PBS/2mM $MgCl_2$/0.02%SDS) for the final electrical measurement.

7.3 Results and discussion

7.3.1 Probe dilution experiment

In order to resolve the limits of molecular absorption during probe functionalization as well as to observe how relative surface densities of the probes affect target hybridization, we did a dose experiment to observe the smallest possible concentration at which probes can be detected. By reducing the probe concentration, the amount of probe molecules that contact the surface also decrease in the diffusion-limited capture process. This might provide better control in defining a probe monolayer and steric relief as well during target hybridization. In this experiment, we compared the electrical and optical sensitivity across various dilutions (50μM, 10μM...100pM) of miR21-TxRed probe. DI/glycerol was used as negative control. Figure 7.3(a) shows the spotting protocol on the array where each titer was located. We can analyze the data by mapping these locations. Figures 7.3(b) and 7.3(c) show I_{DS} heat maps before and after capturing the probes. From the heat map in figure 7.3(c), we can clearly distinguish the 50μM and 10μM titers, while only a few pixels responded in the other titers. Figure 7.3(d) also shows fluorescence data for the array from the TxRed label. The optical and electrical array maps were well correlated.

Figure 7.4 shows histograms of I_{DS} shifts for 10×10 (100) pixels from each titer. The red bars indicate devices in the respective experiment, while the grey bars are from a reference sub-array that was chosen from pixels that were outside any of the probe spots. Therefore, they are common across all the plots. The distributions from 50μM and 10μM probe titers showed a statistically significant detection while the

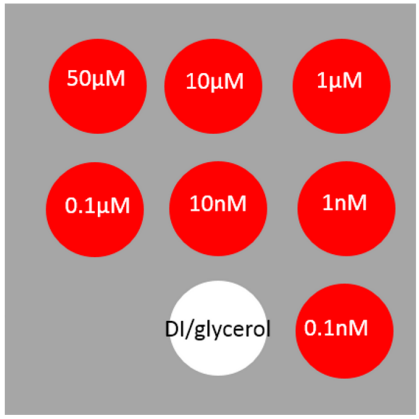

(a) Schematic of probe spot layout on array

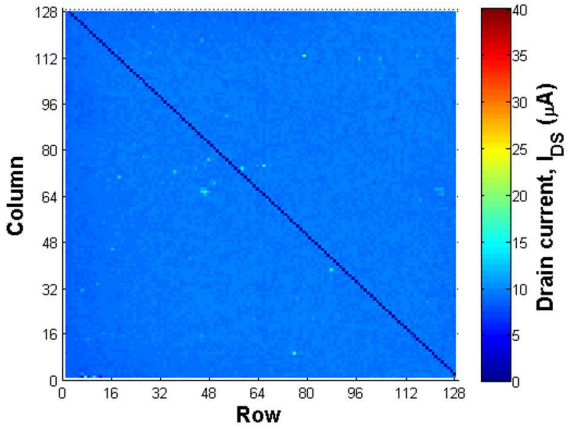

(b) I_{DS} heat map after silanization

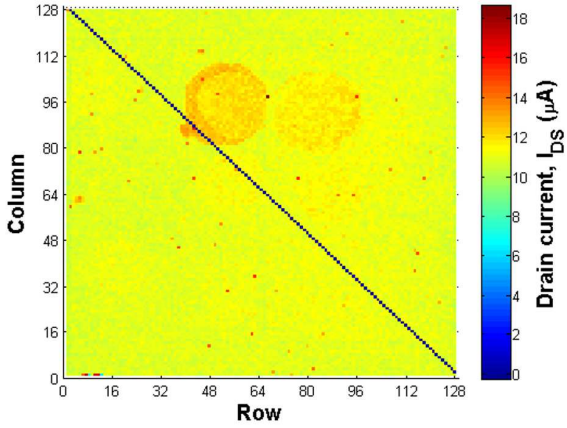

(c) I_{DS} heat map after probes spotting

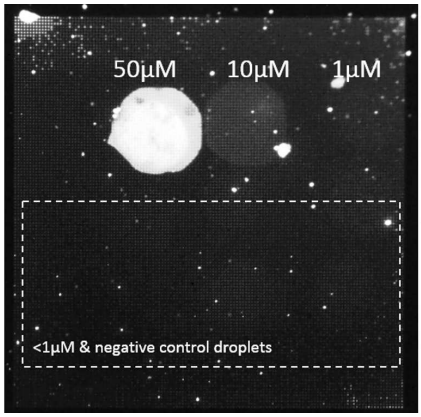

(d) Optical detection over whole array

Figure 7.3: Array data for probe dilution experiment with APDMES chemistry. The spotting schematic, I_{DS} heat maps after each step and optical detection of labelled probes are shown.

histograms from all other titers overlapped that of the reference pixels. Further, figure 7.5 plots electrical shifts v/s probe concentration for all dilutions (figure 7.5) as well as optical (figure 7.5(b)) data for the array. The optical response from the label decreased sharply with probe concentration and this trend is also reflected in the I_{DS} shift for the same array. The electrical response, though, also indicated variations within the array. From the error bars, pixel-to-pixel variations within the sub-array will decrease the signal-to-noise ratio and affect the resolution. The quantitative data thus emphasizes the importance of accounting for these variations through arrays. Although the histograms indicated discernible I_{DS} shifts at high concentrations, care is needed in factoring in the variations at low concentration. The pixel spread means that measurements based on single devices can conceal errors due to chip defects, experimental inhomogeneities and external noise.

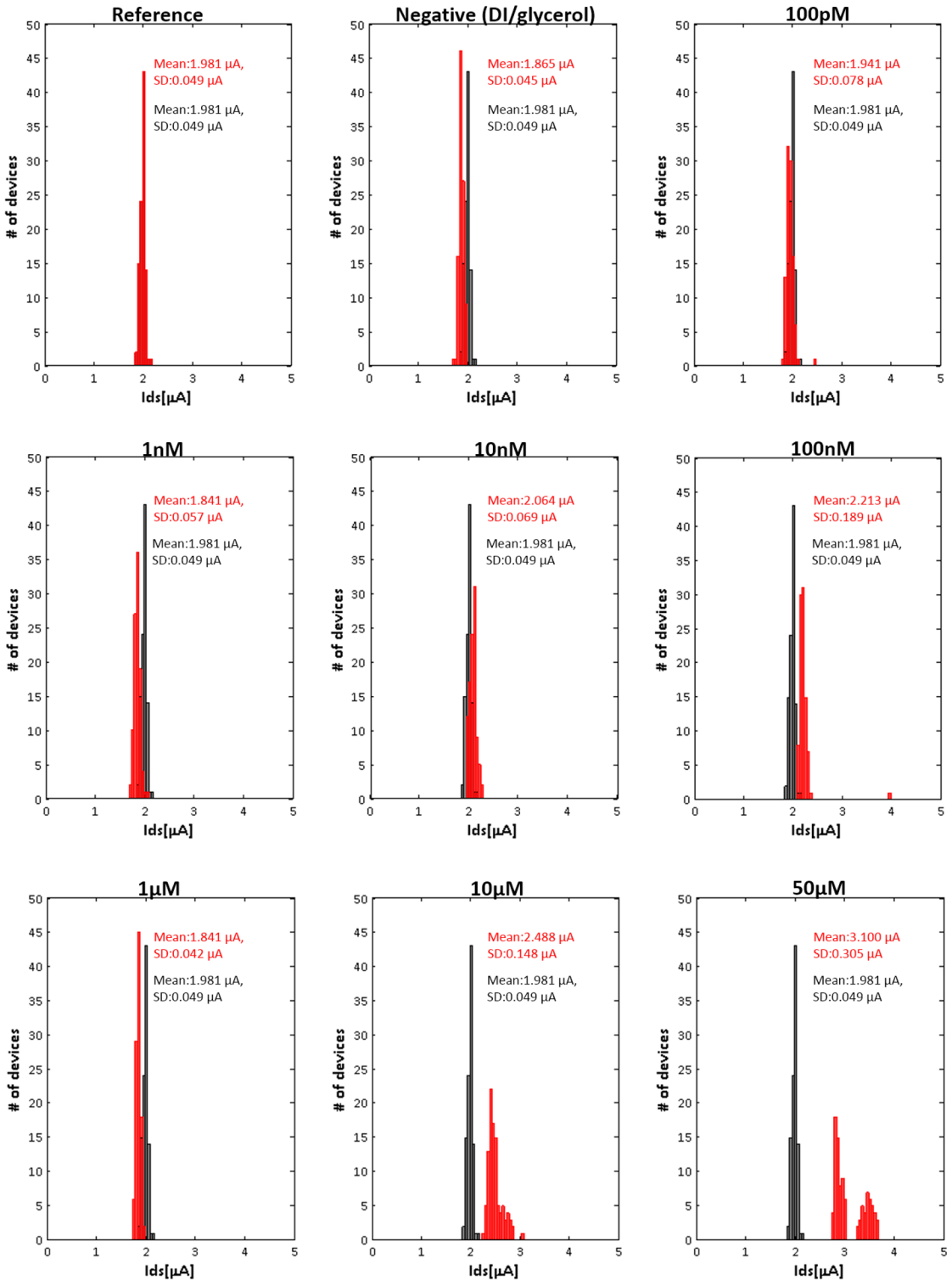

Figure 7.4: I_{DS} histograms of 10×10 pixels within each dilution (APDMES-chemistry) comparing probe shifts v/s reference shifts.

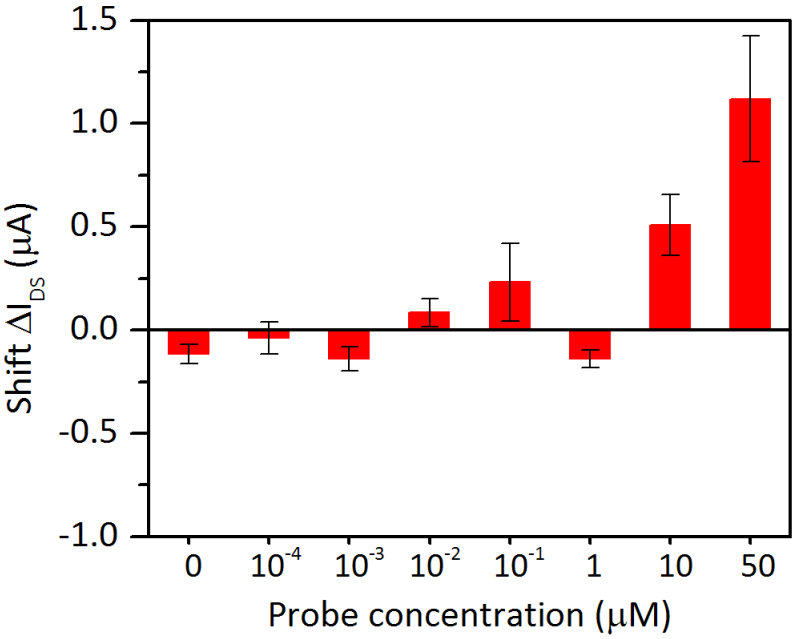

(a) Electrical shifts quantified from I_{DS} histograms

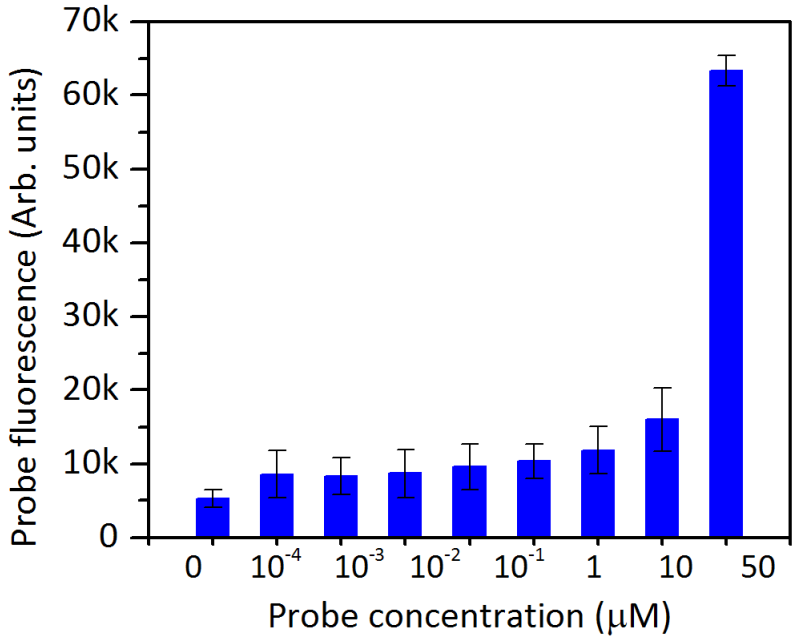

(b) Optical response of probe attachment across the dilutions

Figure 7.5: Electrical and optical quantitative data for probe dilution experiment with APDMES chemistry.

7.3.2 Full molecular sensing experiment with probe dilutions

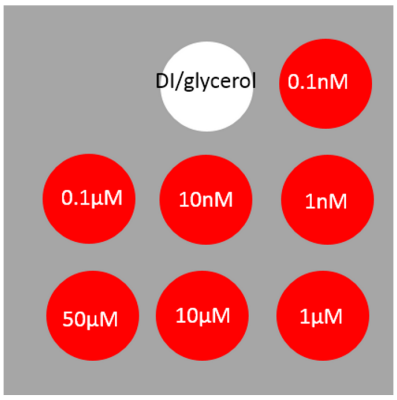

(a) Schematic of probe spot layout on array

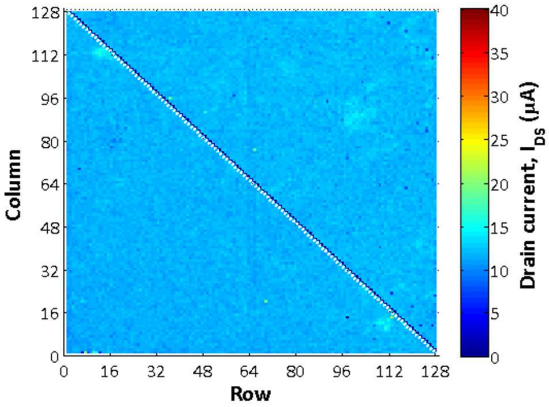

(b) I_{DS} heat map after silanization

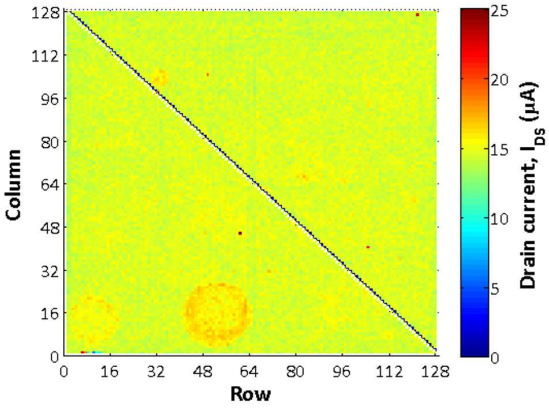

(c) I_{DS} heat map after probes spotting

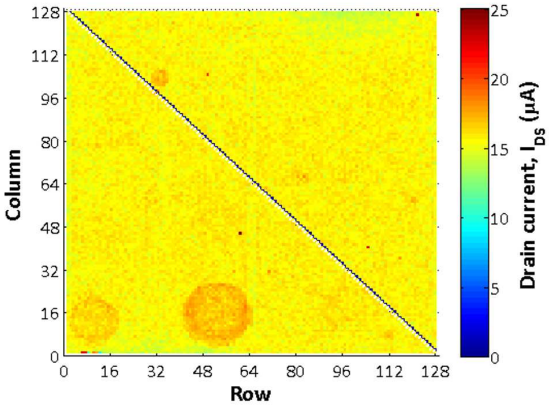

(d) I_{DS} heat map after target hybridized

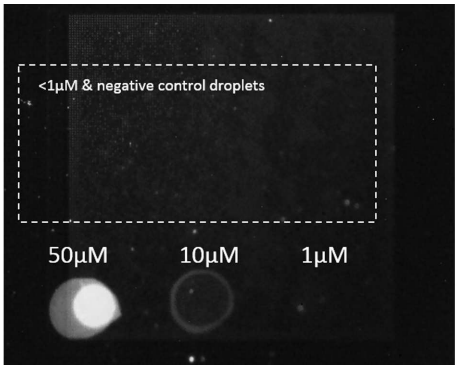

(e) Optical detection of probes over whole array

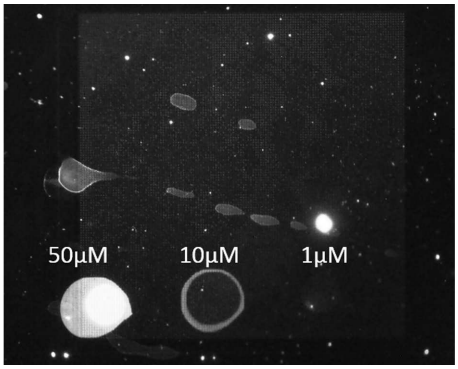

(f) Optical detection of target over whole array

Figure 7.6: Array data for full molecular experiment with probe dilution (APDMES-chemistry). The spotting schematic, I_{DS} heat maps after each step and optical detection of labelled probe and target are shown.

A full molecular sensing experiment using the dilutions of probes from above is described in figures 7.6, 7.7 and 7.8. The spotting protocol (figure 7.6(a)) was again identical with that of figure 7.3(a). In this

experiment, the miR21 target (with TxRed label) was hybridized for 90 min after blocking. The heat maps (figure 7.6(b-d)) again indicate the I_{DS} shifts after spotting the probe through color contrast from those pixels. However the probe to target shift (ssDNA to dsDNA) can only be discerned after subtracting the background change. Figure 7.6(e) and (f) also show the optical map of the array after both spotting and hybridization. The increase in intensity provides optical confirmation of target hybridization.

The histograms of I_{DS} in figure 7.7 are only shown for the high concentrations where we observed changes from the heat maps. Statistically significant shift was seen for the probes, although the 10μM titer had a stronger shift. The target histograms did not show an additional change from the reference due to hybridization. The negative control overlapped almost perfectly with the reference in this experiment. After quantifying the electrical data (figure 7.8(a)), we saw that the shifts after hybridization were not statistically significant compared to that of the probe itself. However, the optical data (figure 7.8(b)) showed a measurable change in the fluorescence at both 50μM and 10μM after hybridization. Since the optical response of hybridization was overwhelmingly larger at 50μM probe dose than other titers, and we did not observe any electrical shift at all in any of the spots, we performed the full molecular experiment with selectivity test at the 50μM probe concentration.

7.3.3 Full molecular sensing experiment

A full molecular sensing experiment with flat orientation was performed to detect miR21 with On/Off selectivity. Figure 7.9(a) shows the layout in which probes were spotted on the 128×128 device array. We used two spots each of the complimentary miR21 (match), let7a (mismatch) as well as DI water negative control probes. The capture probes were spotted at 50 μM concentration in order to attain maximum surface coverage. Electrical results of the whole array heat map are also shown after each step, including silanization (figure 7.9(b)), probe detection (figure 7.9(c)) and target detection (figure 7.9(d)). The heat map clearly shows shifts in I_{DS} immediately after the probe step. All 4 spots due to miR21 and let7a probes had shifted, as expected, because there is no selectivity between the oligonucleotides and the SAM. However, some pixels also responded in the DI/glycerol droplets even though no analytes were actually present. While the shift from probe to target is not visually obvious from the heat maps, we need to quantify the pixel shifts to analyze that.

Histograms of the electrical measurement (figure 7.10) show distributions of 100 pixels for a single droplet among each of the three sets of probes, both before and after hybridization. The histograms of the raw measurement indicate that the pixels corresponding to the miR21 and let7a probes were shifted significantly from the reference pixels due to the molecular layer. Both miR21 and let7a probe distributions confirmed

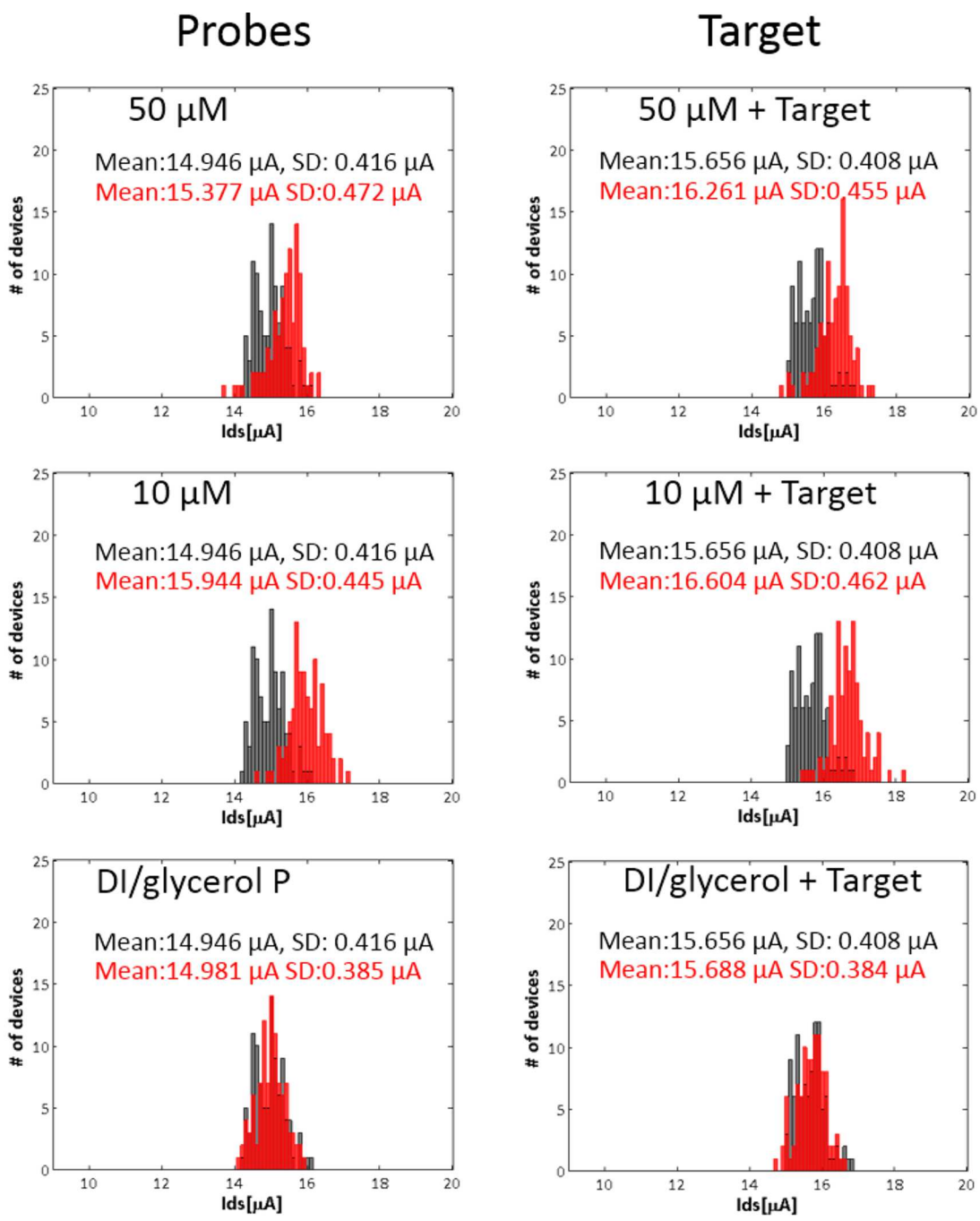

Figure 7.7: I_{DS} histograms of 10×10 pixels within each dilution spot (APDMES-chemistry) comparing probe and target v/s reference pixels.

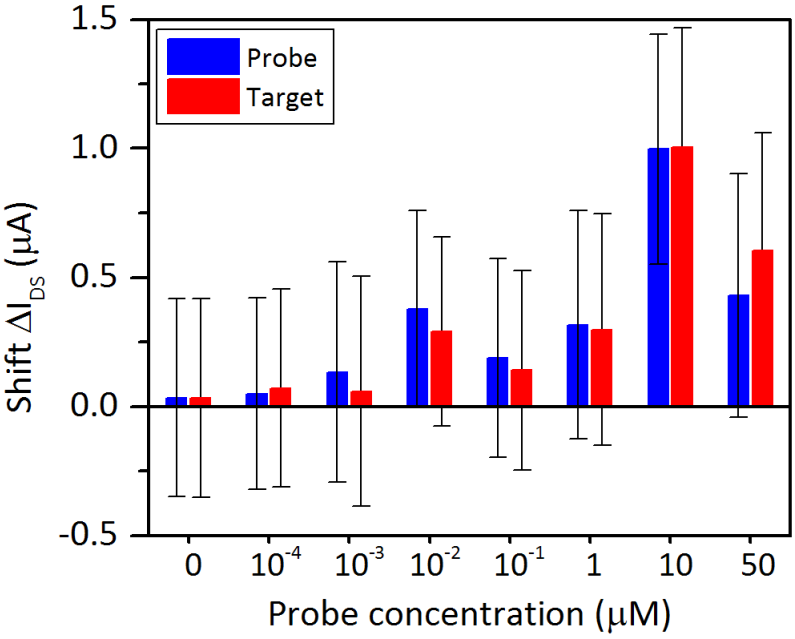

(a) Quantification of electrical shifts

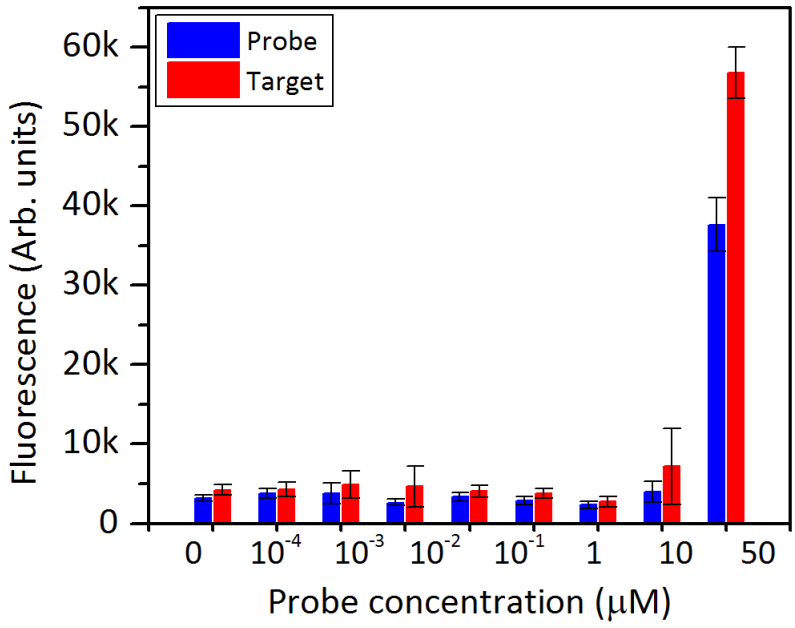

(b) Quantification of optical response with labelled target

Figure 7.8: Electrical and optical quantitative data for full molecular experiment with probe dilution (APDMES chemistry).

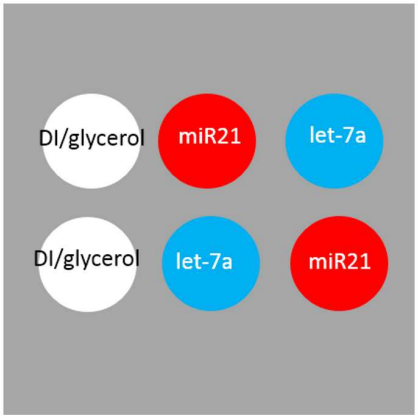

(a) Schematic of probe spot layout on array

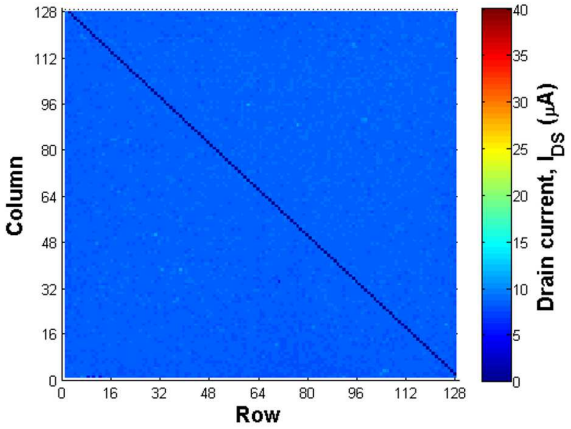

(b) I_{DS} heat map after silanization

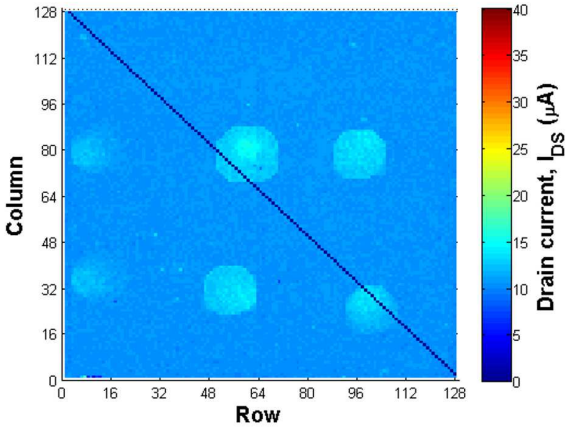

(c) I_{DS} heat map after probes spotting

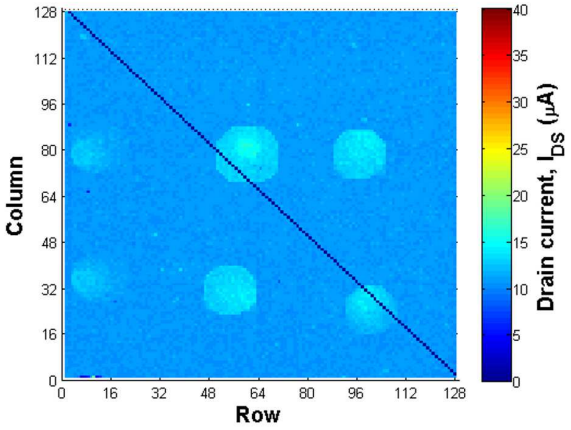

(d) I_{DS} heat map after target hybridization

Figure 7.9: Array data for the full molecular experiment (APDMES-chemistry) showing spotting schematic and I_{DS} heat maps after each step.

the fact that there was no selectivity between the two probes as they would have attached equally well with the SAM layer. However, for the DI/glycerol control spot some pixels overlapped with the reference while others had shifted. After the target hybridization step, the histograms (and mean values indicated) showed that the overall sub-array had not significantly shifted from probe to target.

Statistical data of the mean shifts and the spread within these sub-arrays are plotted in figure 7.11. The bar graphs show mean shifts in each spot from silane to probe (blue) and probe to target (red) after subtracting the reference pixel shift. The error bars were obtained for n = 3 separate arrays that quantify experiment-to-experiment variations. All 4 probe spots had equivalent response (∼2.5 μA), which was statistically significant against that of the negative control spots. P-values and levels of significance from the one-tailed t-test have also been overlaid for the data in figure 7.11. For probes, these were calculated

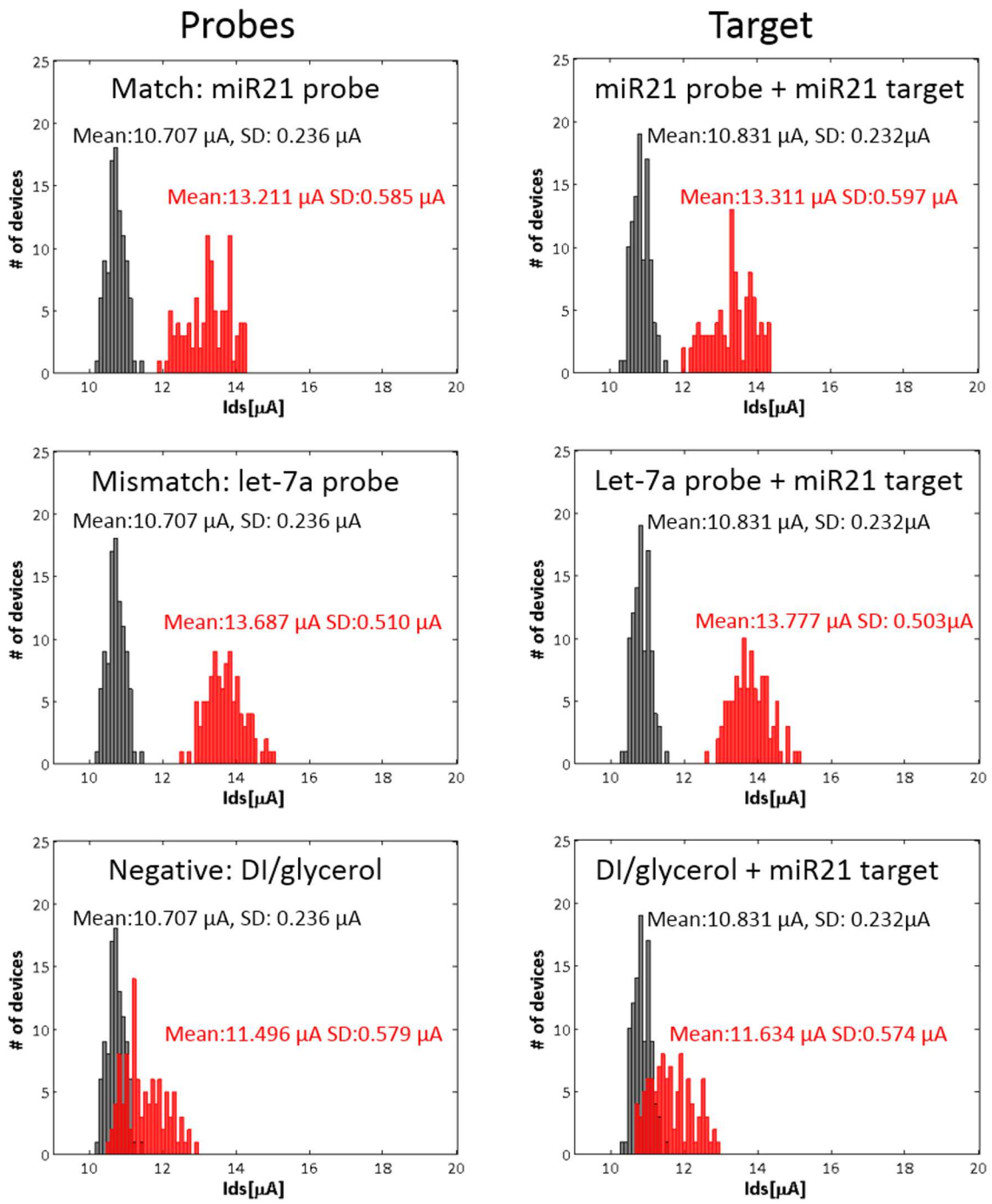

Figure 7.10: I_{DS} histograms of 10×10 pixels within each spot comparing probes and target detection v/s reference pixels in the full molecular experiment (APDMES-chemistry).

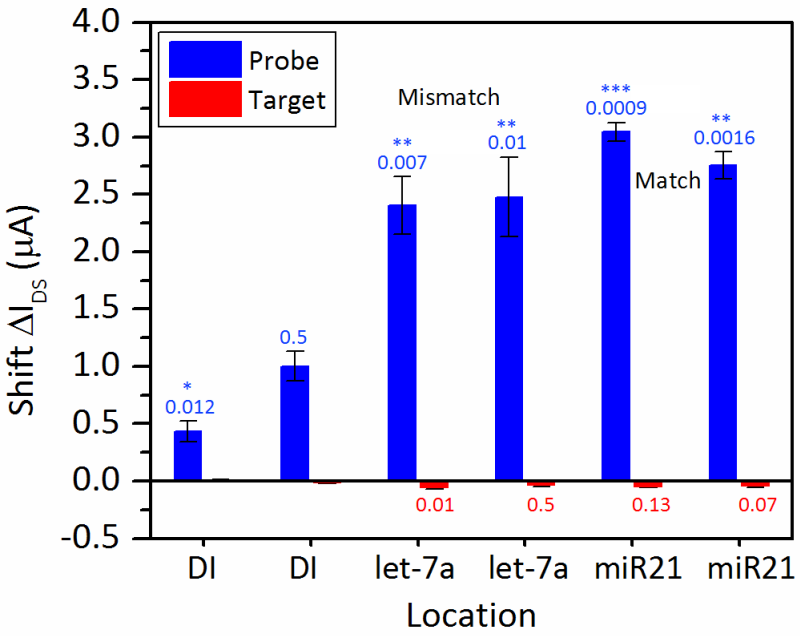

Figure 7.11: Quantification of electrical data for each spot in the full molecular experiment (APDMES-chemistry).

against negative control data (the worse of the two DI spots). For target hybridization, the p-value was calculated against the worse of the two mismatch spots. We did not compute p-values for negative controls. The test indicates statistical significance for probe detection and allows us to reject the null hypothesis, although the same is not true for target hybridization. From this experiment again, we were able to detect probe molecules repeatably. However, the fact that the devices did not respond to target hybridization could suggest a proximity issue because of multilayer formation in the probe step. Due to that, the target molecules may have been too far from the chip surface with respect to λ_D.

7.3.4 Full molecular sensing with vertical orientation

While we were repeatably able to detect probes electrically, the fact that target hybridization was not sensed electrically indicated that either we had a proximity issue of the hybridization occurring far away from the surface or poor hybridization efficiency. However, optical confirmation ruled out the latter. By changing the probe-attachment protocol to the epoxy-amine chemistry it was possible to interrogate the vertical alignment as a means of solving the above issue. In this experiment, amine-modified miR21 probes were used to covalently attach with GPDMES functionalized array. The spotting protocol was identical to that of section 7.3.2 (figure 7.6(a)). The probe was not optically labelled, but the target had a TxRed label

for final optical detection of hybridization. During spotting, the GPDMES-HFO_2 chip surface was more hydrophobic than the aminosilanized surface, therefore we had to dispense 3X to cover an equivalent spot area on these arrays.

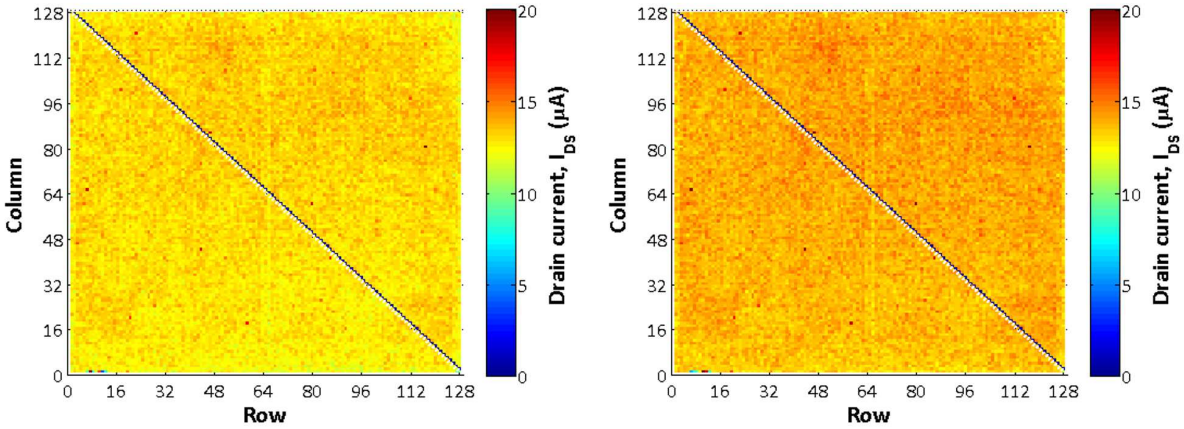

(a) I_{DS} heat map after probes spotting

(b) I_{DS} heat map after target hybridized

Figure 7.12: Array data for molecular experiment with GPDMES-Amino attachment chemistry showing I_{DS} heat maps.

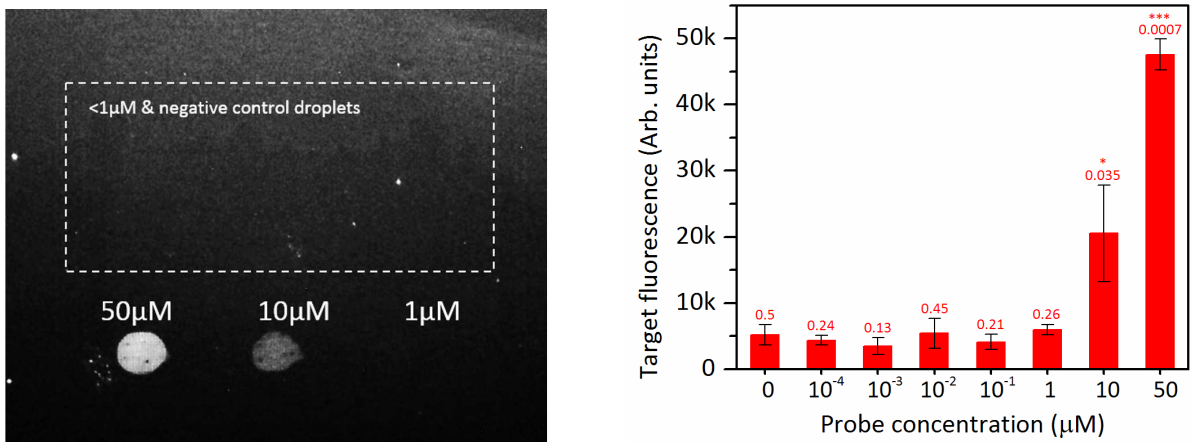

(a) Optical detection over whole array

(b) Quantification of mean gray value in each dilution

Figure 7.13: Optical detection of labelled miR21 target with GPDMES-Amino attachment chemistry.

Figure 7.12 shows I_{DS} heat maps after probe spotting as well as after hybridization. As seen in the heat maps, unlike with the aminosilane/flat orientation protocol, both probes (figure 7.12(a)) and target (figure 7.12(b)) were undetectable even at the highest concentrations. However, the optical measurement (figure 7.13(a)) showed visible target hybridization in the 50μM and 10μM probe spots. We quantified this

across multiple (n = 3) experiments. The data in figure 7.13(b) confirms hybridization at the highest probe concentrations. Further, because this experiment has built-in selectivity against non-specific attachment of target/GPDMES, that indicated insufficient probe capture from the low concentration titers. The p-values calculated against negative control for each of the concentrations also show that the detection was statistically significant only at the highest concentrations (10μM and 50μM). Moreover, the disparity between electrical and optical data indicates the possibility that probes may not be contacting down into the surface of the FET as effectively as it is depositing on the top surface of the array. If no analytes were attached, then we would only measure the bare device characteristic. Also, during the hybridization step, there wouldn't be receptors on the device so the electrical measurement in that case would also not show any shift due to the molecules.

7.4 Factors that could affect the electrical v/s optical response

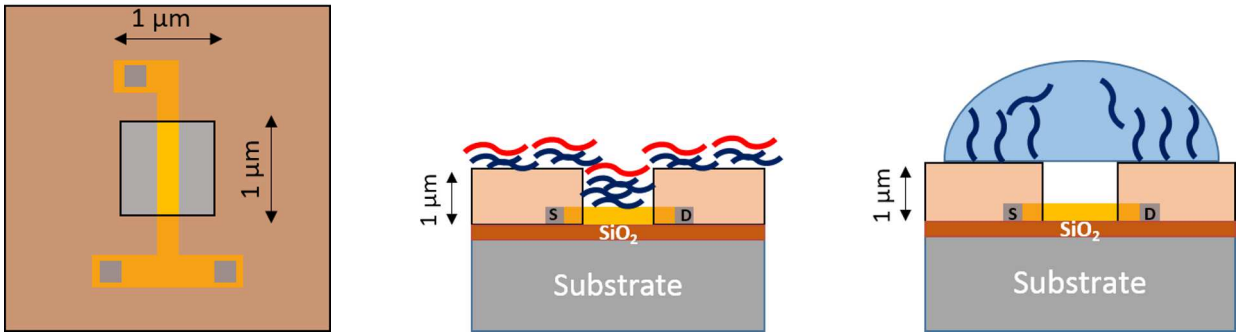

(a) Top view of etchback window opening over a FET in each pixel

(b) Multilayer probes stacking issue with APDMES/flat chemistry

(c) Wettability limits probe capture in GPDMES/upright chemistry

Figure 7.14: Schematics of possible issues of probe coverage with both chemistries.

Figure 7.14 shows schematics that describe the capture issues we have encountered with both functionalization chemistries. As shown in the top view of a single pixel in figure 7.14(a), the chip is covered by a thick dielectric layer ($\sim 1\ \mu$m). On top of each FET, a 1 μm$\times$ 1 μm window is etched-back to release the device. Over a large region on the chip, this creates a periodic array of 1 μm wide and 1 μm deep trenches of 6.5 μm pitch. Based on the results of repeatable probe detection with the APDMES/flat chemistry, we believe that the probe molecules could be condensing into a multilayer stack (possibly because of the heating step) within the device trench as shown in figure 7.14(b). As a result, the target strand that would only hybridize with the topmost layer could be too far away from the device that its charge may not be visible at all. A stack of as few as 4 layers of the probe will exceed λ_D; therefore although we could distinctively

sense the probes in that configuration, the effect of the target molecules was not electrically apparent.

In the case of GPDMES/upright chemistry, we suspect that the wettability of the microtextured chip surface could have caused problems with probe functionalization. Unlike an APDMES/HfO_2 surface that is fairly hydrophilic (contact angle$\sim 45^\circ$), the GPDMES/HfO_2 surface (contact angle$\geq 70^\circ$) is not so wettable [118]. In combination with the surface topography, the apparent contact angle could have exceeded 90° and rendered it hydrophobic. That could have easily meant that a microdroplet beaded up on the chip, contacted the top surface and was pinned at the edges of device windows. Given that the sub-nL microdroplet was very light, its self-weight could not have competed against the repulsion so, air could have been trapped between the pixels and the droplet. That explains the relative difficulty we encountered with spotting the droplets in this case. Since the microdroplet did not wet the surfaces inside the pixel windows, the probes would not have contacted the device surface at all, rather they would have only deposited on the surrounding areas on top of the dielectric.

For the optical portion of these experiments, the measurement was based on the entire footprint of the droplet on the chip surface. Note that the optical measurement cannot delineate any effects due to the depth of the imaging surface. Therefore, a single layer or multilayers would not have been distinguishable based on the fluorescent response of the topmost layer of probe or the hybridized target strands. This explains why, even when we had too many layers of probes stacked, the hybridization and its optical response was always observable. Next, the optical measurement also does not have good selectivity between the device region and the remainder of the chip surface under the spotted area. The measurement was an average of the entire area under the droplet footprint. Therefore, even if molecules were not hybridized inside the pixel trench, that would have only been a tiny area fraction of the rest of the spot. The rest of the dielectric surface, whose area was much greater, contributed to a positive optical signal. Although both the methods of functionalization are based on known protocols, the fact that an actual device has its surface factors at play against ideal flat surfaces that are normally studied lends some complexity to this problem that need to be separately addressed.

7.5 Analysis of diffusion limits

The experiments described in section 7.3 were all limited by the amount of probe molecules captured on the surface. An analysis of the diffusion limitation can hold clues to understand this scenario better for a workaround. Nair and Alam [63] have provided an analytical framework that describes the diffusion-limitations for field-effect sensors. Using their model, we can calculate settling times as a function of probe

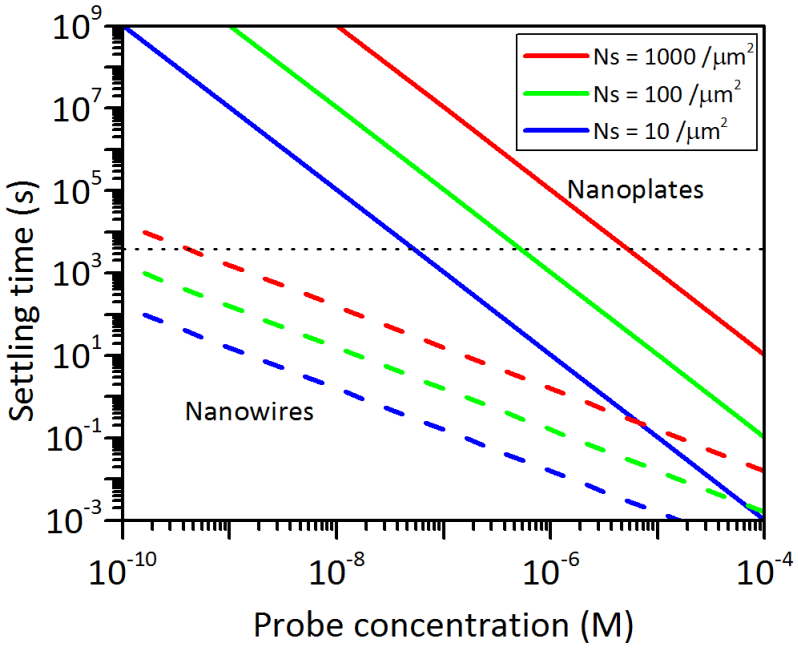

Figure 7.15: Settling time v/s probe concentration for conjugation of probe with SAM functional layer on chip based on a diffusion-limited surface absorption model. The dotted line indicates the cut-off time for probe deposition in our experiments.

concentration. In figure 7.15, we have plotted the settling time v/s probe concentration for a range of surface densities (10-1000 μm^{-2}). In these calculations, we used a molecular diffusivity of 5×10^{-6} /(bp)$^{0.72}$ cm^2/s. The FETs used in our experiments are similar in dimensionality to the nanoplate devices. The calculations show that molecular settling times on a surface increase exponentially with every decade of decrease in concentration. The dotted horizontal line shows the probe incubation time during our experiments. This was constrained in order to prevent evaporation and complete drying of the spots on the chip. Therefore, in the range of surface densities shown, only the 50μM and 10μM titers would have incubated long enough during our experiments to be detectable. This is reflected in our results as well. The 1μM concentration being borderline (depending on surface density), it was also optically detectable only in some cases. We can infer that in the 0.1μM and lower concentrations, the probes would have certainly not diffused long enough for sufficient capture and coverage and this was considtently reflected in all our experiments. Although dilution of probes appears as a way of achieving better monolayer control, the trade-off between settling time and low incubation time can adversely affect the amount of probe functionalization. It may therefore be necessary to address the wettability of the GPDMES surface or multilayer formation with APDMES chemistry while still retaining a high probe spot concentration (>1μM).

Chapter 8

Out-of-plane hierarchical nanostructures in silicon substrates for superhydrophobic applications

A portion of the research leading to this dissertation has also included work on novel micro/nanofabricated structures to create nanostructured surfaces with an increased geometrical complexity and hierarchy of lengthscales in silicon substrates. In this chapter, we discuss a classic miniaturization problem—that of wettability and engineering of superhydrophobic surfaces. It has long since been established that microstructuring the topology of a surface can be an effective method of reducing the contact area with liquids, thereby increasing the contact angle so that, in the extreme, hydrophobicity can be realized. We demonstrate an inexpensive and highly scalable approach of fabricating re-entrant microstructures, with 3-dimensional hierarchical nanostructures as well, so as to achieve superhydrophobicity with extremely low hysteresis[1].

8.1 The need for superhydrophobic structures

Superhydrophobic surfaces are usually characterized by their tendency to repel water, with static contact angles (CAs) with water higher than 150° [121, 122]. This tendency, famously inspired from naturally occuring examples such as the lotus-leaf effect the taro plant and parrot feather plant, finds numerous applications in the areas of self-cleaning [123, 124], liquid motion sensing [125], anti-fouling [126], anti-freezing [127] and heat transfer enhancement [128]. The ability to engineer and control portions of a surface with different wettability has spawned a new area of research using surface-tension controlled microfluidics [123]. It has been shown that surfaces with hierarchical micro/nano structures are efficient at reducing the actual contact area between the solid surface and the liquid droplet, thus increasing the contact angle and decreasing the sliding angle [129]. A quantitative measure of the hydrophobicity of a micropatterned surface is its apparent CA as determined by the Cassie-Baxter equation [130, 131].

$$\cos\theta^* = f\,(1 + \cos\theta_y) - 1 \tag{8.1}$$

where, θ^* is the apparent CA. θ_y is the equilibrium Young's contact angle, and f is the area fraction of

[1] Results discussed in this chapter are published in [119] & [120]. Reproduced with permissions from IEEE and IOP.

the solid surface in contact with the liquid. To increase the equilibrium CA, the two factors, f and θ_y can be tuned. Area fraction, f, can be reduced by generating surface roughness and θ_y increased by adding a hydrophobic coating such as Teflon®. In our testing specimens, we used Teflon®-like fluoropolymer as the coating material [132], composed of C_4F_8 deposits derived from the DRIE process.

8.1.1 Hierarchical micro/nanostructures in the literature

Till date, there have been several demonstrations of creating hierarchical micro/nano surfaces, some of which include electron beam lithography [133], replicate molding [134, 135], plasma etching [129], nanopillar or nanowire formation [136], self-assembly [137] and shift patterning [138]. In the last decade, a novel method of nanofabricating sturctures in crystalline silicon has emerged through a process called metal-assisted chemical etching (MACEtch) [139, 140, 141], and some of the primary demonstrations of this method have been in fabricating hydrophobic surfaces. Most of these demonstrations of hierarchical micro/nano surfaces are usually composed of simple microstructures such as micropillars or microspheres. Recent studies show that re-entrant or micro-hoodoo structures are capable of preventing liquid from falling into the gaps between the micropillars, thus reducing the contact area between an droplet and the micropillar [142]. Another hypothesis suggests that a combination of both hierarchical structures and the re-entrant shape might further increase superhydrophobicity and reduce hysteresis[142, 141]. However, combining both features into one substrate poses a practical microfabrication challenge.

8.2 A one-mask process to create re-entrant and hierarchical surfaces with extreme hydrophobicity

In our attempts, we have developed a simple one-mask pattern transfer and combinations of etching steps produce the complex multi-scale as well as 3D re-entrant geometries in silicon substrates. Re-entrant microstructures were fabricated via a customized microfabrication process based on a combination of both anisotropic and isotropic dry etching steps, while silicon nanopillars were created on the resulting microstructures by using the MACEtch. Sidewall sub-micron features such as scallops from deep reactive ion etching (DRIE) interfere with nanopillar formation. In order to facilitate MACEtch on both top and sidewall of silicon microstructures, we have developed a method to smooth the sidewall sub-micron roughness. During the process development, we have also analyzed certain geometric aspects of the microstructure design and crystal planes that are at play and have a bearing on how the nanopillars evolve into the sidewalls. Results from droplet wetting experiments of the fabricated structures indicate that employing a re-entrant microstructure

with a hierarchical nanofeatures on the surface is a promising path to achieve superhydrophobicity with extremely low hysteresis.

8.3 Experimental

8.3.1 Microfabrication

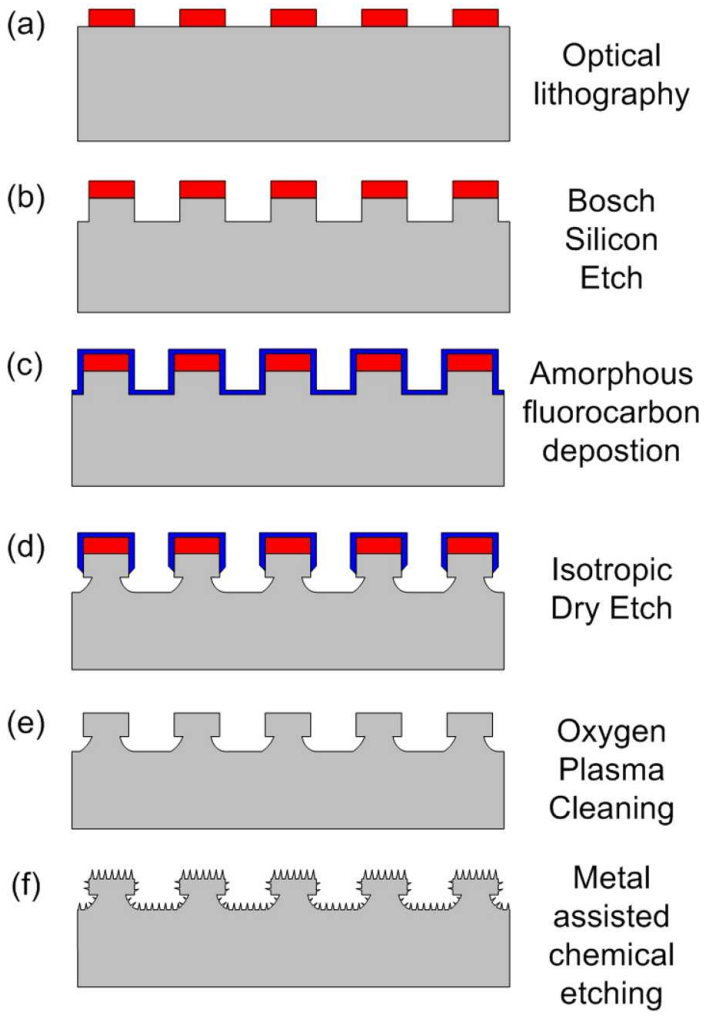

Figure 8.1: Fabrication flow illustrating major processes of realizing the micro/nano hierarchical structure.[2]

Figure 8.1 shows the major steps involved in the fabrication of hierarchical micro/nanostructures with re-entrant shape. An array of 4 μm tall micropillars was patterned on a p-type $\langle 100 \rangle$ silicon substrate using conventional photolithography (step a), followed by DRIE (step b). After these steps, a 100 nm

[2]Reproduced from [120], with permission from IOP.

thick amorphous fluorocarbon (C_4F_8) film [143] was deposited everywhere on the sample surfaces (step c). SF_6 plasma Reactive Ion Etching (RIE) was used to isotropically etch the sample. First, the amorphous fluorocarbon film on the bottom of the substrate was removed with the help of physical bombardment, but that still left the fluorocarbon film on the micropillar sidewalls intact. Then, silicon exposed at the bottom of the substrate was etched by the SF_6 plasma isotropically to form re-entrant microstructures due to undercutting (step d) while the fluorocarbon film protected the sidewalls of the silicon micropillars from any further etching. Tuning the fluorocarbon film thickness works as a way to adjust the crown of the re-entrant microstructure. The fluorocarbon film was then removed by a two-step process: an initial 20 min Piranha cleaning step, followed by a 20 min ashing process in oxygen plasma (step e). Surface oxides formed during cleaning processes were etched away in buffered hydrofluoric acid (BHF). After cleaning, nanopillars were created everywhere on the surface (step f) using MACEtch [109]. Finally, a 20 nm thick amorphous fluorocarbon film was coated on the surface to decrease surface energy for improved water repulsion (step g).

8.3.2 Metal assisted chemical etching of silicon

In order to create nanopillars of silicon in the substrate, we chose the MACEtch process which has gained considerable attention over the last decade [109, 144, 145, 146] because of its simplicity and inherently self-limited process kinetics. Electroless plating with solutions composed of HF and noble metal ions is, simultaneously, a metal-assisted chemical etching process. Dendrite structures of the deposited metal are formed when a Si substrate is immersed in a solution containing HF and M^{n+} ions (M = Ag or Au), in addition to the etching of the silicon substrate. At the interface of the dendritic deposit and the silicon surface, a spontaneous galvanic cell (equations 8.2) is established because the electrochemical potential of Ag^+/Ag is greater than the Fermi energy of Si [144]. Therefore, holes are injected into the valence band of Si from Ag^+ which reduce to elemental Ag forming nuclei. With increasing etch time, these Ag nuclei grow in size into dendritic particles. Simultaneously, the holes injected into the valence band of Si enable local oxidation and dissolution of Si atoms underneath the Ag deposits. As the Si dissolves during the etch, the Ag/Si interface sinks deeper into the Si substrate [147]. The charge transfer is preferentially localized at the redox interface and hence no new Ag nuclei emerge on the sidewalls of etched features. Some demonstrations have also shown that by varying the concentration of $AgNO_3$ and HF, the diameter of resulting Si nanowires can be tuned [147].

$$Ag^+ + e^- \longrightarrow Ag \qquad \| E^0\left(Ag^+/Ag\right) = 0.779\,V \tag{8.2a}$$

$$Si + 6F^- \longrightarrow SiF_6^{2-} + 4e^- \qquad \| E^0\left(Si^{4+}/Si\right) = -1.24\,V \tag{8.2b}$$

$$4Ag^+_{(aq)} + Si_{(s)} + 6F^-_{(aq)} \longrightarrow 4Ag_{(s)} + SiF_{6\,(aq)}^{2-} \tag{8.2c}$$

The MACEtch used in our experiments consisted of three stages. The first stage was that of sample preparation in which the scallops on the sidewall of the silicon micropillars formed during the DRIE process were removed. The sample was oxidized in a tube furnace at 1100°C for 110 min to a known thickness (∼150 nm) greater than the depth of DRIE sidewall scallops. Then the silicon oxide was etched away in BHF to free the micropillar surfaces from any roughness. The second stage was the actual MACEtch in which silicon nanopillars were synthesized by electroless etching in a solution of Ag^+ ions (20mM) in HF (5M) for ca. 2 min, as shown in figure 8.1 (step f) [109]. After synthesis, the third and final stage was that of cleaning the sample in conc. HNO_3 to etch away silver dendrites and reveal silicon nanopillars on the top as well as on the sidewall of the microstructures.

8.3.3 Process optimization for sidewall nanopillars on patterned structures

In order to ensure good quality nanopillar formation on silicon microstructures, both for uniformity of depth and dense coverage over the area, it is very important to have optimized MACEtch conditions. The surface roughness and morphology of the underlying microstructures are crucial in seeding silver dendrites that lead to formation of silicon nanopillars in the Ag^+/HF etching system [129, 141]. To study the effect of surface roughness on MACEtch, we prepared two microstructures of the same shape but different sidewall roughness. Both were cylindrical micropillar arrays of 100 μm diameter and 150 μm equitriangular pitch. Sample A was patterned through photolithography, followed by a conventional 2 μm/min etch rate DRIE process in a Plasmatherm ICP-DRIE system. Sample B was fabricated through the same optical pattern transfer, but etched at a much faster rate (20 μm/min) in a STS Pegasus ICP-DRIE system. Both samples were subjected to the same cleaning and sidewall smoothing steps described above. Finally, MACEtch was performed to yield about 1 μm tall nanopillars.

Figure 8.2 shows SEM images of the corresponding specimens after subsequent cleaning, sidewall treatment, and nanopillar MACEtch as outlined above. As shown in figure 8.2(a), the short thermal oxidation/etch treatment effectively smoothed the 110 nm deep scallops formed during 2 μm/min DRIE and silicon nanopillars were observed on the sidewalls. However, as seen in figure 8.2(b), the scallops formed

during 20 μm/min DRIE were much deeper (ca. 550 nm). They prevailed even after the sidewall treatment and, eventually, the MACEtch only caused further roughening but no nanopillar formation. We believe that during MACEtch, the Ag-Si redox cells that were seeded on the rough surface ended up etching into each other. This artifact only caused nano-roughness and the process failed to propagate towards yielding nanopillars. Hence, a smooth surface and a sidewall treatment step were essential for controlled seeding of the silver dendrites that etched nanopillars laterally on the sidewalls of patterned microstructures.

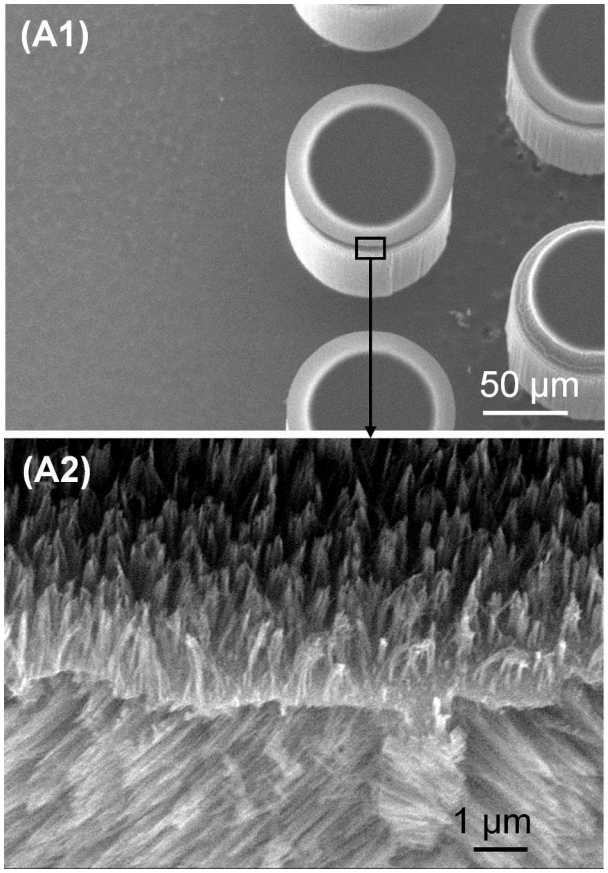

(a) SEMs of SiNP formation on Si micropillars etched in a 2 μm/min DRIE

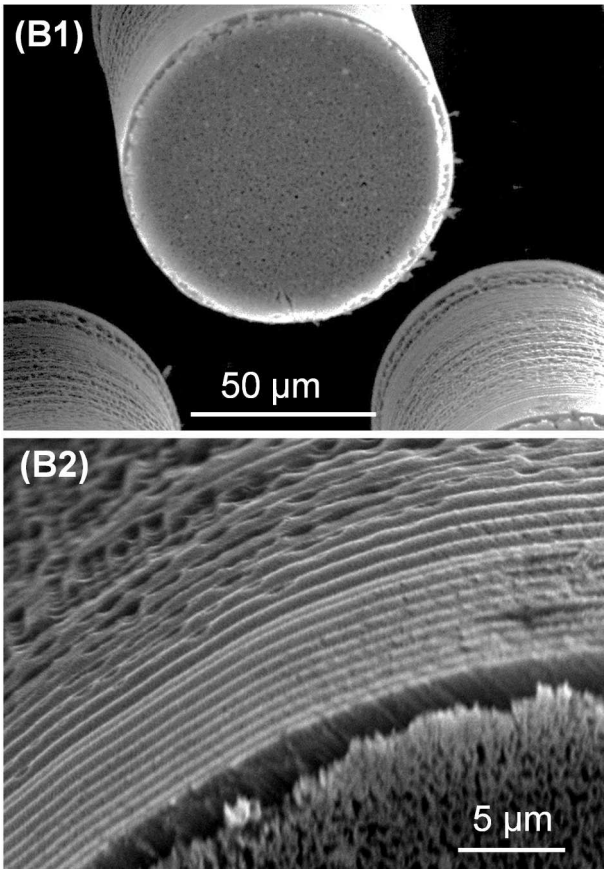

(b) SEMs of SiNP formation on Si micropillars etched in a 20 μm/min DRIE

Figure 8.2: Effect of DRIE scallops (based on DRIE etch rates) on SiNP formation. In each case, the top panel shows before and the bottom panel shows after MACEtch.[3]

8.3.4 Effect of microstructure shape on SiNP formation

To investigate the effect of silicon microstructure shapes on nanopillar formation, we prepared three microstructures of circular, triangular and hexagonal shapes respectively from ⟨100⟩ silicon substrates. All

[3]Reproduced from [119] & [120], with permission from IEEE and IOP.

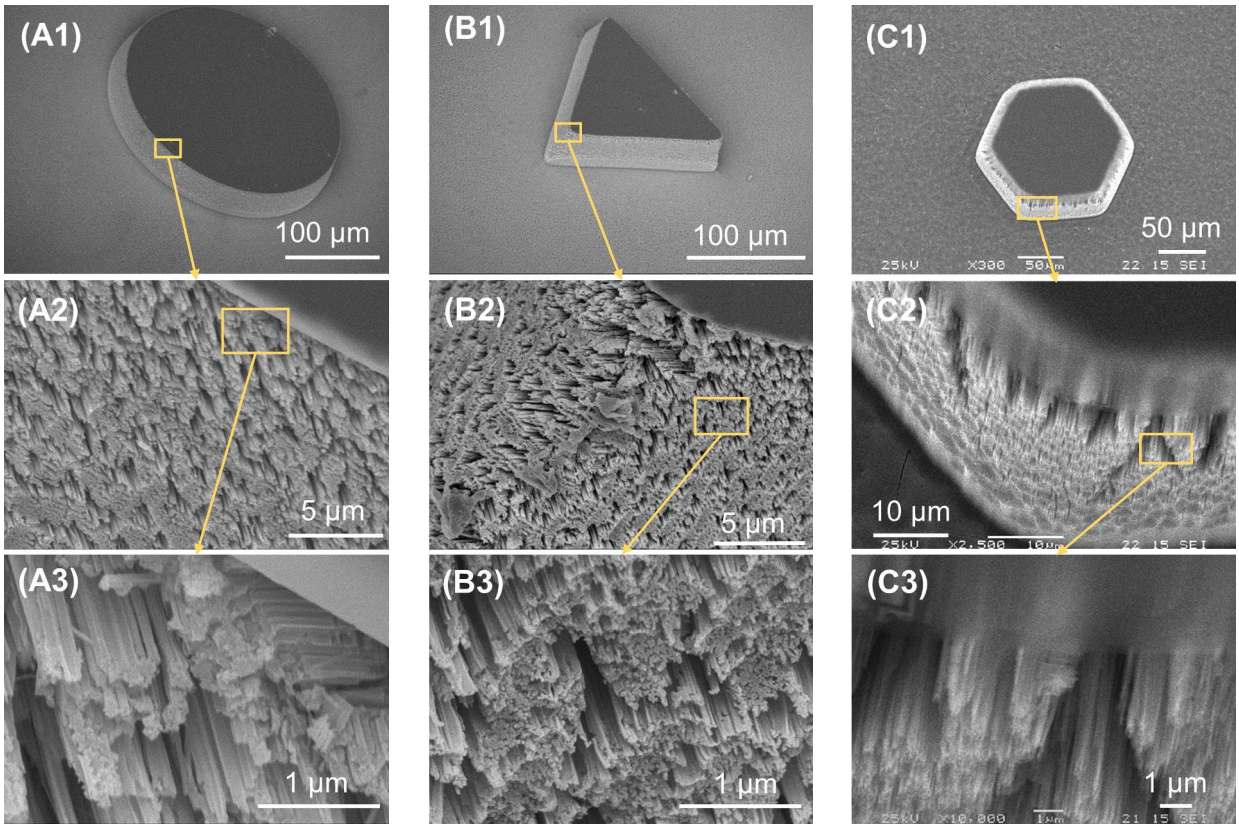

(a) SEMs of SiNP formation on cylindrical Si microposts

(b) SEMs of SiNP formation on triangular Si microposts

(c) SEMs of SiNP formation on hexagonal Si microposts

Figure 8.3: Effect of underlying microstructure shape on evolution and orientation of MACEtched SiNPs.[4]

three microstructures were patterned through photolithography and 2 μm/min DRIE, and MACEtched ($\geq$5 min) to yield tall SiNPs on the sidewalls. In all three cases, the same cleaning and surface treatments as outlined in sections 8.3.1 and 8.3.2 were used to prepare the sidewalls for nanopillar formation. A thin LPCVD Si_3N_4 film, compatible with the rest of the fabrication process, served as an etch mask to prevent nanopillar formation on the top surface of the microstructures. Figure 8.3 shows the SEM images of the three microstructures with nanopillars on the sidewalls (A, B, C). A majority of nanopillars followed $\langle 100 \rangle$ planes, which agreed with reports on nanopillar directionality [129, 144]. We observed further that, regardless of the sidewall orientation with respect to the wafer flat: either 30° or 60° in the case of triangles and hexagons and a continuous change from -90° to +90° for the circular post, nanopillars evolved by etching into the nearest $\langle 100 \rangle$ plane. In all three cases, we were able to obtain uniform size and coverage of nanopillar bundles (A3, B3 & C3). As shown in figure 8.3(b) (B2), nanopillars were oriented along multiple orthogonal $\langle 100 \rangle$ planes near the edge features. In figure 8.2(a) (A2), nanopillars were oriented along multiple orthogonal

[4]Reproduced from [119] & [120], with permission from IEEE and IOP.

⟨100⟩ planes where the tangential direction of curved surface was at 45° with respect to the ⟨100⟩ reference directions in the case of circular geometry. Along sharp vertical edge lines, notably in the case of the vertices of the triangular microstructure (B2), the Ag-Si redox couples from orthogonal intersecting planes etched into each other and only caused irregular nanoscale roughness. Regardless of the microstructure shape, the nanopillar MACEtch followed well-defined directionality with respect to the crystal planes in the substrate.

8.3.5 Microfabricated re-entrant and hierarchical micro/nano-structures

Figures 8.4(a) and 8.4(b) show two re-entrant silicon microstructures (M1 and M2) from the above described fabrication process (figure 8.3.1(steps a-e)). Sample M1 was etched in SF_6 RIE for 1 min. Sample M2 was etched in SF_6 RIE for 2 min, thus resulting in a deeper undercut and thinning down of top crown of the micro re-entrant structures. Measured design parameters for the microstructures are summarized in Table 8.1[5]. The hierarchical micro/nano structures (H1 and H2) were fabricated using the modifications in steps (f) and (g) of the fabrication process. Both samples went through 2 min of electroless etching in MACEtch. Sample H1 corresponds to the hierarchical structure derived from microstructured sample M1 and sample H2 from M2. In each subfigure, insets on the top right are magnified views of the micropillar before and after the MACEtch. Insets on the bottom right show zoomed-in images of silicon nanopillars both on the top and sidewalls of the re-entrant microstructures. By incorporating the two-step anisotropic/isotropic etching strategy and optimizations to the MACEtch, we were able to obtain 3D re-entrant microstructures with nanopillars that had complete top and sidewall coverage over the entire profile. The relative ease and scalability of this fabrication approach arises from the fact that the entire sequence involved only a single optical alignment/pattern transfer step at the beginning. All subsequent steps are based on conventional MEMS etch schemes and, ultimately, the self-aligned formation of nanopillars with respect to the crystal orientation. Figure 8.4(c) shows the SEM images of straight silicon micropillars and the corresponding hierarchical micro/nanostructure after adding nanopillars on top the surface of micropillars using MACEtch.

Design	Top crown width (μm)	Pitch size (μm)	f derived from SEM image	f derived from measured CA
Sample A	5.9	14	0.18	0.14
Sample B	3.5	14	0.04	0.06

Table 8.1: Geometric parameters (as fabricated) for the re-entrant/hierarchical microstructures.

[5]Reproduced from [120], with permission from IOP.

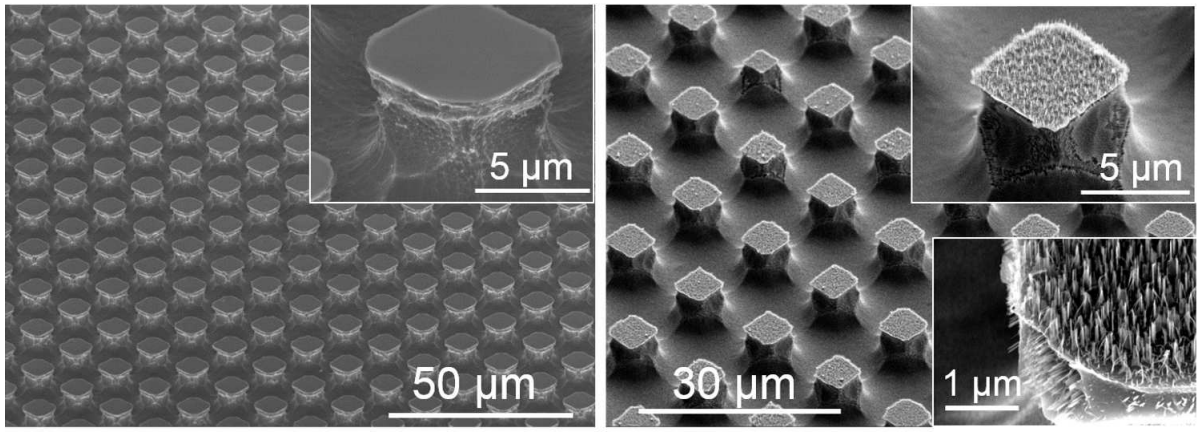

(a) Re-entrant microstructure (M1) before (left), and hierarchical (H1) after (right) SiNP formation

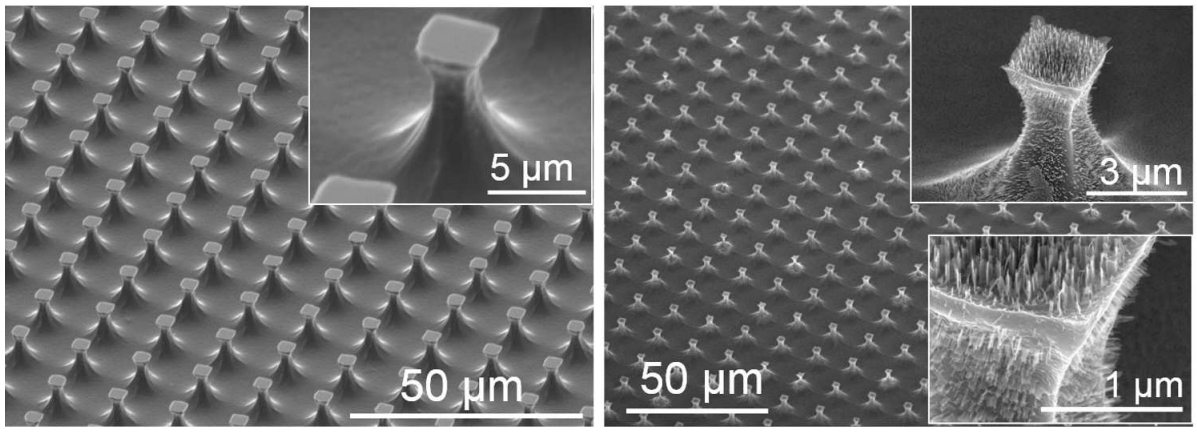

(b) Re-entrant microstructure (M2) before (left), and hierarchical (H2) after (right) SiNP formation

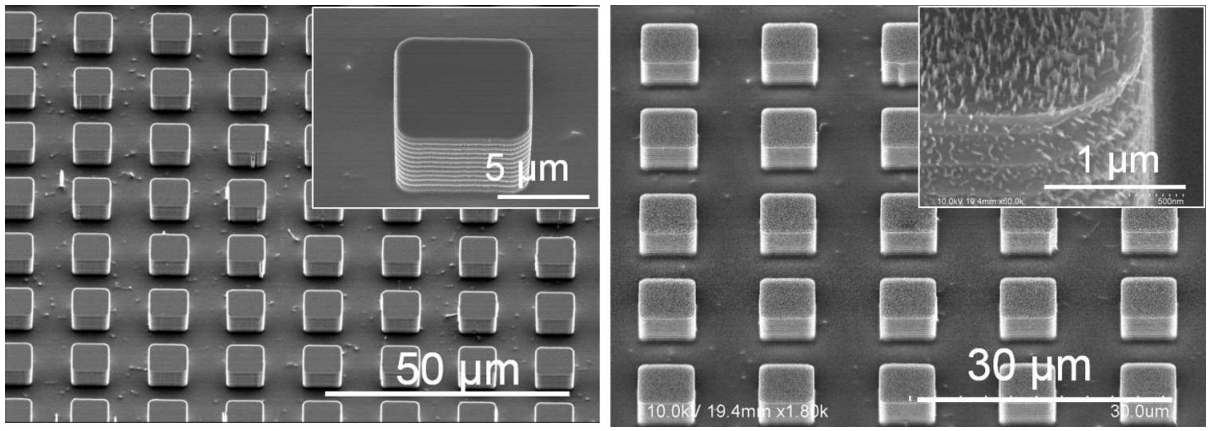

(c) Regular micropillars before (left), and hierarchical (H3) after (right) SiNP formation

Figure 8.4: SEM images of the different microstructure arrays, and corresponding hierarchical micro/nano structures created by MACEtch. Nanopillars on top and sidewalls of a re-entrant structure are shown in the insets.[6]

[6]Reproduced from [120], with permission from IOP.

8.4 Wettability tests

8.4.1 Measurement technique

In order to characterize individual contributions from the re-entrant profile as well as the multi-scale structural hierarchy to superhydrophobicity, we measured the CA of water as well as sliding angle on three sets of samples. The first set of samples had the complete 3-D hybrid structure consisting of both the re-entrant profile micropillars and nanopillars etched on their top/sidewall surfaces. The second set consisted of re-entrant profile micropillars only. The third set consisted of hierarchical structure with straight micropillars instead of re-entrant micropillars. Other control specimens included a smooth flat silicon surface as well as a flat specimen with only nanostructures fabricated using 2 min MACEtch. All samples were coated with 20 nm thick amorphous fluorocarbon film. The apparent static CA was measured using a CAM 200 goniometer (KSV Instruments Ltd., Helsinki, Finland). The sliding angle for the droplet, which is defined as the tilting angle of the surface with respect to the horizontal when the liquid droplet begins to move, was simulated and measured using a precise tilting stage.

8.4.2 Contact angle data

Figure 8.5 shows water CA measured on four types of surfaces and plotted on the theoretical Cassie state curve. The four types of surfaces are: a) smooth surface, b) pure nanostructured (flat) surface, c) pure re-entrant microstructure and d) re-entrant as well as hierarchical micro/nano structured surface. For a smooth surface, $f \longrightarrow 1$, so the apparent CA is the same as the equilibrium CA of water on fluorocarbon film surface, which is measured to be 117°. Pure nanostructured surface has a CA of 142° and hence, according to equation 8.1, $f = 0.39$. Microstructured sample M1 has a CA of 158°, corresponding to a value of $f = 0.14$, which is close to the f-value derived from the SEM images shown in figure 8.4. Since the crown-width of the re-entrant micropillar is 5.9μm while the pillar-to-pillar pitch is 14 μm, the area fraction is calculated to be 0.18. Table 8.1 also summarizes f-values estimated from both SEM images and the CA measurements. The micro/nano hierarchical structure sample H1 has a CA of 165° and the theoretical area fraction is 0.07, which is close to the product of f of microstructure ($f = 0.18$) and that of the nanostructure ($f = 0.39$). This indicates that a water droplet contacts the micro/nano hierarchical structure in full Cassie state. The same trend also follows in the case of micro/nano hierarchical structure H2. Sample H2 has a smaller area fraction, leading to a CA of 171°, which is larger than that of H1. The results proved that hierarchical structure increases the CA by decreasing the contact area between liquid and the top part of the solid surface.

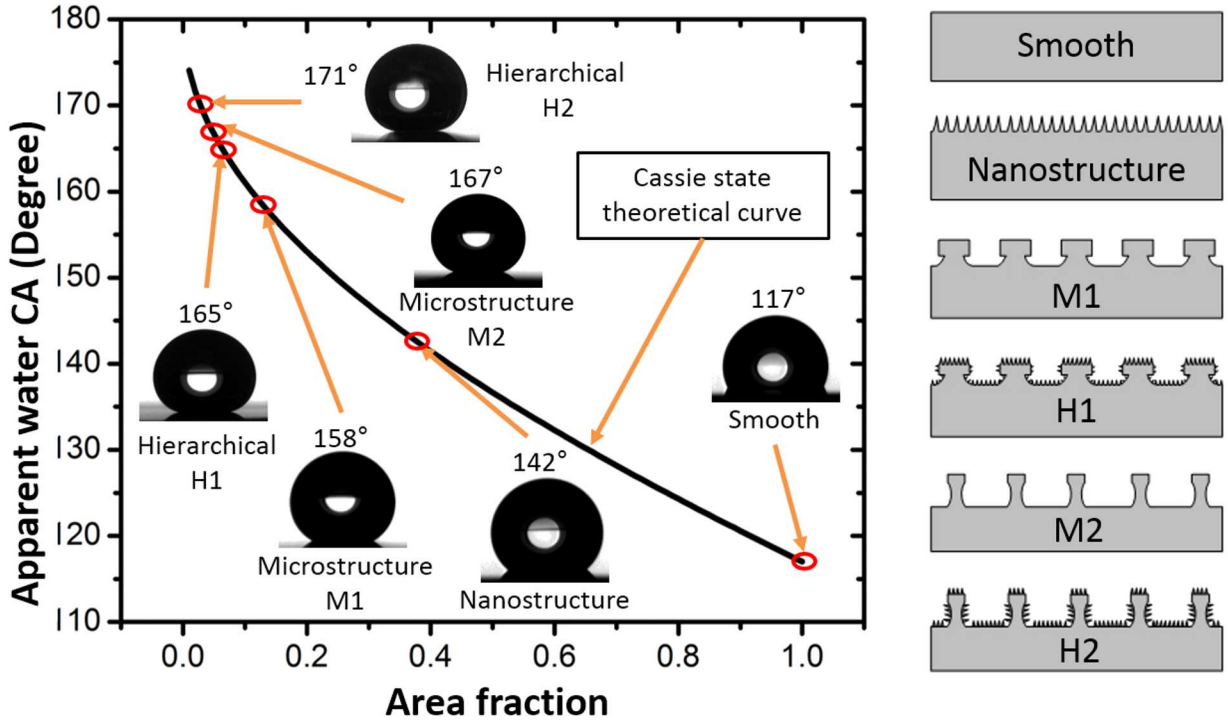

Figure 8.5: Measured CA of water on four surfaces compared with the theoretical Cassie state curve. Actual snapshots of a water droplet contacting the specimen are shown as insets within the plot, and schematics of the profile and structural hierarchy are shown on the right.[7]

Surface types	CA of water (°)	Sliding angle of water (°)	CA of glycerol (°)	Sliding angle of glycerol (°)
Micro re-entrant 1 (M1)	158 ± 2	15 ± 0.2	162 ± 2	28 ± 0.2
Re-entrant and hierarchical (H1)	165 ± 1	2.0 ± 0.2	164 ± 2	4.6 ± 0.2
Micro re-entrant 2 (M2)	167 ± 1	6.5 ± 0.2	161 ± 2	6.6 ± 0.2
Re-entrant and hierarchical (H2)	171 ± 1	0.5 ± 0.2	164 ± 2	2.2 ± 0.2
Micropillar and hierarchical (H3)	166 ± 4	9.6 ± 0.2	159 ± 4	19.6 ± 0.2

Table 8.2: Contact angles and sliding angles measured for water and glycerol.

Table 8.2[8] summarizes water CAs and sliding angles of water and glycerol on three different sets of samples. The first set of samples M1 and M2 have only micro re-entrant structures. The second set of samples H1 and H2 have both micro re-entrant structures similar as M1 and M2 but also have nanopillars on

[7,8]Reproduced from [120], with permission from IOP.

the top and sidewalls. Sliding angles for water droplets on M1 and M2 measure at 15° and 6.5° respectively. After creating nanopillars on the surface, these sliding angles of H1 and H2 drop to as low as 2° and 0.5° respectively. The third sample, H3, has silicon nanowires on straight micropillars with the same pitch and similar pillar size as H1, and the nanopillars were synthesized through MACEtch in the same way but without the prior isotropic RIE modification for the re-entrant profile. As shown in table 8.2, this structure exhibits similar CA but much higher sliding angle 9.6°. The same trend also exists for glycerol. H1 has a sliding angle of 4.6°, much lower than the sliding angle of glycerol on M1 (28°) and sliding angle of glycerol on H3 (19.6°).

8.4.3 Contact angle hysteresis

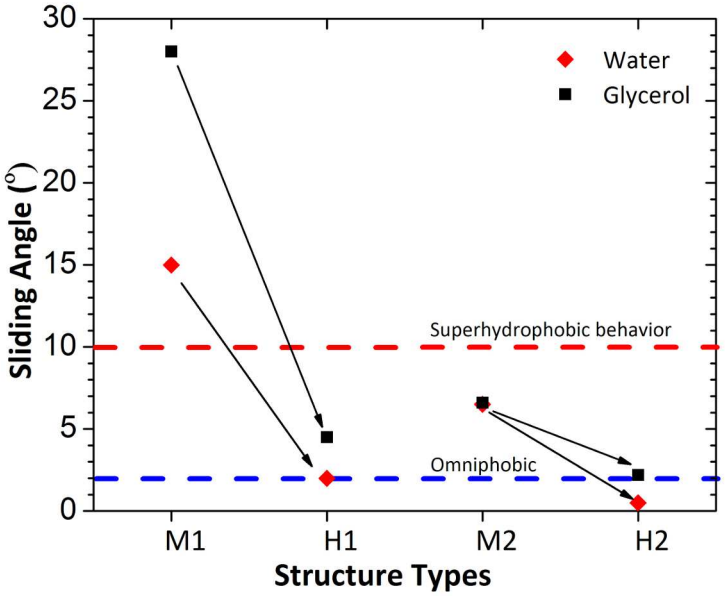

Figure 8.6: Measured sliding angles for roll-off of water/glycerol on the four re-rentrant/re-entrant and hierarchical surfaces.

Figure 8.7 shows a series of snapshots, each at 33 ms time intervals, which recorded a 20 μL water droplet coming in contact with the surface of a H2 sample tilted at an angle of 1° from the horizontal. Since the adhesion force between the sample surface and water droplet was very small, a droplet that was smaller than 20 μL could not be released from the pipette easily. Therefore, a 20 μL water droplet was used and gravity facilitated the release of the water droplet from the pipette to the sample surface. Under these conditions, the surface was found to be extremely hydrophobic and the droplet, upon release, rapidly rolled off the surface. The reason for this extremely low contact angle hysteresis may be attributed to the combined effect

of both shape and hierarchy in the reduction of actual contact area between the liquid droplet and solid structure. A hierarchical structure, or adding nanopillars on top of micropillars in our case, caused the water droplet to come in contact with much smaller area on the top surface of the substrate. Thus adhesion between the liquid and solid surface decreased, resulting in reduced hysteresis.

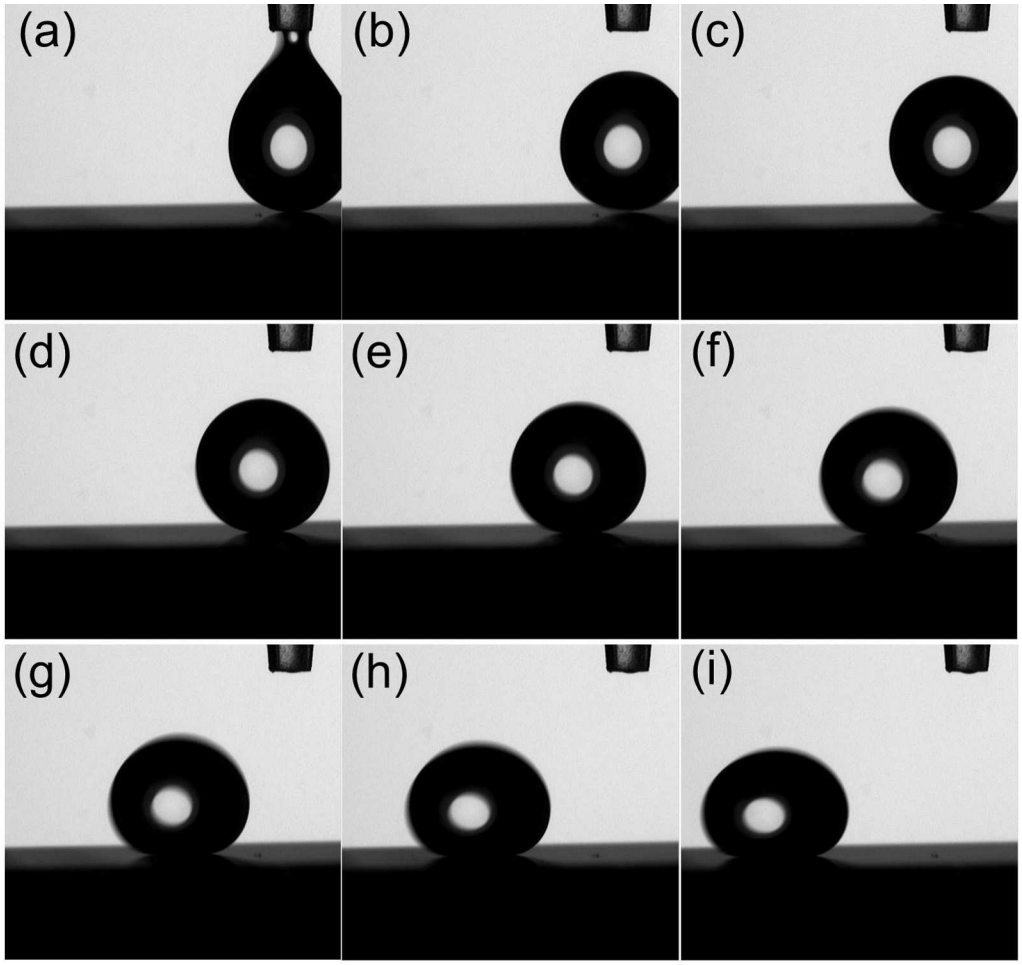

Figure 8.7: A series of photographs showing a water droplet rolling along the H2 surface oriented at a tilt angle of 1° from the horizontal. The time interval between each snapshot was 33 ms.[9]

Our measurements have indicated that surfaces incorporating both hierarchical features and micro re-entrant structures exhibit much lower sliding angle than structures incorporating only hierarchical or only micro re-entrant scheme. Figure 8.8 shows a schematic cartoon of how the microprofile and hierarchical nanostructure modifications progressively increase the hydrophobicity of the surface. The hierarchical nanopillars work by decreasing the surface area in contact with the droplet so that (as seen in equation 8.1) the apparent CA increases by virtue of f. In the case of re-entrant structures (M1 & M2), their adverse

[9]Reproduced from [120], with permission from IOP.

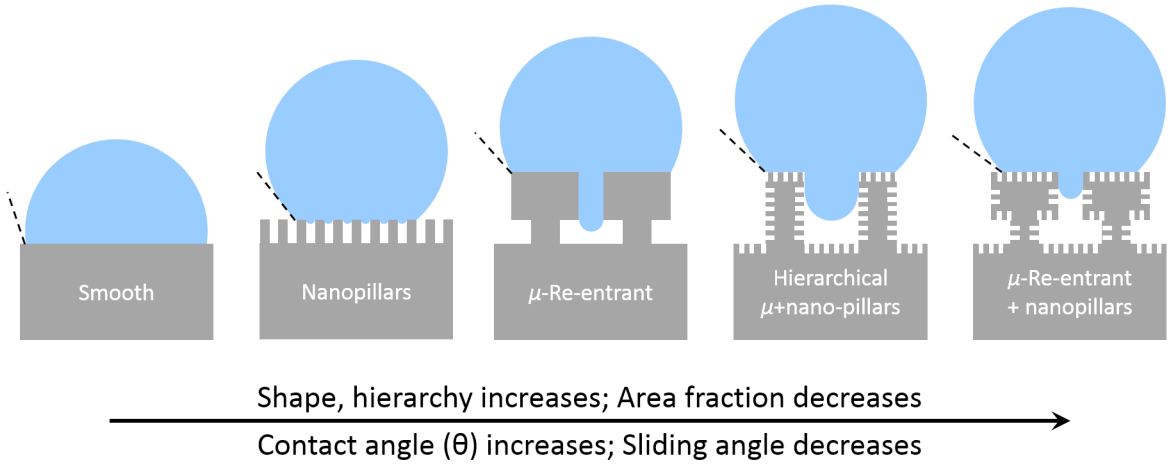

Figure 8.8: Schematic describing the evolution of increasing hydrophobicity with profile and hierarchical modifications to the microstructures.

curvature opposes the extension of the liquid-solid interface below the crown which helps to prevent the water droplet from falling into the gap between pillars, therefore reducing the liquid contact with the sidewalls of the pillars. The combination of straight micropillars with nanopillars (H3) can help by further reducing the f-value, although this structure does not prevent the water droplet from penetrating into the gap. The water droplet partially wets the micropillars but sits on top of the nanopillars, exhibiting the so-called partial Wenzel and partial Cassie state observed on hierarchical structures by many researchers [148, 149, 150, 151]. However, it is the combined effect of re-entrant pillars with thick crown (H1 & H2) that can both minimize the contact area as well as prevent the water droplet from contacting with the sidewalls of the pillars. Thus the hysteresis is minimized to $\leq 2°$, which is in the range of typical omniphobic surfaces, and any droplet placed on such a surface will roll-off with the slightest tilt or mechanical perturbation. The resulting 3-D re-entrant and hierarchically structured surface exhibits superhydrophobicity with a water CA of 171° and a sliding angle of 0.5°.

8.5 Summary

Experimental results show that it is absolutely essential to incorporate a combination of both strategies to minimize the contact between the liquid and solid structure in order to achieve optimal superhydrophobicity with extremely low sliding angles. Synthesizing complex 3D hierarchical structures through polymer coatings and surface modifications is not easy, and there have been several previous attempts to adapt these techniques for making superhydrophobic surfaces to obtain re-entrant structures for making superhydrophobic surfaces.

So far there have been some reports of fabricating re-entrant structures in the literature through XeF_2 etching of silicon using silicon oxide mask, electrospinning [142] and 3D diffuser lithography [149]. These fabrication methods, however, are not readily compatible for incorporating hierarchical schemes. For example, Tuteja et al. [142] reported re-entrant structures with silicon oxide on top; but adding nanostructures on both silicon oxide and the silicon surfaces at the same time is not easy. Our approach provides a straightforward one-mask lithographic scheme to realize monolithic structures of both re-entrant sidewall profiles and multi-scale hierarchy in bulk silicon substrates. Moreover, processes for making re-entrant microstructures are a simple combination of anisotropic and isotropic dry etching steps that can be performed in any standard ICP-RIE silicon etching system. The top-down fabrication of all-silicon re-entrant microstructures, which facilitates the fabrication of silicon nanowires using MACEtch, enables an easily scalable manufacturing scheme that can prove extremely cost-effective.

Chapter 9

Conclusions

The underlying theme of this thesis has been to explore pathways to enhance the electrostatic effects in microfluidic systems. Given that surface charges of nanoparticles are shielded and separation forces scale unfavorably below the sub-micron regime, colloidal nanoparticle foulants or biological species such as viruses, subcellular components and macromolecules will benefit from an efficient way to sustain stronger separation fields. Although field-effect biosensors, by virtue of the scalability of semiconductor electronics, hold tremendous promise for label-free sensing systems, we need to overcome the fundamental issue caused by ionic shielding in order to realize their full capability of biosensing from physiological samples.

9.1 The separation problem

Dielectrophoretic capture of particles is strongly dependent on the relative polarizability of the particles, as well as the scaling of electric fields relative to the particle size and characteristic microfluidic dimensions. Capture schemes will need enhanced electric fields that can be implemented through multiple interdigitated microelectrode arrays. At the same time, combining a high frequency AC depolarization with transverse DC bias across the separation zone enhances the forces of separation acting on the particles. Our results have indicated that the mixed biasing scheme provides the ability to sustain stronger electric fields in bulk to improve the capture of sub-micron colloidal particles that are normally less affected by electrostatic separation forces. In our experiments, we have predicted and observed a reversal of the effect of depolarization on the outcome of separation. In low salt, we were able to depolarize at lower AC cycling frequency for improved collection of the colloids at the electrodes over conventional DEP. However, the high salt medium needed much higher AC depolarization frequency to sustain the electric fields in solution, and particles were also repelled away from the electrode arrays because of nDEP. On one hand, miniaturizing the electrode geometry and pitch further can help increase the intensity of the ACEO depolarization; on the other hand, the prediction of nominal conditions for improved separation informs us about the region in which particles separate out. Thus, our method can be used to design electrostatic separation schemes

with improved efficiency as well as particle collection systems with discrete, well-defined collection zones for targeted capture. Further, this can also be extended to enable segregation and sorting based on material and geometric properties of the particles.

9.2 The sensing problem

In the process of researching a solution to the screening problem, the three key outcomes of our study have been: desalting, need for droplets and on-chip biasing. While examining the feasibility of electronic desalting on-chip, we have revisited the conventional model for EDL absorption and also confirmed through our experimental results that the actual desalting capacity is severely limited in highly saline buffers. This has prompted the need for incorporating geometric enhancements and scaling the reaction volume down to sub-nL droplets. Through a CMOS-compatible method of depositing Pt-black electrodes and their further electrochemical treatment, we have successfully recovered up to two orders of magnitude of electrically available area increment. Using this, we have realized the target V/SA requirement of 1 μm so that >40% of the salts can be depleted from a 10mM initial concentration. This provides a generic framework that can be integrated with any microfluidic system for sample preparation or control of ionic environments.

This 10mM concentration also serves as a crucial balance in terms of the effect of salt on the molecular stability for small molecules. We have examined the case of miRNA hybridization and conclude from our results that there is a 30-fold drop in target hybridization efficiency in low salt (0.01X PBS) as opposed to the optimum high salt buffer (1X PBS). However, the dehybridization experiment showed that we could swap from a high salt buffer to ∼10mM without loss of analytes. Desalting from this point is more feasible but, for this to work, it is crucial that the sensing measurements be performed rapidly to prevent loss of analytes. The on-chip electrodes and inherent symmetry of our desalting scheme facilitate a convenient method of simultaneously gating the transistor during that process itself. Using this feature, we have been able to operate individual devices with <3.5mV noise across 5 sweeps. Firstly, this obviates the need for turning off desalting fields during sensing, so ion back-diffusion does not interfere. Secondly, the device measurements can be completed much faster than the 15 min it takes for analytes to dehybridize in the low apparent salinity.

Further, we have extended the label-free detection method to large arrays of 1000's of transistors. This improves the statistical confidence of molecular sensing experiments that practical applications can benefit from, and also provides a framework for multiplexed detection. As the device to device variations in our experimental measurements have shown, a multi-pixel array is also a necessary condition for improving the

reliability of label-free biosensing. While implementing molecular functionalization protocols on FET arrays, we have encountered certain challenges. Spatial variations and surface topography could be causing either probe wettability issues with covalent chemistry; or the stacking of probe layers becuase of which target analytes are too far from the sensor surface. However, we have successfully shown repeatable detection of miRNA probes, within limits dictated by the kinetics of diffusion, with simultaneous control experiments in tandem.

9.3 Nanostructured and re-entrant superhydrophobic surface

A key requirement for a superhydrophbic surface to be truly dewetting in nature and mimic the lotus-leaf effect is for it to support very low contact angle hysteresis. We have designed an array of microstructures to achieve low sliding angles for liquid droplets. Our study is one of the few to combine the effects of both shape and roughness to maximize hydrophobicity. Using a re-entrant profile, we have fabricated surfaces that prevent falling of water droplets into gaps between microstructures from the Cassie wetting mode. Further, adding 3D nanopillars all over the surface has increased the roughness to minimize the apparent contact area so that a 171° contact angle with <1° sliding angle could be achieved. In the process of developing a process to etch sidewall nanopillars, we have addressed the issue of scalloping on DRIE micromachined structures that previously limited the applications of the MACEtch. This work has led to the development of a unique, highly scalable one-mask fabrication process of making three-dimensional multiscale structures and out-of-plane nanopillars that can open up several possibilities for applications that exploit the favourable scaling of surface characteristics.

9.4 Future work

The future developments of the label-free biosensor depend on leveraging the scalability of foundry fabricated transistors, firstly as a necessary condition for statistical reliability of measurements and, secondly, as an enabling factor for multiplexed screening. In order to meet this requirement, it is necessary to resolve existing issues that cause variations and the compatibility of known experimental protocols of analyte capture to overcome both wettability issues and the stacking problem. The next steps planned towards improving the capability and sensitivity of the label-free biosensor are as follows:

a) Improving probe monolayer control and optimization for maximum target capture.

Initially, we discussed the importance of different molecular conformations on device response. Both of

the functionalization protocols that we have sought to implement have worked optically for hybridization, but the electrical measurements have indicated otherwise. We have identified issues of probe stacking or non-wetting of the device trench that may have caused non-optimal molecular capture. We will perform high-resolution AFM measurements of the SAMs and molecular layers on the uneven surface of our chips to analyze the film quality and identify the physical issues or non-uniformities that may be affecting the exprimental results. Based on this data, we will undertake steps to improve both capture protocols (by eliminating heating steps that could cause multilayering or modifying the SAM surface hydrophilicity) to yield a uniform probe monolayer over which target molecules can efficiently hybridize. An alternative solution in the flat conformation could be to incorporate schemes of mixed monolayers [152] that relieve steric hindrances to improve hybridization efficiency. For the upright conformation, a more hydrophilic SAM surface such as 1,1-carbonyldiimidazole (CA<10°) [118] that can conjugate with amine-modified probes may be a good substitute for GPDMES.

b) Studies of diffusion limits and extending LOD for probe capture to <1μM.

Data from our probe detection experiments have correlated well with the diffusion-based absorption model for molecular monolayers. Our goal is to experimentally characterize settling times for smaller probe concentrations ($\leq 1\mu M$) so that it will enable us to achieve more uniform (albeit low) surface density that may be advantageous for hybridization. We will incorporate high humidity controls, to prevent evaporation and drying issues that are a risk against longer hold times, for capturing smaller concentrations of analytes. Further, the diffusion limitation will be calibrated in that process which, we believe, has not been experimentally characterized before.

c) Reducing the noise and variations across experiments.

One of the benefits of having multiple measurements within a single reaction is in the improved statistical confidence. We have been able to show mean electrical shifts with probe detection repeatably. This can help avoid mistakes from single measurements due to a dead pixel or an over-sensitive one. However, the spread in pixel response is large. Improvements in the quality and pixel uniformity of the electronic chips will certainly help. But, we also need to look at ways to filter out known bad/over-responsive pixels. Additionally, a method of functionalization and capture that provides a more homogeneous result will minimize errors due to surface variations during the experiment.

d) Sensitivity improvements with desalting.

The next step in improving the sensitivity of the arrays is to implement the on-chip desalting enhancements that we have developed over the course of this work. Towards that end, we have designed and also

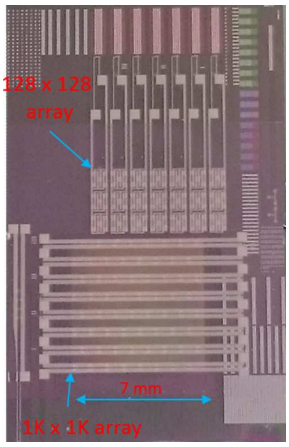

(a) Picture of a large array chip with on-chip Pt-electrodes on both 128x128 and 1024x1024 arrays

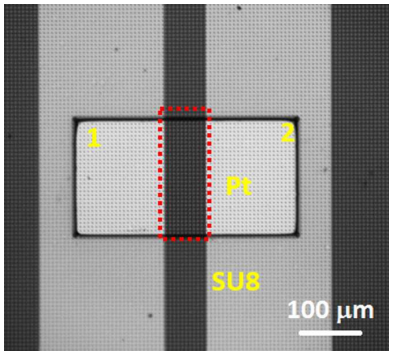

(b) A portion of the 1024x1024 arrays showing two Pt-electrodes in a SU8 well. The dotted line shows active devices

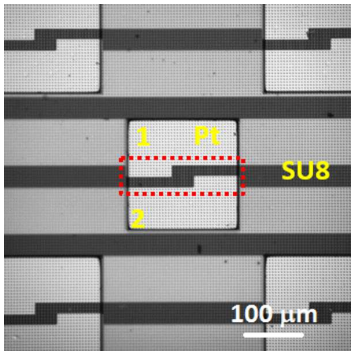

(c) A 128x128 array showing two Pt-electrodes in SU-8 wells. The dotted line shows active devices

Figure 9.1: Desalting electrodes on arrays of FETs.

microfabricated on-chip platinum electrodes. Figure 9.1 shows pictures of on-chip desalting electrodes that have been designed and are being characterized for improving the sensitivity of the FET arrays. In each array, a pair of desalting electrodes defined inside a SU8 well can be used to perform multiple parallel desalting/sensing experiments. Each well can contain ca. 150 (128x128 array/figure 9.1(c)) or 300 (1024x1024 array/figure 9.1(b)) active devices as indicated by the dotted lines. Based on initial attempts at gating devices with the on-chip electrodes, we have inferred that it may be necessary to incorporate microfabrication improvements to enhance the electrical isolation of the electrodes that are in contact over a densely packed array of transistors. Eventually, a modular approach that breaks down the system into smaller sub-arrays, each with their own desalting/QRE on-chip of high surface area could also help discretize the system.

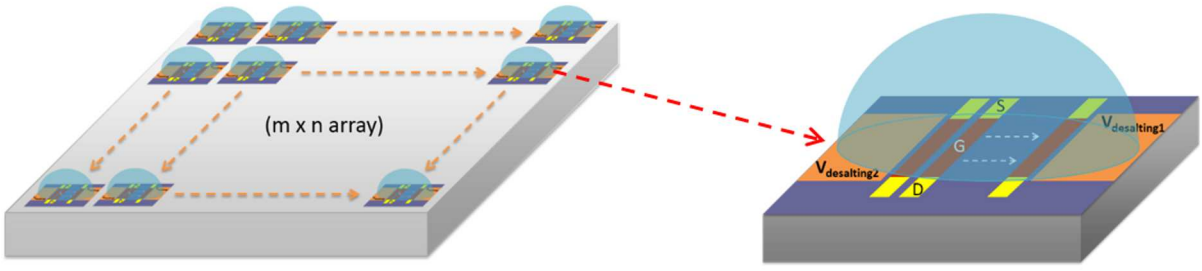

Figure 9.2: Schematic of a multiplexed label-free biosensing platform composed of arrays of field-effect sensors with localized desalting in droplets.

In the process of designing an on-chip desalting scheme for sensitivity improvement, we have reviewed both theoretical and experimental data and come to the understanding that volumetric limitation of the desalting capacity requires having to do so in a microdroplet. However, it also means that each reaction can be over a sub-array of FETs with independent desalting and device addressing in a droplet. The schematics in figure 9.2 illustrate this concept. The lengthscale also makes this approach more synergistic with digital microfluidics and droplet based assays [153, 154], which will contribute to the throughput for a multiplexed system in terms of parallel analyte processing and manipulation. Such a platform can be a very strong enabling factor towards realizing a label-free, point-of-care diagnostic technology.

References

[1] A. V. Delgado, F. Gonzlez-Caballero, R. J. Hunter, L. K. Koopal, and J. Lyklema, "Measurement and Interpretation of Electrokinetic Phenomena (IUPAC Technical Report)," *Pure and Applied Chemistry*, vol. 77, no. 10, pp. 1753–1805, 2005.

[2] P. Debye and E. Huckel, "Zur Theorie der Elektrolyte. I. Gefrierpunktserniedrigung und verwandte Erscheinungen," *Physikalische Zeitschrift*, vol. 24, no. 9, pp. 185–206, 1923.

[3] A. J. Bard and L. R. Faulkner, *Electrochemical methods: Fundamentals and Applications*. New York: Wiley, 2nd ed ed., 2001.

[4] V. V. Swaminathan, M. A. Shannon, and R. Bashir, "Enhanced sub-micron colloidal particle separation with interdigitated microelectrode arrays using mixed AC/DC dielectrophoretic scheme," *Biomedical Microdevices*, vol. 17, no. 2, p. 29, 2015.

[5] M. L. Wells and E. D. Goldberg, "Colloid aggregation in seawater," *Marine Chemistry*, vol. 41, no. 4, pp. 353–358, 1993.

[6] M. L. Wells and E. D. Goldberg, "The distribution of colloids in the North Atlantic and Southern Oceans," *Limnology and Oceanography*, vol. 39, no. 2, pp. 286–302, 1994.

[7] A. Yamasaki, H. Fukuda, R. Fukuda, T. Miyajima, T. Nagata, H. Ogawa, and I. Koike, "Submicrometer particles in northwest Pacific coastal environments: Abundance, size distribution, and biological origins," *Limnology and Oceanography*, vol. 43, no. 3, pp. 536–542, 1998.

[8] P. M. Dove and C. M. Craven, "Surface charge density on silica in alkali and alkaline earth chloride electrolyte solutions," *Geochimica et Cosmochimica Acta*, vol. 69, no. 21, pp. 4963–4970, 2005.

[9] P. Somasundaran, ed., *Encyclopedia of surface and colloid science*. New York: Taylor & Francis, 2nd ed ed., 2006.

[10] F. Wang and V. V. Tarabara, "Pore blocking mechanisms during early stages of membrane fouling by colloids," *Journal of Colloid and Interface Science*, vol. 328, no. 2, pp. 464–469, 2008.

[11] H. A. Pohl, *Dielectrophoresis: the behavior of neutral matter in nonuniform electric fields*. Cambridge monographs on physics, Cambridge ; New York: Cambridge University Press, 1978.

[12] R. Pethig, "Dielectrophoresis: Status of the theory, technology, and applications," *Biomicrofluidics*, vol. 4, no. 2, p. 022811, 2010.

[13] P. R. C. Gascoyne and J. Vykoukal, "Particle separation by dielectrophoresis," *ELECTROPHORESIS*, vol. 23, no. 13, p. 1973, 2002.

[14] D. Liu and S. V. Garimella, "Microfluidic Pumping Based on Traveling-Wave Dielectrophoresis," *Nanoscale and Microscale Thermophysical Engineering*, vol. 13, no. 2, pp. 109–133, 2009.

[15] K. Park, H.-J. Suk, D. Akin, and R. Bashir, "Dielectrophoresis-based cell manipulation using electrodes on a reusable printed circuit board," *Lab on a Chip*, vol. 9, no. 15, p. 2224, 2009.

[16] J. Cemazar, D. Vrtacnik, S. Amon, and T. Kotnik, "Dielectrophoretic Field-Flow Microchamber for Separation of Biological Cells Based on Their Electrical Properties," *IEEE Transactions on NanoBioscience*, vol. 10, no. 1, pp. 36–43, 2011.

[17] K. Zhu, A. S. Kaprelyants, E. G. Salina, and G. H. Markx, "Separation by dielectrophoresis of dormant and nondormant bacterial cells of Mycobacterium smegmatis," *Biomicrofluidics*, vol. 4, no. 2, p. 022809, 2010.

[18] P. Bajaj, D. Marchwiany, C. Duarte, and R. Bashir, "Patterned Three-Dimensional Encapsulation of Embryonic Stem Cells using Dielectrophoresis and Stereolithography," *Advanced Healthcare Materials*, vol. 2, no. 3, pp. 450–458, 2013.

[19] E. G. Cen, C. Dalton, Y. Li, S. Adamia, L. M. Pilarski, and K. V. Kaler, "A combined dielectrophoresis, traveling wave dielectrophoresis and electrorotation microchip for the manipulation and characterization of human malignant cells," *Journal of Microbiological Methods*, vol. 58, no. 3, pp. 387–401, 2004.

[20] C. Huang, H. Liu, N. H. Bander, and B. J. Kirby, "Enrichment of prostate cancer cells from blood cells with a hybrid dielectrophoresis and immunocapture microfluidic system," *Biomedical Microdevices*, vol. 15, no. 6, pp. 941–948, 2013.

[21] K. Park, D. Akin, and R. Bashir, "Electrical capture and lysis of vaccinia virus particles using silicon nano-scale probe array," *Biomedical Microdevices*, vol. 9, no. 6, pp. 877–883, 2007.

[22] M. Varshney and Y. Li, "Interdigitated array microelectrodes based impedance biosensors for detection of bacterial cells," *Biosensors and Bioelectronics*, vol. 24, no. 10, pp. 2951–2960, 2009.

[23] Z. Zou, S. Lee, and C. H. Ahn, "A Polymer Microfluidic Chip With Interdigitated Electrodes Arrays for Simultaneous Dielectrophoretic Manipulation and Impedimetric Detection of Microparticles," *IEEE Sensors Journal*, vol. 8, pp. 527–535, May 2008.

[24] D. R. Albrecht, R. L. Sah, and S. N. Bhatia, "Geometric and Material Determinants of Patterning Efficiency by Dielectrophoresis," *Biophysical Journal*, vol. 87, no. 4, pp. 2131–2147, 2004.

[25] J. Cao, P. Cheng, and F. Hong, "A numerical analysis of forces imposed on particles in conventional dielectrophoresis in microchannels with interdigitated electrodes," *Journal of Electrostatics*, vol. 66, no. 11-12, pp. 620–626, 2008.

[26] B. Edwards, A. Timperman, R. Carroll, K. Jo, J. Mease, and J. Schiffbauer, "Traveling-Wave Electrophoresis For Microfluidic Separations," *Physical Review Letters*, vol. 102, no. 7, p. 076103, 2009.

[27] K. D. Jo, J. E. Schiffbauer, B. E. Edwards, R. Lloyd Carroll, and A. T. Timperman, "Fabrication and performance of a microfluidic traveling-wave electrophoresis system," *The Analyst*, vol. 137, no. 4, p. 875, 2012.

[28] W. Li, H. Du, D. Chen, and C. Shu, "Analysis of dielectrophoretic electrode arrays for nanoparticle manipulation," *Computational Materials Science*, vol. 30, no. 3-4, pp. 320–325, 2004.

[29] T. Sun, H. Morgan, and N. Green, "Analytical solutions of ac electrokinetics in interdigitated electrode arrays: Electric field, dielectrophoretic and traveling-wave dielectrophoretic forces," *Physical Review E*, vol. 76, no. 4, 2007.

[30] J. Yantzi, J. Yeow, and S. Abdallah, "Multiphase electrodes for microbead control applications: Integration of DEP and electrokinetics for bio-particle positioning," *Biosensors and Bioelectronics*, vol. 22, no. 11, pp. 2539–2545, 2007.

[31] L. Wang, J. Lu, S. A. Marchenko, E. S. Monuki, L. A. Flanagan, and A. P. Lee, "Dual frequency dielectrophoresis with interdigitated sidewall electrodes for microfluidic flow-through separation of beads and cells," *Electrophoresis*, vol. 30, no. 5, pp. 782–791, 2009.

[32] N. Gadish and J. Voldman, "High-Throughput Positive-Dielectrophoretic Bioparticle Microconcentrator," *Analytical Chemistry*, vol. 78, no. 22, pp. 7870–7876, 2006.

[33] T. Horii, M. Yamamoto, T. Yasukawa, and F. Mizutani, "Rapid formation of cell-particle complexes via dielectrophoretic manipulation for the detection of surface antigens," *Biosensors and Bioelectronics*, vol. 61, pp. 215–221, 2014.

[34] K.-H. Han, S.-I. Han, and A. B. Frazier, "Lateral displacement as a function of particle size using a piecewise curved planar interdigitated electrode array," *Lab on a Chip*, vol. 9, no. 20, p. 2958, 2009.

[35] E. D. Pratt, C. Huang, B. G. Hawkins, J. P. Gleghorn, and B. J. Kirby, "Rare cell capture in microfluidic devices," *Chemical Engineering Science*, vol. 66, no. 7, pp. 1508–1522, 2011.

[36] A. Castellanos, A. Ramos, A. Gonzlez, N. G. Green, and H. Morgan, "Electrohydrodynamics and dielectrophoresis in microsystems: scaling laws," *Journal of Physics D: Applied Physics*, vol. 36, no. 20, pp. 2584–2597, 2003.

[37] A. Ramos, H. Morgan, N. G. Green, and A. Castellanos, "AC Electric-Field-Induced Fluid Flow in Microelectrodes," *Journal of Colloid and Interface Science*, vol. 217, no. 2, pp. 420–422, 1999.

[38] H. Zhou, L. R. White, and R. D. Tilton, "Lateral separation of colloids or cells by dielectrophoresis augmented by AC electroosmosis," *Journal of Colloid and Interface Science*, vol. 285, no. 1, pp. 179–191, 2005.

[39] J. J. Wu, "ac electro-osmotic micropump by asymmetric electrode polarization," *Journal of Applied Physics*, vol. 103, no. 2, p. 024907, 2008.

[40] A. J. Pascall and T. M. Squires, "Induced Charge Electro-osmosis over Controllably Contaminated Electrodes," *Physical Review Letters*, vol. 104, no. 8, p. 088301, 2010.

[41] P. Bergveld, "The development and application of FET-based biosensors," *Biosensors*, vol. 2, no. 1, pp. 15–33, 1986.

[42] P. Bergveld, "Thirty years of ISFETOLOGY," *Sensors and Actuators B: Chemical*, vol. 88, no. 1, pp. 1–20, 2003.

[43] S. Purushothaman, C. Toumazou, and C.-P. Ou, "Protons and single nucleotide polymorphism detection: A simple use for the Ion Sensitive Field Effect Transistor," *Sensors and Actuators B: Chemical*, vol. 114, no. 2, pp. 964–968, 2006.

[44] J. Go and M. A. Alam, "The future scalability of pH-based genome sequencers: A theoretical perspective," *Journal of Applied Physics*, vol. 114, no. 16, p. 164311, 2013.

[45] J. M. Rothberg, W. Hinz, T. M. Rearick, J. Schultz, W. Mileski, M. Davey, J. H. Leamon, K. Johnson, M. J. Milgrew, M. Edwards, J. Hoon, J. F. Simons, D. Marran, J. W. Myers, J. F. Davidson, A. Branting, J. R. Nobile, B. P. Puc, D. Light, T. A. Clark, M. Huber, J. T. Branciforte, I. B. Stoner, S. E. Cawley, M. Lyons, Y. Fu, N. Homer, M. Sedova, X. Miao, B. Reed, J. Sabina, E. Feierstein, M. Schorn, M. Alanjary, E. Dimalanta, D. Dressman, R. Kasinskas, T. Sokolsky, J. A. Fidanza, E. Namsaraev, K. J. McKernan, A. Williams, G. T. Roth, and J. Bustillo, "An integrated semiconductor device enabling non-optical genome sequencing," *Nature*, vol. 475, no. 7356, pp. 348–352, 2011.

[46] Y. Cui, Q. Wei, H. Park, and C. M. Lieber, "Nanowire Nanosensors for Highly Sensitive and Selective Detection of Biological and Chemical Species," *Science*, vol. 293, no. 5533, pp. 1289–1292, 2001.

[47] F. Patolsky, G. Zheng, and C. M. Lieber, "Nanowire sensors for medicine and the life sciences," *Nanomedicine*, vol. 1, no. 1, pp. 51–65, 2006.

[48] Y. L. Bunimovich, Y. S. Shin, W.-S. Yeo, M. Amori, G. Kwong, and J. R. Heath, "Quantitative Real-Time Measurements of DNA Hybridization with Alkylated Nonoxidized Silicon Nanowires in Electrolyte Solution," *Journal of the American Chemical Society*, vol. 128, no. 50, pp. 16323–16331, 2006.

[49] A. Gao, N. Lu, Y. Wang, P. Dai, T. Li, X. Gao, Y. Wang, and C. Fan, "Enhanced Sensing of Nucleic Acids with Silicon Nanowire Field Effect Transistor Biosensors," *Nano Letters*, vol. 12, no. 10, pp. 5262–5268, 2012.

[50] G.-J. Zhang, J. H. Chua, R.-E. Chee, A. Agarwal, and S. M. Wong, "Label-free direct detection of MiRNAs with silicon nanowire biosensors," *Biosensors and Bioelectronics*, vol. 24, no. 8, pp. 2504–2508, 2009.

[51] B. R. Dorvel, B. Reddy, J. Go, C. Duarte Guevara, E. Salm, M. A. Alam, and R. Bashir, "Silicon Nanowires with High-k Hafnium Oxide Dielectrics for Sensitive Detection of Small Nucleic Acid Oligomers," *ACS Nano*, vol. 6, no. 7, pp. 6150–6164, 2012.

[52] B. Dorvel, B. Reddy, and R. Bashir, "Effect of Biointerfacing Linker Chemistries on the Sensitivity of Silicon Nanowires for Protein Detection," *Analytical Chemistry*, vol. 85, no. 20, pp. 9493–9500, 2013.

[53] E. Stern, R. Wagner, F. J. Sigworth, R. Breaker, T. M. Fahmy, and M. A. Reed, "Importance of the Debye Screening Length on Nanowire Field Effect Transistor Sensors," *Nano Letters*, vol. 7, no. 11, pp. 3405–3409, 2007.

[54] G. Zheng, F. Patolsky, Y. Cui, W. U. Wang, and C. M. Lieber, "Multiplexed electrical detection of cancer markers with nanowire sensor arrays," *Nature Biotechnology*, vol. 23, no. 10, pp. 1294–1301, 2005.

[55] V. Krivitsky, L.-C. Hsiung, A. Lichtenstein, B. Brudnik, R. Kantaev, R. Elnathan, A. Pevzner, A. Khatchtourints, and F. Patolsky, "Si Nanowires Forest-Based On-Chip Biomolecular Filtering, Separation and Preconcentration Devices: Nanowires Do it All," *Nano Letters*, vol. 12, no. 9, pp. 4748–4756, 2012.

[56] F. Patolsky, G. Zheng, O. Hayden, M. Lakadamyali, X. Zhuang, and C. M. Lieber, "Electrical detection of single viruses," *Proceedings of the National Academy of Sciences*, vol. 101, no. 39, pp. 14017–14022, 2004.

[57] F. N. Ishikawa, H.-K. Chang, M. Curreli, H.-I. Liao, C. A. Olson, P.-C. Chen, R. Zhang, R. W. Roberts, R. Sun, R. J. Cote, M. E. Thompson, and C. Zhou, "Label-Free, Electrical Detection of the SARS Virus N-Protein with Nanowire Biosensors Utilizing Antibody Mimics as Capture Probes," *ACS Nano*, vol. 3, no. 5, pp. 1219–1224, 2009.

[58] B. Reddy, B. R. Dorvel, J. Go, P. R. Nair, O. H. Elibol, G. M. Credo, J. S. Daniels, E. K. C. Chow, X. Su, M. Varma, M. A. Alam, and R. Bashir, "High-k dielectric Al2o3 nanowire and nanoplate field effect sensors for improved pH sensing," *Biomedical Microdevices*, vol. 13, no. 2, pp. 335–344, 2011.

[59] J.-H. Ahn, S.-J. Choi, J.-W. Han, T. J. Park, S. Y. Lee, and Y.-K. Choi, "Double-Gate Nanowire Field Effect Transistor for a Biosensor," *Nano Letters*, vol. 10, no. 8, pp. 2934–2938, 2010.

[60] J.-H. Ahn, J.-Y. Kim, M.-L. Seol, D. J. Baek, Z. Guo, C.-H. Kim, S.-J. Choi, and Y.-K. Choi, "A pH sensor with a double-gate silicon nanowire field-effect transistor," *Applied Physics Letters*, vol. 102, no. 8, p. 083701, 2013.

[61] P. R. Nair and M. A. Alam, "Design Considerations of Silicon Nanowire Biosensors," *IEEE Transactions on Electron Devices*, vol. 54, no. 12, pp. 3400–3408, 2007.

[62] P. R. Nair and M. A. Alam, "Screening-Limited Response of NanoBiosensors," *Nano Letters*, vol. 8, no. 5, pp. 1281–1285, 2008.

[63] P. R. Nair and M. A. Alam, "Performance limits of nanobiosensors," *Applied Physics Letters*, vol. 88, no. 23, p. 233120, 2006.

[64] M. H. Sorensen, N. A. Mortensen, and M. Brandbyge, "Screening model for nanowire surface-charge sensors in liquid," *Applied Physics Letters*, vol. 91, no. 10, p. 102105, 2007.

[65] B. Dorvel, B. Reddy, I. Block, P. Mathias, S. E. Clare, B. Cunningham, D. E. Bergstrom, and R. Bashir, "Vapor-Phase Deposition of Monofunctional Alkoxysilanes for Sub-Nanometer-Level Biointerfacing on Silicon Oxide Surfaces," *Advanced Functional Materials*, vol. 20, no. 1, pp. 87–95, 2010.

[66] A. Kim, C. S. Ah, C. W. Park, J.-H. Yang, T. Kim, C.-G. Ahn, S. H. Park, and G. Y. Sung, "Direct label-free electrical immunodetection in human serum using a flow-through-apparatus approach with integrated field-effect transistors," *Biosensors and Bioelectronics*, vol. 25, no. 7, pp. 1767–1773, 2010.

[67] B. Honig and A. Nicholls, "Classical electrostatics in biology and chemistry," *Science*, vol. 268, no. 5214, pp. 1144–1149, 1995.

[68] N. K. Rajan, X. Duan, and M. A. Reed, "Performance limitations for nanowire/nanoribbon biosensors:," *Wiley Interdisciplinary Reviews: Nanomedicine and Nanobiotechnology*, vol. 5, no. 6, pp. 629–645, 2013.

[69] E. Stern, A. Vacic, N. K. Rajan, J. M. Criscione, J. Park, B. R. Ilic, D. J. Mooney, M. A. Reed, and T. M. Fahmy, "Label-free biomarker detection from whole blood," *Nature Nanotechnology*, vol. 5, no. 2, pp. 138–142, 2009.

[70] W. Guan, R. Fan, and M. A. Reed, "Field-effect reconfigurable nanofluidic ionic diodes," *Nature Communications*, vol. 2, p. 506, 2011.

[71] G.-J. Zhang, G. Zhang, J. H. Chua, R.-E. Chee, E. H. Wong, A. Agarwal, K. D. Buddharaju, N. Singh, Z. Gao, and N. Balasubramanian, "DNA Sensing by Silicon Nanowire: Charge Layer Distance Dependence," *Nano Letters*, vol. 8, no. 4, pp. 1066–1070, 2008.

[72] R. Elnathan, M. Kwiat, A. Pevzner, Y. Engel, L. Burstein, A. Khatchtourints, A. Lichtenstein, R. Kantaev, and F. Patolsky, "Biorecognition Layer Engineering: Overcoming Screening Limitations of Nanowire-Based FET Devices," *Nano Letters*, vol. 12, no. 10, pp. 5245–5254, 2012.

[73] A. Vacic, J. M. Criscione, N. K. Rajan, E. Stern, T. M. Fahmy, and M. A. Reed, "Determination of Molecular Configuration by Debye Length Modulation," *Journal of the American Chemical Society*, vol. 133, no. 35, pp. 13886–13889, 2011.

[74] G. S. Kulkarni and Z. Zhong, "Detection beyond the Debye Screening Length in a High-Frequency Nanoelectronic Biosensor," *Nano Letters*, vol. 12, no. 2, pp. 719–723, 2012.

[75] W. F. Dove and N. Davidson, "Cation effects on the denaturation of DNA," *Journal of Molecular Biology*, vol. 5, pp. 467–478, Nov. 1962.

[76] G. S. Manning, "The molecular theory of polyelectrolyte solutions with applications to the electrostatic properties of polynucleotides," *Quarterly Reviews of Biophysics*, vol. 11, no. 02, p. 179, 1978.

[77] C. Schildkraut and S. Lifson, "Dependence of the melting temperature of DNA on salt concentration," *Biopolymers*, vol. 3, no. 2, pp. 195–208, 1965.

[78] R. Owczarzy, Y. You, B. G. Moreira, J. A. Manthey, L. Huang, M. A. Behlke, and J. A. Walder, "Effects of Sodium Ions on DNA Duplex Oligomers: Improved Predictions of Melting Temperatures," *Biochemistry*, vol. 43, no. 12, pp. 3537–3554, 2004.

[79] A. Panjkovich and F. Melo, "Comparison of different melting temperature calculation methods for short DNA sequences," *Bioinformatics*, vol. 21, no. 6, pp. 711–722, 2005.

[80] G. Khandelwal and J. Bhyravabhotla, "A Phenomenological Model for Predicting Melting Temperatures of DNA Sequences," *PLoS ONE*, vol. 5, p. e12433, Aug. 2010.

[81] B. E. Conway, *Electrochemical supercapacitors: Scientific Fundamentals and Technological Applications*. New York: Plenum Press, 1999.

[82] A. M. Johnson and J. Newman, "Desalting by Means of Porous Carbon Electrodes," *Journal of The Electrochemical Society*, vol. 118, no. 3, pp. 510–517, 1971.

[83] T. Welgemoed and C. Schutte, "Capacitive Deionization Technology: An alternative desalination solution," *Desalination*, vol. 183, no. 1-3, pp. 327–340, 2005.

[84] M. Andelman, "Flow Through Capacitor basics," *Separation and Purification Technology*, vol. 80, no. 2, pp. 262–269, 2011.

[85] O. N. Demirer and C. H. Hidrovo, "Laser-induced fluorescence visualization of ion transport in a pseudo-porous capacitive deionization microstructure," *Microfluidics and Nanofluidics*, vol. 16, no. 1-2, pp. 109–122, 2014.

[86] K. Mani, "Electrodialysis water splitting technology," *Journal of Membrane Science*, vol. 58, no. 2, pp. 117–138, 1991.

[87] Z. J. Han, R. Morrow, B. K. Tay, and D. McKenzie, "Time-dependent electrical double layer with blocking electrode," *Applied Physics Letters*, vol. 94, no. 4, p. 043118, 2009.

[88] V. V. Swaminathan, P. Dak, B. Reddy, E. Salm, C. Duarte-Guevara, Y. Zhong, A. Fischer, Y.-S. Liu, M. A. Alam, and R. Bashir, "Electronic desalting for controlling the ionic environment in droplet-based biosensing platforms," *Applied Physics Letters*, vol. 106, no. 5, p. 053105, 2015.

[89] J.-H. Lee, W.-S. Bae, and J.-H. Choi, "Electrode reactions and adsorption/desorption performance related to the applied potential in a capacitive deionization process," *Desalination*, vol. 258, no. 1-3, pp. 159–163, 2010.

[90] M. Gouy, "Sur la constitution de la charge electrique a la surface d'un electrolyte," *J. Phys. Theor. Appl.*, vol. 9, no. 1, pp. 457–468, 1910.

[91] D. L. Chapman, "A contribution to the theory of electrocapillarity," *Philosophical Magazine Series 6*, vol. 25, no. 148, pp. 475–481, 1913.

[92] M. Kilic, M. Bazant, and A. Ajdari, "Steric effects in the dynamics of electrolytes at large applied voltages. I. Double-layer charging," *Physical Review E*, vol. 75, no. 2, p. 021502, 2007.

[93] Iglic, A. and Kralj-Iglic, V., "Influence of finite size of ions on electrostatic properties of electric double layer," *Electrotechnical Review (Slovenia)*, vol. 61, no. 3, pp. 127–133, 1994.

[94] I. Borukhov, D. Andelman, and H. Orland, "Steric Effects in Electrolytes: A Modified Poisson-Boltzmann Equation," *Physical Review Letters*, vol. 79, no. 3, pp. 435–438, 1997.

[95] Thermo Scientific, "NHS and Sulfo-NHS protocol," 2011.

[96] J. Drelich, E. Chibowski, D. D. Meng, and K. Terpilowski, "Hydrophilic and superhydrophilic surfaces and materials," *Soft Matter*, vol. 7, no. 21, p. 9804, 2011.

[97] C. Duarte-Guevara, V. V. Swaminathan, M. Burgess, B. Reddy, E. Salm, Y.-S. Liu, J. Rodriguez-Lopez, and R. Bashir, "On-chip metal/polypyrrole quasi-reference electrodes for robust ISFET operation," *The Analyst*, vol. 140, pp. 3630–3641, 2015.

[98] E. Salm, Y. Zhong, B. Reddy, C. Duarte-Guevara, V. Swaminathan, Y.-S. Liu, and R. Bashir, "Electrical Detection of Nucleic Acid Amplification Using an On-Chip Quasi-Reference Electrode and a PVC REFET," *Analytical Chemistry*, vol. 86, no. 14, pp. 6968–6975, 2014.

[99] P. W. Atkins, *Physical Chemistry*. New York: Freeman, 6th ed ed., 1998.

[100] R. Behrends, K. Fuchs, U. Kaatze, Y. Hayashi, and Y. Feldman, "Dielectric properties of glycerol/water mixtures at temperatures between 10 and 50 C," *The Journal of Chemical Physics*, vol. 124, no. 14, p. 144512, 2006.

[101] M. W. Shinwari, D. Zhitomirsky, I. A. Deen, P. R. Selvaganapathy, M. J. Deen, and D. Landheer, "Microfabricated Reference Electrodes and their Biosensing Applications," *Sensors*, vol. 10, no. 3, pp. 1679–1715, 2010.

[102] A. van den Berg, A. Grisel, H. van den Vlekkert, and N. de Rooij, "A micro-volume open liquid-junction reference electrode for pH-ISFETs," *Sensors and Actuators B: Chemical*, vol. 1, no. 1-6, pp. 425–432, 1990.

[103] S. Chen and S.-L. Zhang, "Contacting versus Insulated Gate Electrode for Si Nanoribbon Field-Effect Sensors Operating in Electrolyte," *Analytical Chemistry*, vol. 83, no. 24, pp. 9546–9551, 2011.

[104] P. Simon and Y. Gogotsi, "Materials for electrochemical capacitors," *Nature Materials*, vol. 7, no. 11, pp. 845–854, 2008.

[105] A. Ebrahimi, P. Dak, E. Salm, S. Dash, S. V. Garimella, R. Bashir, and M. A. Alam, "Nanotextured superhydrophobic electrodes enable detection of attomolar-scale DNA concentration within a droplet by non-faradaic impedance spectroscopy," *Lab on a Chip*, vol. 13, no. 21, p. 4248, 2013.

[106] M. Nishizawa, V. P. Menon, and C. R. Martin, "Metal Nanotubule Membranes with Electrochemically Switchable Ion-Transport Selectivity," *Science*, vol. 268, no. 5211, pp. 700–702, 1995.

[107] R. Jayashree, J. Spendelow, J. Yeom, C. Rastogi, M. Shannon, and P. Kenis, "Characterization and application of electrodeposited Pt, Pt/Pd, and Pd catalyst structures for direct formic acid micro fuel cells," *Electrochimica Acta*, vol. 50, no. 24, pp. 4674–4682, 2005.

[108] G. Zhang, S. Sun, M. Cai, Y. Zhang, R. Li, and X. Sun, "Porous Dendritic Platinum Nanotubes with Extremely High Activity and Stability for Oxygen Reduction Reaction," *Scientific Reports*, vol. 3, 2013.

[109] Z. Huang, N. Geyer, P. Werner, J. de Boor, and U. Gsele, "Metal-Assisted Chemical Etching of Silicon: A Review," *Advanced Materials*, vol. 23, no. 2, pp. 285–308, 2011.

[110] W. Ye, C. Shen, J. Tian, C. Wang, L. Bao, and H. Gao, "Self-assembled synthesis of SERS-active silver dendrites and photoluminescence properties of a thin porous silicon layer," *Electrochemistry Communications*, vol. 10, no. 4, pp. 625–629, 2008.

[111] L. Zhu, N. Kroodsma, J. Yeom, J. L. Haan, M. A. Shannon, and D. D. Meng, "An on-demand microfluidic hydrogen generator with self-regulated gas generation and self-circulated reactant exchange with a rechargeable reservoir," *Microfluidics and Nanofluidics*, vol. 11, no. 5, pp. 569–578, 2011.

[112] E. Barsoukov and J. R. Macdonald, eds., *Impedance spectroscopy: Theory, Experiment, and Applications*. Hoboken, N.J: Wiley-Interscience, 2nd ed ed., 2005.

[113] J. Kang, J. Wen, S. H. Jayaram, A. Yu, and X. Wang, "Development of an equivalent circuit model for electrochemical double layer capacitors (EDLCs) with distinct electrolytes," *Electrochimica Acta*, vol. 115, pp. 587–598, 2014.

[114] F. Heer, W. Franks, A. Blau, S. Taschini, C. Ziegler, A. Hierlemann, and H. Baltes, "CMOS microelectrode array for the monitoring of electrogenic cells," *Biosensors and Bioelectronics*, vol. 20, no. 2, pp. 358–366, 2004.

[115] H. Wang and L. Pilon, "Accurate Simulations of Electric Double Layer Capacitance of Ultramicroelectrodes," *The Journal of Physical Chemistry C*, vol. 115, no. 33, pp. 16711–16719, 2011.

[116] L. Qiang, S. Vaddiraju, J. F. Rusling, and F. Papadimitrakopoulos, "Highly sensitive and reusable Pt-black microfluidic electrodes for long-term electrochemical sensing," *Biosensors and Bioelectronics*, vol. 26, no. 2, pp. 682–688, 2010.

[117] C. Duarte-Guevara, F.-L. Lai, C.-W. Cheng, B. Reddy, E. Salm, V. Swaminathan, Y.-K. Tsui, H. C. Tuan, A. Kalnitsky, Y.-S. Liu, and R. Bashir, "Enhanced Biosensing Resolution with Foundry Fabricated Individually Addressable Dual-Gated ISFETs," *Analytical Chemistry*, vol. 86, no. 16, pp. 8359–8367, 2014.

[118] J. M. Goddard and D. Erickson, "Bioconjugation techniques for microfluidic biosensors," *Analytical and Bioanalytical Chemistry*, vol. 394, no. 2, pp. 469–479, 2009.

[119] V. V. Swaminathan, S. Gannavaram, S. Li, H. Hu, J. Yeom, Y. Wang, and L. Zhu, "Microfluidic platform with hierarchical micro/nanostructures and SELEX nucleic acid aptamer coating for isolation of circulating tumor cells," in *13th IEEE International Conference on Nanotechnology*, (Beijing, China), pp. 370–373, IEEE, Aug. 2013.

[120] H. Hu, V. V. Swaminathan, M. R. Z. Farahani, G. Mensing, J. Yeom, M. A. Shannon, and L. Zhu, "Hierarchically structured re-entrant microstructures for superhydrophobic surfaces with extremely low hysteresis," *Journal of Micromechanics and Microengineering*, vol. 24, p. 095023, Sept. 2014.

[121] T. Darmanin, E. T. de Givenchy, S. Amigoni, and F. Guittard, "Superhydrophobic Surfaces by Electrochemical Processes," *Advanced Materials*, vol. 25, no. 10, pp. 1378–1394, 2013.

[122] S. Wang and L. Jiang, "Definition of Superhydrophobic States," *Advanced Materials*, vol. 19, no. 21, pp. 3423–3424, 2007.

[123] R. Blossey, "Self-cleaning surfaces virtual realities," *Nature Materials*, vol. 2, no. 5, pp. 301–306, 2003.

[124] R. Frstner, W. Barthlott, C. Neinhuis, and P. Walzel, "Wetting and Self-Cleaning Properties of Artificial Superhydrophobic Surfaces," *Langmuir*, vol. 21, no. 3, pp. 956–961, 2005.

[125] H. Zeng and Y. Zhao, "Liquid-state motion sensing," *Sensors and Actuators B: Chemical*, vol. 154, no. 1, pp. 33–40, 2011.

[126] A. J. Scardino, H. Zhang, D. J. Cookson, R. N. Lamb, and R. d. Nys, "The role of nano-roughness in antifouling," *Biofouling*, vol. 25, no. 8, pp. 757–767, 2009.

[127] L. Mishchenko, B. Hatton, V. Bahadur, J. A. Taylor, T. Krupenkin, and J. Aizenberg, "Design of Ice-free Nanostructured Surfaces Based on Repulsion of Impacting Water Droplets," *ACS Nano*, vol. 4, no. 12, pp. 7699–7707, 2010.

[128] N. Miljkovic, R. Enright, Y. Nam, K. Lopez, N. Dou, J. Sack, and E. N. Wang, "Jumping-Droplet-Enhanced Condensation on Scalable Superhydrophobic Nanostructured Surfaces," *Nano Letters*, vol. 13, no. 1, pp. 179–187, 2013.

[129] Y. Kwon, N. Patankar, J. Choi, and J. Lee, "Design of Surface Hierarchy for Extreme Hydrophobicity," *Langmuir*, vol. 25, no. 11, pp. 6129–6136, 2009.

[130] A. B. D. Cassie and S. Baxter, "Wettability of porous surfaces," *Transactions of the Faraday Society*, vol. 40, p. 546, 1944.

[131] A. Milne and A. Amirfazli, "The Cassie equation: How it is meant to be used," *Advances in Colloid and Interface Science*, vol. 170, no. 1-2, pp. 48–55, 2012.

[132] J. Han, J. Yeom, G. Mensing, D. Joe, R. I. Masel, and M. A. Shannon, "Surface energy approach and AFM verification of the (CF)n treated surface effect and its correlation with adhesion reduction in microvalves," *Journal of Micromechanics and Microengineering*, vol. 19, no. 8, p. 085017, 2009.

[133] J. Feng, M. T. Tuominen, and J. P. Rothstein, "Hierarchical Superhydrophobic Surfaces Fabricated by Dual-Scale Electron-Beam-Lithography with Well-Ordered Secondary Nanostructures," *Advanced Functional Materials*, vol. 21, no. 19, pp. 3715–3722, 2011.

[134] H. E. Jeong, M. K. Kwak, C. I. Park, and K. Y. Suh, "Wettability of nanoengineered dual-roughness surfaces fabricated by UV-assisted capillary force lithography," *Journal of Colloid and Interface Science*, vol. 339, no. 1, pp. 202–207, 2009.

[135] L. Feng, Y. Zhang, J. Xi, Y. Zhu, N. Wang, F. Xia, and L. Jiang, "Petal Effect: A Superhydrophobic State with High Adhesive Force," *Langmuir*, vol. 24, no. 8, pp. 4114–4119, 2008.

[136] D.-H. Kim, Y. Kim, B. M. Kim, J. S. Ko, C.-R. Cho, and J.-M. Kim, "Uniform superhydrophobic surfaces using micro/nano complex structures formed spontaneously by a simple and cost-effective nonlithographic process based on anodic aluminum oxide technology," *Journal of Micromechanics and Microengineering*, vol. 21, no. 4, p. 045003, 2011.

[137] Y. Li, X. J. Huang, S. H. Heo, C. C. Li, Y. K. Choi, W. P. Cai, and S. O. Cho, "Superhydrophobic Bionic Surfaces with Hierarchical Microsphere/SWCNT Composite Arrays," *Langmuir*, vol. 23, no. 4, pp. 2169–2174, 2007.

[138] Z. Ma, C. Jiang, X. Li, F. Ye, and W. Yuan, "Controllable fabrication of periodic arrays of high-aspect-ratio micro-nano hierarchical structures and their superhydrophobicity," *Journal of Micromechanics and Microengineering*, vol. 23, no. 9, p. 095027, 2013.

[139] Y. Xiu, L. Zhu, D. W. Hess, and C. P. Wong, "Hierarchical Silicon Etched Structures for Controlled Hydrophobicity/Superhydrophobicity," *Nano Letters*, vol. 7, no. 11, pp. 3388–3393, 2007.

[140] L. Cao, T. P. Price, M. Weiss, and D. Gao, "Super Water- and Oil-Repellent Surfaces on Intrinsically Hydrophilic and Oleophilic Porous Silicon Films," *Langmuir*, vol. 24, no. 5, pp. 1640–1643, 2008.

[141] C. Lee and C.-J. C. Kim, "Maximizing the Giant Liquid Slip on Superhydrophobic Microstructures by Nanostructuring Their Sidewalls," *Langmuir*, vol. 25, no. 21, pp. 12812–12818, 2009.

[142] A. Tuteja, W. Choi, M. Ma, J. M. Mabry, S. A. Mazzella, G. C. Rutledge, G. H. McKinley, and R. E. Cohen, "Designing Superoleophobic Surfaces," *Science*, vol. 318, no. 5856, pp. 1618–1622, 2007.

[143] T. E. F. M. Standaert, C. Hedlund, E. A. Joseph, G. S. Oehrlein, and T. J. Dalton, "Role of fluorocarbon film formation in the etching of silicon, silicon dioxide, silicon nitride, and amorphous hydrogenated silicon carbide," *Journal of Vacuum Science & Technology A: Vacuum, Surfaces, and Films*, vol. 22, no. 1, p. 53, 2004.

[144] K. Peng, Y. Yan, S. Gao, and J. Zhu, "Dendrite-Assisted Growth of Silicon Nanowires in Electroless Metal Deposition," *Advanced Functional Materials*, vol. 13, no. 2, pp. 127–132, 2003.

[145] B. S. Kim, S. Shin, S. J. Shin, K. M. Kim, and H. H. Cho, "Control of Superhydrophilicity/Superhydrophobicity using Silicon Nanowires via Electroless Etching Method and Fluorine Carbon Coatings," *Langmuir*, vol. 27, no. 16, pp. 10148–10156, 2011.

[146] M. K. Dawood, H. Zheng, T. H. Liew, K. C. Leong, Y. L. Foo, R. Rajagopalan, S. A. Khan, and W. K. Choi, "Mimicking Both Petal and Lotus Effects on a Single Silicon Substrate by Tuning the Wettability of Nanostructured Surfaces," *Langmuir*, vol. 27, no. 7, pp. 4126–4133, 2011.

[147] C.-Y. Chen, C.-S. Wu, C.-J. Chou, and T.-J. Yen, "Morphological Control of Single-Crystalline Silicon Nanowire Arrays near Room Temperature," *Advanced Materials*, vol. 20, no. 20, pp. 3811–3815, 2008.

[148] M.-H. Chen, T.-H. Hsu, Y.-J. Chuang, and F.-G. Tseng, "Dual hierarchical biomimic superhydrophobic surface with three energy states," *Applied Physics Letters*, vol. 95, no. 2, p. 023702, 2009.

[149] M. Im, H. Im, J.-H. Lee, J.-B. Yoon, and Y.-K. Choi, "A robust superhydrophobic and superoleophobic surface with inverse-trapezoidal microstructures on a large transparent flexible substrate," *Soft Matter*, vol. 6, no. 7, p. 1401, 2010.

[150] Y. He, C. Jiang, H. Yin, J. Chen, and W. Yuan, "Superhydrophobic silicon surfaces with micronano hierarchical structures via deep reactive ion etching and galvanic etching," *Journal of Colloid and Interface Science*, vol. 364, no. 1, pp. 219–229, 2011.

[151] J. B. Boreyko, C. H. Baker, C. R. Poley, and C.-H. Chen, "Wetting and Dewetting Transitions on Hierarchical Superhydrophobic Surfaces," *Langmuir*, vol. 27, no. 12, pp. 7502–7509, 2011.

[152] R. A. Shircliff, I. T. Martin, J. W. Pankow, J. Fennell, P. Stradins, M. L. Ghirardi, S. W. Cowley, and H. M. Branz, "High-Resolution X-ray Photoelectron Spectroscopy of Mixed Silane Monolayers for DNA Attachment," *ACS Applied Materials & Interfaces*, vol. 3, no. 9, pp. 3285–3292, 2011.

[153] V. Srinivasan, V. K. Pamula, and R. B. Fair, "An integrated digital microfluidic lab-on-a-chip for clinical diagnostics on human physiological fluids," *Lab on a Chip*, vol. 4, no. 4, p. 310, 2004.

[154] R. B. Fair, "Digital microfluidics: is a true lab-on-a-chip possible?," *Microfluidics and Nanofluidics*, vol. 3, no. 3, pp. 245–281, 2007.

[155] M. Castellarnau, N. Zine, J. Bausells, C. Madrid, A. Jurez, J. Samitier, and A. Errachid, "Integrated cell positioning and cell-based ISFET biosensors," *Sensors and Actuators B: Chemical*, vol. 120, no. 2, pp. 615–620, 2007.

[156] H. Li, Y. Zheng, D. Akin, and R. Bashir, "Characterization and modeling of a microfluidic dielectrophoresis filter for biological species," *Journal of Microelectromechanical Systems*, vol. 14, no. 1, pp. 103–112, 2005.

[157] A. Neculae, O. M. Bunoiu, M. Lungu, M. Bunoiu, and I. Malaescu, "Numerical Simulation of Bioparticle Manipulation Using Dielectrophoresis," in *Proceedings of the Physics conference, AIP*, vol. 1262, (Timisoara, Romania), pp. 144–149, AIP, 2010.

[158] C. A. R. Perez, O. N. Demirer, R. L. Clifton, R. M. Naylor, and C. H. Hidrovo, "Macro Analysis of the Electro-Adsorption Process in Low Concentration NaCl Solutions for Water Desalination Applications," *Journal of The Electrochemical Society*, vol. 160, pp. E13–E21, Jan. 2013.

[159] S. Rigante, P. Livi, A. Rusu, Y. Chen, A. Bazigos, A. Hierlemann, and A. M. Ionescu, "FinFET integrated low-power circuits for enhanced sensing applications," *Sensors and Actuators B: Chemical*, vol. 186, pp. 789–795, 2013.

[160] V. V. Swaminathan, H. Hu, M. R. Z. Farhani, G. Mensing, J. Yeom, M. A. Shannon, and L. Zhu, "Hierarchical and re-entrant micro/nanostructures for superhydrophobic surfaces with extremely low hysteresis," in *246th ACS National Meeting & Exposition*, (Indianapolis), Sept. 2013.

[161] V. V. Swaminathan, P. Dak, B. Reddy (Jr.), E. Salm, C. Duarte-Guevara, Y. Zhong, A. Fischer, J. Huang, J. Yang, Y.-S. Liu, M. A. Alam, and R. Bashir, "Localized Electronic Desalting Around Field-Effect Sensors for Molecular Detection in Droplets with Enhanced Sensitivity," in *36th Annual International Conference of the IEEE Engineering in Medicine and Biology Society*, (Chicago, USA), Aug. 2014.